Table of Contents

Abstract iii

Acknowledgements vii

Table of Contents ix

List of Figures xiii

List of Tables xvii

Nomenclature xix

CHAPTER 1: Introduction 1

1.1 Nanostructures 1

1.2 Nanostructures in Thermoelectric Applications 3

1.3 Heat Transfer in Nanostructures 6

1.4 Motivation 8

1.5 Outline of The Thesis 8

1.6 List of Articles Prepared 11

1.6.1 Journal articles 11

1.6.2 Conference articles 11

CHAPTER 2: Theoretical Background 13

2.1 Outline 13

2.2 Molecular Dynamics in Nanoscale Heat Transfer 14

2.3 Direct Method for Evaluating Thermal Conductivity 17

2.4 Green-Kubo Method for Evaluating Thermal Conductivity 18

2.5 Lattice Dynamics 20

2.6 Boltzmann Transport Equation 22

2.7 Normal Mode Decomposition 25

2.8 Allen-Feldman Theory 27

CHAPTER 3: Modal Analysis of the Thermal Conductivity of Nanowires 29

3.1 Introduction 29

3.2 Theoretical and Computational Formalism 32

3.2.1 Lattice dynamic calculations 32

3.2.2 Normal mode decomposition 35

3.3 Results and Discussion 38

3.3.1 Case Studies: pristine and superlattice nanowires 38

3.3.2 Non-monotonic diameter dependence of TC of nanowires 44

3.3.3 TC evaluation of shell alloyed nanowires (SANWs) 48

CHAPTER 4: Thermal Performance of Si/Ge Random Layer Nanowires 57

4.1 Introduction 57

4.2 Simulation Procedures 60

4.2.1 Constructing random layer structures 60

4.2.2 Implementation of non-equilibrium molecular dynamics 62

4.2.3 Implementation of GAMMA-normal mode decomposition 63

4.3 Results and Discussion 65

4.3.1 Mode level analysis of SL and RL structures 65

4.3.2 Effect of cross-sectional width 69

4.3.3 Effect of mean layer thickness 74

4.3.4 Effect of temperature and total length 76

4.3.5 Effect of shell modifications 78

CHAPTER 5: Thermal Performance of Nanotwinned Random Layer Structures 81

5.1 Introduction 81

5.2 Computational Procedure 83

5.3 Results and Discussion 85

5.3.1 Evaluation the TC of NTRL structures 85

5.3.2 Effect of temperature for TC of NTRL structures 87

5.3.3 Ultra-low TC of mix hetero-nanotwinned random layer structures 89

CHAPTER 6: Conclusions, Limitations and Future Work 91

6.1 Conclusions 91

6.2 Limitations 94

6.3 Future Work 95

Appendix A: Convergence Issue of 1D Structures 97

Appendix B: Identification of Acoustic Branches 99

Appendix C: Evaluation of Eigenvector Periodicity Index (I_n) 101

Appendix D: Details of Random Layer Distributions 105

Appendix E: Comparison of TC of Two Types of NTRL Structures 107

Appendix F: Statistics of Computational Simulations 109

References 111

List of Figures

Figure 1-1: Different types of nanostructures (*a*) multi-layers [23] (*b*) *ZnO* nanowires [24] (*c*) Carbon nanotubes [25] (*d*) *Si* nanomesh [10] (*e*) *InGaAsP/InAlAs* superlattice [12]................3

Figure 3-1: Atomic configurations of (a) nanowire of cross-sectional width 2.1 nm and (b) unit-cell (UC) defined for the nanowire...34

Figure 3-2: (a) Dispersion curve of the nanowire in Figure 3-1. (b) *PR* of modes of nanowire of total length 32 UCs. 35

Figure 3-3: Cumulative K_OP of (a) PNW and (b) SLNW...39

Figure 3-4: Phonon relaxation times of the (a) PNW and (b) SLNW. 40

Figure 3-5: Cumulative TC of PNW's (a) AF, (b) AL, (c) AT and SLNW's (d) AF, (e) AL, (f) AT branches over ω at different structure size. 42

Figure 3-6: Comparison of TC evaluated by NMD and GK methods of (a) PNW and (b) SLNW. 43

Figure 3-7:TC variation with the NW cross-sectional width...45

Figure 3-8: (a) DOS over ω. (b)Normalized cumulative TC of structures over ω.................46

Figure 3-9: Modal (a) group velocity and (b) relaxation time of NWs of three different cross-sectional widths..48

Figure 3-10: Atomic configuration of SANW. The green box encloses the core region of the SANW. 49

Figure 3-11: I_n of (a) PNW, (b) SANW of m_B=2m_A, (c) SANW of m_B=3m_A and (d) SANW of m_B=5m_A. *PR* of (e) PNW, (f) SANW of m_B=2m_A, (g) SANW of m_B=3m_A and (h) SANW of m_B=5m_A. 51

Figure 3-12:Corresponding virtual crystal atomic configuration for the one shown in Figure 3-10. 54

Figure 3-13: Comparison of the DOS of SANW and corresponding virtual crystal structure. 54

Figure 3-14: Comparison of relaxation times evaluated by VC-NMD and GNMD................55

Figure 3-15: Diffusivities evaluate by both VC-NMD and AF for SANWs of alloy atomic mass of (a)2m_A, (b)3m_A and (c)5m_A. 55

Figure 3-16: (a) TC evaluation different modes of SANWs. (b) Comparison of normalized cumulative TC of SANWs of different alloy mass species and the PNW counterpart............56

Figure 4-1:(top) Atomic configuration of SLNW of mean layer thickness 1.08 nm and cross-sectional width 1.54 nm. (Bottom) Atomic Configuration of RLNW of same mean layer thickness and cross-sectional width. 61

Figure 4-2: Temperature profile of a RLNW of 52.1 nm long. 63

Figure 4-3: Comparison of PR of (a) SL and RL structures and (b) RL structures of different total lengths. 66

Figure 4-4: SED of selected few modes of (a) SL (b) RL structures, (c) phonon relaxation time values. 68

Figure 4-5: Illustration of TC of RLNWs and corresponding SLNW of different cross-sectional widths. The total length of all the nanowires in the figure is 52.1nm. Here NW reduction % is corresponding to the reduction % of RLNWs over SLNWs while bulk reduction % is for bulk counterparts. 70

Figure 4-6: DOS against Frequency for nanowires of three different cross-sectional widths and corresponding bulk counterpart. The mean layer thickness of all the nanowires is kept as 1.08 nm 71

Figure 4-7: *PR* of SLNW and RLNW of mean layer thickness 1.08 nm, cross-sectional width 1.54 nm and total length 52.1 nm. 72

Figure 4-8 :Comparison of TC between RLNWs and corresponding SLNWs of different mean layer thicknesses. 75

Figure 4-9: (a)TC variation of SLNWs and RLNWs with temperature. The total length and cross-sectional width of NWs are kept at 100 nm and 1.54 nm, respectively. (b) TC variation with respect to nanowire total length. The mean layer thickness and cross-sectional width are kept at 1.08 nm and 1.54 nm, respectively. 77

Figure 4-10: TC of nanowires with (a) random shell atom mixing and (b) random shell atom removal. Total length, cross-sectional width and mean layer thickness are kept as 100 nm, 1.54 nm and 1.08 nm, respectively. 79

Figure 5-1:Atomic configurations of NTSL (top) and NTRL structures (bottom). Twin boundaries are highlighted in boxes. 83

Figure 5-2 : Illustration of TC of NTSL and NTRL structures of length (a) 90 nm (b) 170 nm. 86

Figure 5-3:PR of NTSL and NTSL of total length 22.5 nm. 87

Figure 5-4 : Effect of temperature on TC of NTSL and NTRL structures. 88

Figure 5-5 :Atomic configuration of a mix-HNTRL structure in which mean layer thicknesses from both twin and material random distributions are kept at 1.88 nm. Twin boundaries are highlighted in boxes. 89

Figure 5-6 : TC of c-HRL, HNTRL and mix-HNTRL structures of total length 90 nm for different random twin boundary and Si/Ge random distributions. 90

Figure B-1 :Vector plot of eigenvectors of (a)AT (b)AL and (c)AF branches. 99

Figure C-1: Variation of Eigenvector components of PNW of mode ω= 0.3448 rad.THz along (a) X, (b) Y and (c) Z axis, and (d)-(f) corresponding autocorrelation (Π), respectively. The * at (d)-(f) denote the corresponding points of lag equals 0 and $Lg/2$. 102

Bestofe.com

Figure C-2: Π of PNW for modes of ω equals to (a) 0.3448, (b) 8.2554 and (c) 16.6858 rad.THz. Π of SANW of m_B=2m_A for modes of ω equals to (a) 0.2903, (b) 7.0679 and (c) 16.4460 rad.THz. 103

Figure E-1: Comparison of the TC of NTRL of two different random twin boundary distributions........ 107

Figure F-1: (a)NMD simulations in chapter 3 and (b) NEMD simulations in chapter 4 and 5. 109

List of Tables

Table 3-1: Computational parameters of NMD implementation of PNW and SLNW................. 39

Table D-1: The variance and mean layer thickness of type1 and typ2 RLNWs......................... 105

BESTPFE.COM
List of research project topics and materials

Nomenclature

Abbreviations

AC	Auto correlated
AF	Acoustic flexural
A-F	Allen-Feldman
AL	Acoustic longitudinal
AT	Acoustic torsional
BTE	Boltzmann transport equation
BZ	Brillouin zone
DOS	Density of states
EMD	Equilibrium molecular dynamics
GK	Green-Kubo
GNMD	GAMMA-normal mode decomposition
GULP	General utility lattice program
HNTRL	Hetero-nanotwinned random layer
HRL	Hetero-random layer
LAMMPS	Large scale atomic/molecular massively parallel simulator
LJ	Lennard-Jones

LW	Long wavelength
MD	Molecular dynamics
MFP	Mean free path
NEMD	Non-equilibrium molecular dynamics
NMD	Normal mode decomposition
NPT	Constant number of atoms, pressure and temperature ensemble
NTRL	Nanotwinned random layer
NTSL	Nanotwinned superlattice
NVE	Constant number of atoms, volume and total energy ensemble
NVT	Constant number of atoms, volume and temperature ensemble
PGEC	Phonon glass electron crystal
PNW	Pristine nanowire
PR	Participation ratio
RLNW	Random-layer nanowire
SANW	Shell alloy nanowires
SD	Standard deviation
SED	Spectral energy density
SLNW	Superlattice nanowires
SMRTA	Single mode relaxation time approximation

SW	Stillinger-Weber
TC	Thermal conductivity
TE	Thermoelectric
UC	Unit-cell
VC	Virtual crystal

Variables

Greek letters

α, β	Cartesian components
Γ	Line width
γ	Electrical conductivity
δ	Dirac-delta
ϵ	Depth of the potential well of LJ potential
Θ	Array of Eigenvalue component
λ	distance to adjacent unit-cells
ν	Phonon branch
Π	Autocorrelation of Θ
σ	Finite distance at which LJ potential of zero
τ	Relaxation time

ϕ	Potential function
ϕ_2	Two-body potential function
ϕ_{ij}	Pair-wise interaction between i^{th} and j^{th} atoms
Ψ	Phonon SED
ω	Angular frequency
ω_{cut}	Cut-off angular frequency

Roman letters

$\mathbf{a}$	Amplitude vector
C	Volumetric specific heat
c	Concentration of material constituents
$\mathbf{D}$	Dynamical matrix
D	Mode diffusivity
d	Degree of freedom
E	Total energy
$\boldsymbol{e}$	Eigenvector
$\mathbf{F}$	Force constant matrix
$\mathbf{f}$	Force vector
f	Particle density

f_e	Equilibrium particle density
$\mathbf{G}$	Reciprocal lattice vector
$\mathcal{H}$	Hamiltonian
h	Planck’s constant
$\hbar$	Reduced Planck’s constant
I	Eigenvector periodicity index
i, j, j'	Designating atoms
$\mathbf{K}$	Thermal conductivity tensor
K	Thermal conductivity
$\mathbf{k}$	Wave vector
k_B	Boltzmann constant
k_e	Electron governed thermal conductivity
k_l	Lattice thermal conductivity
L	Total length
Lg	Maximum lag
l, l'	Designating unit-cells
m_i	Mass of i^{th} atom
m_A	Mass of Argon atom
m_B	Alloy atomic mass

N	Number of unit-cells
n, n'	Designating modes
n''	Integer
$\langle n \rangle$	Phonon occupation number
P	Number of atoms or particles
$\mathbf{p}$	Momentum vector
$\mathbf{q}$	Heat flux vector
Q	Normal mode coordinates
$\dot{Q}$	Derivative of normal mode coordinates
$\mathbf{R}$	Lattice vector
$\mathbf{r}$	Position vector
$\mathbf{r_i}$	Position vector of i^{th} atom
r_{ij}	Distance between i^{th} and j^{th} atoms
$\mathbf{r}_0$	Equilibrium position
S	Seebeck coefficient
T	Temperature
t	time
$\mathbf{u}$	Displacement vector
V	Volume

$\mathbf{v}$	Velocity vector
$\mathbf{v}_\mathrm{g}$	Group velocity
$\hat{\boldsymbol{x}}$	Unit vector along the X axis
ZT	Figure of merit

Bestpfe.com

CHAPTER 1

Introduction

1.1 Nanostructures

Due to rapid advances in nanoscience and nanotechnology, developing new materials with superior properties is becoming an important engineering endeavour. The term “Nanostructures” is frequently used to recognize those novel materials in which characteristic length scale lies in the range of 1-100 *nm*. One of the important and extraordinary aspects of nanostructures is that those thermal and mechanical characteristics may be very different from the characteristics of corresponding bulk counterparts. For example, graphene and carbon-based nanostructures possess very high thermal conductivity (TC) than their corresponding bulk counterparts [1]; moreover *Si/Ge* superlattices retain lower TC compared to bulk *Si*, *Ge* and *SiGe* alloys [2].

Large varieties of different nanostructures have been introduced, tested and applied in a broad range of applications. The wide applications of nanostructures can be seen in thermoelectric energy conversions, optoelectronic applications etc. A few of the commonly used types of nanostructures are illustrated in Figure 1-1. Nanostructures can be classified

BESTPFE.COM
List of research project topics and materials

according to the relative dimensions of the structures. When all three dimensions are in the same order and nanoscale, the structure is called a 0D nanostructure: examples are Au nanodots and nanoparticles [3]. Structures where lateral dimensions are small compared to the longitudinal direction are called 1D nanostructures such as carbon nanotubes of single [4], [5] and multiple walls [6] and Si nanowires [7], [8]. 2D nanostructures have one dimension significantly small compared to the other dimensions. Examples are Graphene sheets [9], Si nanomesh [10] and silicone nanomesh [11]. In 3D nanostructures none of the dimensions are in nanoscale but nanopatterning was created such as a InGaAsP/InAlAs superlattice [12]. Furthermore, a higher dimensional arrangement of 1D structures can be formed (e.g. hyper-branched nanowires using PbS and PbSe [13] and kinked Si nanowires [14]).

In order to improve performance (e.g. thermal transport, mechanical strength), hetero-nanostructures have been introduced where two or more materials are combined while keeping the layer thicknesses in nanoscale. Some of the examples are Si/SiGe superlattice films [16],[17], graphene/boron nitride superlattice [17] and Graphene hetero-structures [18]. Moreover, combinations of low dimensionality and hetero-structuring were also investigated. For instance, axial hetero-junction Si/Ge nanowires [19] and Si based core-shell nanowire hetero-structures [20] have been reported. Another innovative method is to mix the hetero-structures of different dimensions such as MnAs quantum dots built on the surface of InAs nanowires [21], InAs nanowire built on Si substrate [22] etc.

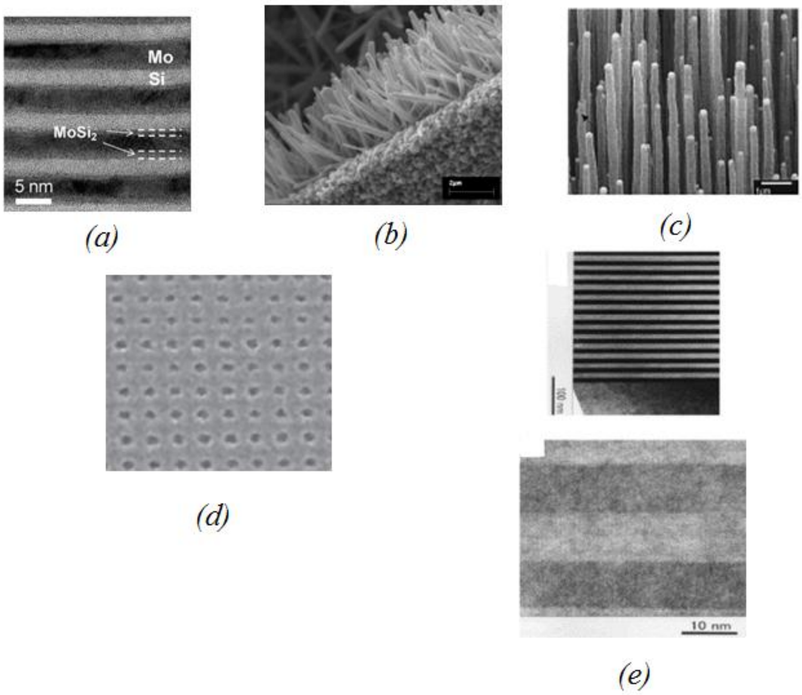

Figure 1-1: Different types of nanostructures (*a*) multi-layers [23] (*b*) *ZnO* nanowires [24] (*c*) Carbon nanotubes [25] (*d*) *Si*nanomesh[10] (*e*) *InGaAsP/InAlAs* superlattice [12]

1.2 Nanostructures in Thermoelectric Applications

Harnessing waste energy emitted by power plants, vehicles etc. is becoming a very important engineering task with the energy crisis and associated environmental issues faced by the world [26]. Thermoelectric (TE) materials demonstrate the potential for being a promising waste recovering technology with their ability to directly convert heat to electricity. More importantly, TE materials offer high reliability, zero pollutants and higher temperature feasible solutions [27]. As far as the environment is concerned, zero pollutant solutions to recover waste energy, thereby reducing fossil fuel consumption and green gas emission are highly admired. The usage of TE materials is not limited to power generation technology but also can be used in refrigeration applications. The Peltier effect is utilized in refrigeration technology and the Seebeck effect in power generation [27]. The key advantage of using TE material governed refrigeration technology is that the systems can be made very compact without fluid circulation and moving components. Therefore, potential applications of TE materials range from waste heat recovery from automobiles to radioisotope thermoelectric generators in deep space missions and seat cooling in automobiles to electronic cooling in integrated circuits [28].

However, the key challenge in utilizing TE materials is their lower efficiency. The efficiency of TE materials is mainly evaluated by the TE figure of merit, *ZT*, which is defined as [26],

$$ZT = \frac{S^2 \gamma T}{k_e + k_l} \tag{1-1}$$

where S, γ, T, k_e and k_l denote the Seebeck coefficient, electrical conductivity, absolute temperature and thermal conductivity due to electrons and lattice structure, respectively. The straightforward rationale of improving the TE figure of merit is increasing the power factor ($S^2\gamma$) while reducing the TC. Historically the power factor has been optimized for narrow-gap semiconducting materials via doping carriers [28], [29] while TC was decreased by adding point defects such as alloying. For example, Bi_2Te_3 systems were alloyed using Sb which yielded better ZT compared to parent materials [30], [31]. However, it is important to note that improving electrical conductivity via increasing carrier concentration leads to higher carrier TC. Furthermore, reducing lattice TC by adding point defects deteriorates the electrical conductivity, demanding a compromise of electrical and thermal conductivities [32]. As far as the power factor is concerned, carrier concentration affects the Seebeck coefficient and electrical conductivity in contrasting ways. As such it demands optimum carrier concentration which maximizes the power factor [33]. Several material systems can be found in the literature where point defect strategy was adopted to increase ZT such as in $SiGe$ [34] and Bi_2Te_3 [30] assemblies. Another approach called phonon glass electron crystal

(PGEC) [35] to enhance the ZT of TE material was introduced where phonons and electrons are made to be propagated through glass-like and crystal-like structures, respectively. Therefore, structures are designed to move electrons freely while phonons are scattered heavily. In PGEC strategy, voids are created inside the structures and filled with other materials, for example, skutterudite is filled with lanthanum, cerium, iron, etc. [36], [37] having ZT~1.4.

Nanostructures can be used to improve the ZT significantly compared to the corresponding bulk materials due to the effect of quantum confinement to the increment of the power factor and/or the effect of larger phonon scatterings to reduce thermal conductivity [26]. For example, a ZT of ~2.4 was achieved using Bi_2Te_3/ Sb_2Te_3 quantum well superlattices of 6nm periodic length [38] despite bulk counterpart yields of only up to a ZT of 1.1. Moreover, nanostructuring improves the ZT of Si nanocomposites, even though bulk silicon is considered as poor TE material. For example, 3.5 times increment of ZT over bulk Si was achieved adding $Si_{1-x}Ge_x$ nanoparticles [39]. Furthermore, nanograined Si composite yielded ZT ~1 at 1173 K as grain size reduced to 10 nm. The nanowires are supposed be an efficient TE material due to the fact their small diameter causes quantum confinement and additional phonon scatterings lead to a higher power factor and lower TC [40]. It was reported that rough Si nanowire of diameter 50 nm fabricated by electroless etching attains the a ZT of ~0.6 at room temperature which has 60-fold improvement over bulk Si [8]. Moreover, Boukai et al. reported that a ZT of ~1 can be achieved by decreasing the nanowire diameter down to 20 nm at 200 K [7]. This higher ZT was attributed to the significant reduction of TC due to phonon-wall scatterings and enhancement of the Seebeck coefficient due to improved phonon drag effect.

1.3 Heat Transfer in Nanostructures

Classically the heat conduction process is described as a diffusion process and is interpreted by Fourier's law given by

$$\mathbf{q} = -\mathbf{K}\nabla T \qquad \textbf{1-2}$$

where **q**, **K** and *T* are heat flux vector, thermal conductivity tensor and temperature, respectively. This law is well-established and proven to be successful in describing the heat conduction process on a macroscopic scale. It was argued that when the length scales associated with heat carriers are comparable or larger than the characteristic length of the medium, the heat conduction process deviates from a diffusive process and thereby, Fourier's law fails in such cases [41]. The type of heat carrier depends on the category of materials such that phonons are the dominant heat carriers in insulators and semi-conductors while electrons dominate in metals. In this study, we are interested in the heat conduction of non-metals, therefore, our focus is limited to phonon-governed thermal conduction

On a nanoscale, the term "ballistic phonon transport" is typically used to designate the propagation of phonons without being subject to scattering (no energy dissipation) for hundreds of nanometres which is different to "diffusive phonon transport" which is governed by temperature gradient [42]. Low temperature also encourages phonons to have ballistic transport which depends on the relative size of the phonon mean free path (MFP) and structure characteristic lengths [43]. Experimental confirmations of the existence of ballistic phonon transport can be found on silicon-nitride membranes at low temperatures [43] and Si membranes at room temperature [44]. Moreover, strong evidence for the ballistic phonon transport of superlattices was provided for AlN-GaN [45] and GaAs-AlAs [46] superlattices where size dependent thermal conductivity was observed experimentally. Depending on the preservation of phase correlations of atomic fluctuations spatially, phonons can also be categorized as wave-like (coherent) or particle-like (incoherent) [47]. Here it is important to note that “ballistic” refers to momentum preserve transport while “coherent” refers to phase preserve transport and these two notions are not necessarily the same [48], [49]. When phonons exhibit coherent behaviour, wave phenomena such as interference [50], tunnelling [51] and localisation [52] are observable and those appearances critically depend on the relative size of structure characteristic length and phonon coherence length [47]. Strong experimental evidence of the existence of coherent phonons of epitaxial oxide superlattices was provided in Ravichandran et al.[53] where crossover of thermal conductivities of superlattices was demonstrated. Crossover is attributed to the change from diffuse phonon to specular phonon transport meaning incoherent to coherent phonon transport [54].

The lower dimensionality of structures also results in anomalous (non-Fourier) heat conduction due to the effect of quantum confinement [55]. Violation of Fourier’s law was first detected numerically for a 1D non-linear lattice known as a Fermi-Pasta-Ulam chain model [56] where divergence of thermal conductivity was observed with the structure total length. This anomalous behaviour is attributed to the momentum conservation of phonons [57]. Moreover, inconsistencies of Fourier’s law prediction at room temperature were identified experimentally with heat conduction in 1D nanostructures such as multi-wall carbon and boron nitride nanotubes [58]. More importantly, it was shown in that study, the anomalous heat conduction occurs even in the cases where structure length L > phonon MFP. Moreover, several studies attempted to establish a connection between anomalous heat conduction to the diffusivity of 1D lattices [59], [60].

1.4 Motivation

This work is primarily motivated by the identification of nanostructures as promising candidates in TE applications. Among different varieties of nanostructures, nanowires, hetero-structures and combinations of both are taken as the focus of this study since their inspiring characteristics lead to lower lattice TC while retaining the same electrical conductivity and Seebeck coefficient of the corresponding bulk counterpart. Furthermore, the objectives of this work are to investigate the phonon-governed heat conduction performance of above-mentioned nanostructures and introduce novel nanostructures of remarkable thermal insulating performance.

Even though nanowires have been investigated extensively, there is still a lack of comprehensive modal analysis of their thermal behaviour. Here what we mean by “comprehensive modal analysis” is the ability to derive the value of thermal conductivity in terms of modal characteristics such as relaxation time, group velocity etc. Moreover, due to the lack of comprehensive modal analysis, some of the unique thermal characteritics of nanowires are not well understood and adequately addressed. These unique thermal characteristics include non-monotonic TC trends over cross sectional area and the effect of shell modifications to the TC. Therefore, this study partly focuses on investigating some of the important thermal behaviours of nanowires by conducting comprehensive modal analysis.

Moreover, as shown in recent studies [49], [61], the thermal insulating performance of superlattices, one of the widely investigated hetero-structures, is outperformed by random layer structures. However, thermal insulating performance of structures with randomly arranged material layers has not been satisfactorily evaluated. For example, the performance of the nanowire form of the random layer structures has not been addressed in the literature.

Therefore, one of the aims of this work is to fill that gap by comprehensively evaluating their performance.

The effect of phonon-grain boundary scattering has been widely addressed in the literature to reduce the TC of nanostructures [62]–[64]. However those studies assumed the particle-like behaviour of phonons, thereby reduced TC due to the phonon-grain boundary scatterings was explained. Recently, a few studies [65]–[67] identified the existence of wave-like phonons in Si twin boundaries (one of the grain boundaries) and subsequently proposed nanostructures which utilized wave-like properties to get further reduction of TC. Based on that finding it is aimed to propose naval nanostructures of remarkable thermal insulating characteristics as efficient TE materials.

As material constituents, Lennard-Jones (LJ) materials, which demand less computational facilities, and Si/Ge which are used extensively in the semiconductor industry are employed in the present work.

1.5 Outline of TheThesis

In Chapter 2, the theoretical foundations of the computational methods used in the study are briefly presented. This chapter contains a summary of classical molecular dynamics (MD) including the direct method and the Green-Kubo (GK) method, the Boltzmann transport equation (BTE) including normal mode decomposition (NMD) and Allen Feldman (A-F) theory.

TC of nanowires is investigated in Chapter 3. LJ fictitious material is used as the material constituent and the NMD method is applied for TC evaluation. Subsequently, results given by the NMD method are verified using the GK method which is based on a fundamentally

Bestpfe.com

different physical perspective to the NMD formulation. The convergence issue of nanowires' TC and the effect of nanowire diameter on TC are investigated scrutinizing the modal contribution, particularly at low frequencies. Furthermore, the effect of shell alloy on the nanowires'TC is probed with the virtual crystal (VC) approximation and contribution of non-propagating modes is estimated via A-F theory.

In Chapter 4, the influence of randomly arranged layer thicknesses on TC is tested for nanowires made of Si and Ge. The thermal conductivities are compared with corresponding superlattice nanowire counterparts to demonstrate the effectiveness of random layer arrangements. Moreover, the effects of cross-sectional width, mean layer thickness, total length, temperature and shell modifications including surface roughness and atomic mixing are examined indicating some anomalous behaviours of TC demonstrated over superlattice counterparts.

Chapter 5 demonstrates phonon localisation due to the twin boundaries of nanotwinned random layer (NTRL) structures. In this investigation, NTRL structures are introduced which are shown to be having reduced TC over superlattice counterparts. Furthermore, combinations of twin boundaries and different material interfaces (Si and Ge) are tested seeking further reduction of TC and compared with the TC of corresponding amorphous structures.

This study is concluded in Chapter 6 stating limitations and related future work.

1.6 List of Articles Prepared

1.6.1 Journal articles

- Samaraweera N, Larkin J M, Chan K L and Mithraratne K 2018 Modal analysis of the thermal conductivity of nanowires: Examining unique thermal transport features *J. Phys. Condens. Matter***30** 225301.
- Samaraweera N, Larkin J M, Chan K L and Mithraratne K 2018 Reduced thermal conductivity of Si/Ge random layer nanowires: A comparative study against superlattice counterparts *J. Appl. Phys.***123** 244303.
- Samaraweera N, Chan K L and Mithraratne K 2018 Reduced thermal conductivity of nanotwinned random layer structures: A promising nanostructuring towards efficient Si and Si/Ge thermoelectric materials *J. Phys. D. Appl. Phys.***51** 204006.

1.6.2 Conference articles

- Samaraweera N, Chan KL, Mithraratne K. Reduced Thermal Conductivity of Nanotwin Random Layer Structures: Effect of twin boundary for phonon localisation. The 4th edition of Nanotech France 2018 International Conference and Exhibition, nanotech France, Paris, 2018.
- Samaraweera N, Larkin J, Chan KL, Mithraratne K. Understanding thermal transport in nanowires. IUMRS-15 th International conference on advanced materials, Kyoto, 2017.
- Samaraweera N, Chan KL, Mithraratne K. Si/Ge random multilayer nanowires with ultra-low thermal conductivity. IUMRS-15 th International conference on advanced materials, Kyoto, 2017.

BESTPFE.COM
List of research project topics and materials

CHAPTER 2

Theoretical Background

2.1 Outline

This chapter presents the theoretical background of the computational methods used in this study. Here the thermal conductivity (TC) of structures is evaluated using molecular dynamic based methods such as the direct method and the Green-Kubo (GK) method. Thus, the discussion is started with a description of molecular dynamic (MD) simulations (section 2.2) and further direct and GK methods are discussed in sections 2.3 and 2.4 respectively. Mode level analysis is one of the crucial parts of this study, therefore, key subject areas needed to understand this approach are presented here, including lattice dynamic calculations (section 2.5), Boltzmann transport equation (BTE) (section 2.6) and normal mode decomposition (NMD) (section 2.7). Finally Allen-Feldman (A-F) theory is discussed in section 2.8 which facilitates to evaluate the TC of disordered solids.

2.2 Molecular Dynamics in Nanoscale Heat Transfer

MD simulation is a real space analysis, dealing with atomic/molecular structures of materials, currently considered as a very powerful tool for investigating the details of nanoscale phenomena. Despite MD being a generic tool for understanding numerous physical aspects of matter, our discussion in this thesis is particularly limited to the heat conduction process. Depending on the strategy to evaluate interatomic forces, MD methods can be differentiated as ab-initio and classical approaches where quantum theory-based sub-atomic particle level evaluations and experimental data-based empirical interatomic potentials are used, respectively [68]. The use of the ab-initio MD method is restricted due to the higher computational demands, therefore, currently it is limited for systems with few atoms [69]. Nevertheless, classical MD simulations can be used for wide range of applications and it is very convenient and practical with respect to the current computational power. However, use of classical MD is limited in cases where quantum effects are critical such as in low temperature (relative to material Debye temperature) [70].Therefore, some works [70]–[72] introduced quantum corrections for classical MD simulations resulting if the system temperature is not near or above the Debye temperature.

The fundamental inputs needed for MD simulations (from this point onward MD simulation refers to its classical form) are the atomic structure of the matter and interatomic potentials which satisfactorily characterize the potential fields among atoms. Newton's second law is applied for translational motion of each and every atom in the structure as given below.

$$m_i \frac{d^2\mathbf{r_i}}{dt^2} = \mathbf{f_i} = -\boldsymbol{\nabla}_\mathbf{i}\phi \qquad \textbf{2-1}$$

where m_i, $\mathbf{r}_i$, $\mathbf{f}_i$ and ϕ represent the mass, position vector, force vector acting on i^{th} atom and resultant potential field of the whole system, respectively. If the system consisting of P atoms and Cartesian components in 3D space is considered, 3P equations have to be solved to get the particle's position and momentum trajectories. Several algorithms are introduced for integrating Newton's equation to improve the computational efficiency while minimising numerical errors. Computationally efficient algoritFhms suggest computationally faster and lower in memory storage. From the physics point of view, selected algorithms must satisfy the time reversible property and thereby energy conservation which Newton's equation possesses. Even though literally none of the available algorithms satisfy the above requirements, it is widely accepted Verlet algorithms are a very good candidate [73]. The Velocity Verlet algorithm is well-known for its easy implementation among other Verlet algorithms.

The evaluation of proper interatomic potential function is the most challenging task of MD implementations since its success substantially affects the accuracy of results. The accurate prediction of potential functions is currently a combined effort of real experiments and density functional analysis [74]. It is a rather acceptable practice to decompose the combined potential energy in a P-atom system as a summation of one body, two body, three body and so on [75]. Thus, the total potential energy ϕ is in the following form.

$$\phi(1,2,\dots,P) = \sum_{i} \phi_1(\mathbf{r_i}) + \sum_{\substack{i,j\\ j>i}} \phi_2(\mathbf{r_i},\mathbf{r_j}) + \sum_{\substack{i,j,k\\ k>j>i}} \phi_3(\mathbf{r_i},\mathbf{r_j},\mathbf{r_k}) + \cdots + \phi_P(\mathbf{r_i},\mathbf{r_j},\dots,\mathbf{r}_{\boldsymbol{P}}) \qquad \textbf{2-2}$$

Here one body potential $\phi_1$represents the effects from walls and external electrical fields on the system. To be useful, it is a necessary condition that $\phi_p$converges to zero immediately

P increases. Lennard-Jones (LJ) potential [76] is the most widely used pair potential function. Among the different variants of LJ potential, LJ 12-6 form

$$\phi_2(\mathbf{r_i}, \mathbf{r_j}) = 4\epsilon\left[\left(\frac{\sigma}{|\mathbf{r_i} - \mathbf{r_j}|}\right)^{12} - \left(\frac{\sigma}{|\mathbf{r_i} - \mathbf{r_j}|}\right)^{6}\right] \tag{2-3}$$

is well recognized as a suitable potential to model the properties of noble elements such as Argon [77]. In equation 2-3, ϵ and σ have the dimensions of energy and length, respectively. The repulsive forces due to the overlapping of inner shell electrons and ions are modelled by the first term on the right hand side of equation 2-3 while second term models the attractive forces due to electrostatic effects. A large number of studies used this potential to demonstrate the heat conduction of matter [49], [61], [78]–[81]. Although, LJ potential is successful in modelling the behaviour of noble elements and some crystals, the stability of diamond structure of tetrahedral semiconductors such as Si and Ge cannot be described in a proper way. Thus, Stillinger-Weber (SW) potential [75] which comprises both two-body and three-body terms, was introduced for diamond lattices such as Si, C, Ge and GaAs. This potential was proved to be capable of replicating mechanical and thermal properties of Si. For example, the heat conduction of Si thin films [79] and nanowires [82], [83] was investigated using SW potential. Tersoff [84], [85] proposed a many-body potential called the Tersoff potential for materials such as Si, Ge. The Tersoff potential has been widely used to predict trends in the heat conduction process of materials, for example, crystalline/amorphous core/shell Si nanowires [86], Si/Ge superlattice nanowires [87], polycrystalline Si nanowires [88], carbon nanotubes [89], etc.

2.3 Direct Method for Evaluating Thermal Conductivity

The direct method is based on non-equilibrium molecular dynamics (NEMD) and is closely analogous with the experimental evaluation of TC. In this method, the structure in which TC must be calculated is sandwiched by heat source and sink similar to the experimental set up. Subsequently two fixed regions are attached to the two extremes of the simulation cell including the structure and two heat reservoirsin order to keep atoms attached in reservoirs.Basically there are two different implementation procedures in the direct method: in one precedure the heat flux is imposed while in the other the temperature gradient is imposed. In the former, a prescribed heat flux is added to the heat source while same amount is removed from the sink in the form of kinetic energy and the system is allowed to develop a steady state temperature gradient. In the latter method, the temperatures of the reservoirs are prescribed and the system is allowed to create a steady state heat flux. However, Lukes et al. [90] showed that the latter method takes a long simulation time for the system to approach a converged heat flux, therefore the former method is employed in this study. Once the steady state temperature gradient is developed in the system, the TC (*K*) is evaluated using Fourier's law as follows,

$$K = \frac{|\boldsymbol{q}|}{\frac{dT}{dx}}$$

where **q** is the prescribed heat flux. Also it is important to note that the prescribed **q** must be big enough to create a large enough temperature difference between the heat reservoirs compared to the statistical temperature fluctuation of the system and small enough to create a linear temperature profile along the structure [91]. Even though the direct method uses finite sized structures to evaluate the TC, techniques were developed to infer the TC of infinitely large structures [92]. A large number of studies can be found in the literature which applied the direct method to evaluate the TC of structures including LJ materials [78], Si,diamond [92] and Si, Si/Ge nanowires [87], [93] etc.

2.4 Green-Kubo Method for Evaluating Thermal Conductivity

The Green-Kubo (GK) method is taken as a key approach to evaluate transport phenomena such as electric current, momentum, heat, etc. [94]. The underlying principle in this approach is to relate the currents due to an externally applied field in a system governed by Hamiltonian dynamics to equilibrium correlation functions of the current. The molecular chaos assumption employed in the Boltzmann transport equation (see section 2.6) is not applied here, therefore, the GK formulation can be applied for both dilute and dense systems. When transportation takes place in a system such as heat conduction, the change of the Hamiltonian is taken as a perturbation to the initial equilibrium Hamiltonian. Thus, the external disturbance which perturbs the initial equilibrium Hamiltonian leads to a small disturbance of the particle density function mentioned above. Linear response theory facilitates establishing the linear relation via the transport coefficient between the external force field and the flux arising due to the disturbance to the particle distribution function. The works of Green [95] and Kubo [96], [97] led to an exact expression based on the fluctuation-dissipation theorem for the linear transport coefficient in terms of time-dependent equilibrium fluctuations of flux. In the case of the heat transport process, the external force field becomes the temperature gradient even though it is internal, while the flux becomes the heat flux vector. Therefore, using the GK formulation the thermal conductivity coefficient is expressed in terms of autocorrelation of the heat flux vector which fluctuates around zero at equilibrium. Therefore, the GK method is based on equilibrium molecular dynamics and the parameters described in the following equations are evaluated using MD simulations. The heat flux vector is defined as,

$$\mathbf{q} = \frac{1}{V}\frac{d\sum_i \mathbf{r_i}E_i}{dt} \qquad \textbf{2-4}$$

where V, $\mathbf{r}_i$ and E_i stand for volume, i^{th} atom's position vector and total energy, respectively. The total energy E_i is the summation of both kinetic and potential energies as given in the following equation

$$E_i = \frac{1}{2}m_i\mathbf{v}_i^2 + \frac{1}{2}\sum_j \phi_{ij}\,(r_{ij}) \qquad \textbf{2-5}$$

wherem_i,$\mathbf{v}_\mathrm{i}$ and $\phi_{ij}\,(r_{ij})$ are mass, velocity of i^{th} atom and pair-wise interaction of i^{th} atom with j^{th} atom when they are apart from the distance r_{ij}, respectively. The lattice thermal conductivity tensor is given by

$$K_{\alpha\beta} = \frac{V}{k_B T^2}\int_0^{\infty} < q_\alpha(0)q_\beta(t) > dt \qquad \textbf{2-6}$$

where $K_{\alpha\beta}$ is the rank-two thermal conductivity tensor. A large body of works can be found which used the GK formulation to evaluate the thermal conductivity of different materials, for example, LJ argon [98], [99], diamond [100] , crystalline Si [92], [101], amorphous Si [72] and Si nanowire [102]. The GK formulation can yield all the components of the thermal conductivity tensor following a single simulation in contrast to the direct method based on NEMD. However, one of the drawbacks of this method is the slow decay of the heat flux autocorrelation function for higher thermal conductivity material compared to lower ones [102].

Bestpfe.com

2.5 Lattice Dynamics

In this section some important concepts in lattice dynamics such as normal mode coordinates, dynamical matrix, Hamiltonian etc. are presented in the limit of harmonic approximation where the potential energy function is approximated to a quadratic form, therefore, the restoring force is proportional to the square of the displacement from the equilibrium position. This fact is clear as the potential energy function is expanded in a Taylor series [103] as shown in below.

$$\phi = \phi(\mathbf{r}_0) + \left(\frac{\partial \phi}{\partial r}\right)_0 . \mathbf{u} + \frac{1}{2!}\left(\frac{\partial^2 \phi}{\partial r^2}\right)_0 u^2 + \frac{1}{3!}\left(\frac{\partial^3 \phi}{\partial r^3}\right)_0 u^3 + \cdots \qquad \textbf{2-7}$$

Here **u** is the small displacement defined as **r-r$_\mathbf{0}$** where **r$_\mathbf{0}$** denotes the equilibrium position of the atom in which potential energy is minimum. The first and second parts of equation 2-7 can be neglected as those represent a constant and a force that vanishes at the equilibrium point, respectively. Therefore, in the harmonic approximation only the quadratic term is considered .

The lattice energy (E) is defined as the sum of the interaction energy of each pair of atoms in crystalline structures. Therefore,

$$E = \frac{1}{2} \sum_{jj',ll',} \phi \begin{pmatrix} jj' \\ ll' \end{pmatrix} \qquad \textbf{2-8}$$

where $\phi\binom{jj'}{ll'}$ denotes the interaction energy between the j^{th} atom in the l^{th} unit-cell and the j'^{th} atom in the l'^{th} unit-cell of a given crystalline structure. Under the harmonic approximation the force constant matrix **F** can be represented as [104]

$$F_{\alpha\beta}\begin{pmatrix} jj' \\ ll' \end{pmatrix} = \frac{\partial^2 E}{\partial u_{\alpha(jl)}\partial u_{\beta(j'l')}} \qquad \textbf{2-9}$$

where u_α,and u_β represent Cartesian displacement vector components. The equation of motion for the j^{th} atom in the l^{th} unit cell can be written as

$$m_j\,\ddot{\mathbf{u}}(jl,t) = -\sum_{j'l'}\mathbf{F}\begin{pmatrix} jj' \\ ll' \end{pmatrix}.\mathbf{u}(j'l',t) \qquad \textbf{2-10}$$

where m_j is the mass of the j^{th} atom.

Taking plane wave assumption, the displacement of the j^{th} atom of the l^{th} unit-cell is given by

$$\mathbf{u}(jl,t) = \sum_{\mathbf{k},\nu}\mathbf{a}(j,\mathbf{k},\nu)\exp(i[\mathbf{k}.\mathbf{r}(jl) - \omega(\mathbf{k},\nu)t]) \qquad \textbf{2-11}$$

where **k**, ν and ω stand for wave vector, phonon branch in the dispersion diagram and angular frequency, respectively. Here summation is conducted over all the wave vectors and phonon polarization.

Substitution of equation 2-11 to 2-10 with some re-arrangements lead to the following form.

$$\omega^2(\mathbf{k},\nu)\mathbf{e}(\mathbf{k},\nu) = \mathbf{D}(\mathbf{k}).\mathbf{e}(\mathbf{k},\nu) \qquad \textbf{2-12}$$

where ***e*** and **D** denote the eigenvector and the dynamical matrix, respectively.

The time dependant complex scalar quantity called normal mode coordinates and those time derivatives are defined such that

$$Q\begin{pmatrix} \mathbf{k} \\ \nu \end{pmatrix}, t\Big) = \frac{1}{\sqrt{N}}\sum_{jl}\sqrt{m_j}\exp(-\sqrt{-1}\mathbf{k}.\mathbf{r}(jl))\mathbf{e}^*(j,\mathbf{k},\nu).\mathbf{u}(jl,t)) \qquad \textbf{2-13}$$

BESTPFE.COM
List of research project topics and materials

$$\dot{Q}\begin{pmatrix}\mathbf{k}\\ \nu\end{pmatrix}, t\Big) = \frac{1}{\sqrt{N}}\sum_{jl}\sqrt{m_j}\exp(-\sqrt{-1}\mathbf{k}.\mathbf{r}(jl))\mathbf{e}^*(j,\mathbf{k},\nu).\dot{\mathbf{u}}(jl,t)) \qquad \textbf{2-14}$$

where N denotes the number of unit cells. These normal mode coordinates represent travelling waves of the crystal structure with unique wave vector and frequency. It is also important to note that the normal modes are orthogonal, therefore, modes are independent of each other.

The Hamiltonian of the crystal within harmonic approximationcan be expressed by normal modes and corresponding derivatives as below [104].

$$\mathcal{H} = \frac{1}{2}\sum_{\mathbf{k},\nu}\dot{Q}\begin{pmatrix}\mathbf{k}\\ \nu\end{pmatrix}\dot{Q}\begin{pmatrix}-\mathbf{k}\\ \nu\end{pmatrix} + \frac{1}{2}\sum_{\mathbf{k},\nu}\omega^2\,Q\begin{pmatrix}\mathbf{k}\\ \nu\end{pmatrix}Q\begin{pmatrix}-\mathbf{k}\\ \nu\end{pmatrix} \qquad \textbf{2-15}$$

In equation 2-15 the first part on theright hand side denotes the kinetic energy while second part denotes the potential energy.

2.6 Boltzmann Transport Equation

The average number of phonons of a given quantum state in a system at equilibrium is given by the Bose-Einstein distribution as below.

$$\langle n\rangle = \frac{1}{exp\left(\frac{\hbar\omega}{k_BT}\right) - 1} \qquad \textbf{2-16}$$

where $\langle n\rangle$ and k_B are the occupation number and Boltzmann constant, respectively. However, when the system does not possess equilibrium, for example, in the case of heat conduction, the above distribution is no longer applicable. Thus, it is needed to formulate a phonon non-equilibrium distribution and governing equation to determine how such a distribution evolves in the system as time advances.

The Liouville equation describes the dynamics of a system in phase space [94]. If there are P particles in a system, the corresponding phase space is $2d \times P$ dimensional space where d is the degree of freedom of a single particle and factor 2 accounts for both generalized spatial coordinates and corresponding momentum coordinates. Now the evolution of a system of particles can be represented using a line in the phase space traced by a single point. The corresponding ensemble of states, a large number of microstates of the system satisfying the same macroscopic constraint, can be depicted by a set of points in the phase space. Since the number of states in the ensemble is enormously large, the representing points of each micro state at t=0 can be taken as a continuum and their time evolution can be viewed as lines analogous to path lines in fluid dynamics. It is important to note that these lines never intersect each other since initial conditions of each state uniquely determine its trajectory in phase space, thereby making points in the phase space conserved as fluid mass conserved in fluid mechanics. The P^{th} particle density is defined as

$$No.ofStates = f^{(P)}\left(t, \mathbf{r}^{(n)}, \mathbf{p}^{(n)}\right)\Delta\mathbf{r}^{(n)}\Delta\mathbf{p}^{(n)} \tag{2-17}$$

in the small volume of the phase space $\Delta\mathbf{r}^{(n)}\Delta\mathbf{p}^{(n)}$ and the conservation of particle density $f^{(P)}$ follows,

$$\frac{\partial f^{(P)}}{\partial t} + \sum_{i=1}^{n} \dot{\mathbf{r}}^{(i)} \times \frac{\partial f^{(P)}}{\partial \mathbf{r}^{(i)}} + \sum_{i=1}^{n} \dot{\mathbf{p}}^{(i)} \times \frac{\partial f^{(P)}}{\partial \mathbf{p}^{(i)}} = 0 \tag{2-18}$$

Since the direct solution of the Liouville equation is not available, a key simplification is imposed to P^{th} particle density called one particle density function with molecular chaos assumption. The molecular chaos assumption treats the particles as independent, therefore, velocities are uncorrelated before and after the collisions and further, collisions are infrequent. Therefore, this assumption is valid only for dilute systems such as phonon gas.

The one-particle density function is defined as an averaging of P^{th} particle density to a state having only **r** and **p,** therefore it is interpreted as shown in equation 2-19.

$$No.\,of States = f^{(1)}(t,\mathbf{r},\mathbf{p})\Delta\mathbf{r}\Delta\mathbf{p} \tag{2-19}$$

Applying this averaging to the Liouville equation yields BTE which contains a particle collision part [105] as shown in equation 2-20.

$$\left(\frac{\partial}{\partial t}+\mathbf{v}.\nabla_r+\mathbf{f}.\nabla_p\right)f(\mathbf{r},\mathbf{p},t)=\left(\frac{\partial f}{\partial t}\right)_{coll} \tag{2-20}$$

where **v**, **f** and *f* denote velocity of particles, external force and one-particle distribution in the phase space, respectively. When the heat transport is addressed via BTE, phonons are taken as carriers and *f* denotes the phonon distribution. Then, taking steady state condition and neglecting external forces, equation 2-20 simplifies to the following form.

$$\mathbf{v}.\nabla_r f(\mathbf{r},\mathbf{p},t)=\left(\frac{\partial f}{\partial t}\right)_{coll} \tag{2-21}$$

Even though, BTE simplifies to equation 2-21, owing to the complicated form of the collision part, it is extremely hard to obtain a solution. To make the collision part simpler, relaxation time approximation is invoked. Here, the collision term is defined as the ratio of equilibrium small fluctuating distribution around f_e and relaxation time τ as shown in equation 2-22.

$$\left(\frac{\partial f}{\partial t}\right)_{coll}=\frac{-(f-f_e)}{\tau} \tag{2-22}$$

Here τ is the relaxation time of a particular particle distribution (i.e. phonons of particular wave vector **k** and branch *v*) and refers to the time taken to achieve the non-equilibrium distribution towards equilibrium distribution. Taking fluctuations as independent of temperature *T*,

$$\frac{df}{dT} = \frac{df_e}{dT}. \qquad \textbf{2-23}$$

By substituting equations 2-22 and 2-23 into 2-21taking phonons with wave vector **k** and branch ν,

$$\left(f\begin{pmatrix}\mathbf{k}\\ \nu\end{pmatrix} - f_e\right) = -\tau\begin{pmatrix}\mathbf{k}\\ \nu\end{pmatrix}\mathbf{v}_g\begin{pmatrix}\mathbf{k}\\ \nu\end{pmatrix}.\boldsymbol{\nabla}_r T\frac{df_e}{dT} \qquad \textbf{2-24}$$

Here $\mathbf{v}_g$ is the phonon group velocity. The heat flux can be written as

$$\mathbf{q} = \sum_{\mathbf{k}}\sum_{\nu}\hbar\omega\mathbf{v_g}\left(f\begin{pmatrix}\mathbf{k}\\ \nu\end{pmatrix} - f_e\begin{pmatrix}\mathbf{k}\\ \nu\end{pmatrix}\right) \qquad \textbf{2-25}$$

Then, thermal conductivity K can be written as

$$K = \sum_{\boldsymbol{k}}\sum_{\nu} C_{ph}\mathrm{v_g}^2\begin{pmatrix}\mathbf{k}\\ \nu\end{pmatrix}\tau\begin{pmatrix}\mathbf{k}\\ \nu\end{pmatrix} \qquad \textbf{2-26}$$

where C_{ph} denotes the phonon volumetric heat capacity.

2.7 Normal Mode Decomposition

Normal mode decomposition (NMD) is a method which can be used to evaluate the phonon relaxation time and anharmonic frequency. This method requires atomic velocities and positions as inputs which can be obtained by MD simulations.Therefore, NMD accounts for the complete anharmonicity of the system beyond the third order of the potential function (see equation 2-7). This fact makes the NMD method advantageous over density functional theory in terms of accounting the full anharmonicity. Furthermore, the fact of relying on empirical potentials adds another advantage from the computational efficiency point of view.

Using the normal mode coordinates the energy associated with mode of wave vector **k** and branch *ν* can be given by,

$$E\binom{\mathbf{k}}{\nu},t\Big) = \frac{1}{2}\dot{Q}\left(\binom{\mathbf{k}}{\nu},t\right)\dot{Q}\left(\binom{-\mathbf{k}}{\nu},t\right) + \frac{1}{2}\omega^2 Q\left(\binom{\mathbf{k}}{\nu},t\right)Q\left(\binom{-\mathbf{k}}{\nu},t\right) \tag{2-27}$$

Here the first term of equation 2-27 illustrates the kinetic energy while the second part depicts the mode potential energy. Furthermore, following the equipartition theorem the expectation value of mode energy *E* can be written as two times the kinetic energy.

$$\left\langle E\left(\binom{\mathbf{k}}{\nu},t\right)\right\rangle = \lim_{t_0\to\infty}\frac{1}{t_0}\int_0^{t_0}\dot{Q}\left(\binom{\mathbf{k}}{\nu},t\right)\dot{Q}\left(\binom{-\mathbf{k}}{\nu},t\right)dt \tag{2-28}$$

The finite value for the relaxation time of phonons gained due to the anharmonicity, existence of defects, boundary etc. results in an exponential decay of the autocorrelation of mode energy with time. Therefore,

$$\frac{E\left(\binom{\mathbf{k}}{\nu},t\right)E\left(\binom{\mathbf{k}}{\nu},0\right)}{E\left(\binom{\mathbf{k}}{\nu},0\right)E\left(\binom{\mathbf{k}}{\nu},0\right)} = \exp\left(-2\Gamma\binom{\mathbf{k}}{\nu}t\right) \tag{2-29}$$

where *Γ* represents the line width. Subsequently, following the Wiener-Khintchine theorem, the phonon spectral energy density (SED) is evaluated using equation 2-29 as shown below omitting the autocorrelation of time derivative of normal mode coordinates in time domain [106], [107].

$$\Psi\left(\binom{\mathbf{k}}{\nu},\omega\right) = \lim_{T_0\to\infty}\frac{1}{2T_0}\left|\frac{1}{\sqrt{2\pi}}\int_0^{T_0}\dot{Q}\left(\binom{\mathbf{k}}{\nu},t\right)\exp\left(-\sqrt{-1}\,\omega t\right)dt\right|^2 \tag{2-30}$$

Following the anharmonic theory [108], the SED given in equation 2-30 is fitted to the Lorentzian function which is centered at $\omega_0\binom{k}{\nu}$ while the full width at half maximum is $\Gamma\binom{\boldsymbol{k}}{\nu}$.

$$\Psi\binom{\mathbf{k}}{\nu},\omega) = \frac{C_0\binom{\mathbf{k}}{\nu}}{2}\frac{\Gamma\binom{\mathbf{k}}{\nu}/\pi}{\left(\omega_0\binom{\mathbf{k}}{\nu}-\omega\right)^2+\Gamma^2\binom{\mathbf{k}}{\nu}} \tag{2-31}$$

where $C_0\binom{\mathbf{k}}{\nu}$ is associated with the average energy of the mode. Therefore, phonon relaxation time is given by [108]

$$\tau\binom{\mathbf{k}}{\nu} = \frac{1}{2\Gamma\binom{\mathbf{k}}{\nu}} \tag{2-32}$$

2.8 Allen-Feldman Theory

When the structure is disordered, it does not possess a periodicity and the concept of wave vector is no longer an appropriate concept, therefore mean free path and group velocity are hard to define for the vibrational modes. In an attempt to explain anomalous behaviour of glasses in which thermal conductivity decreases as temperature decreases contrary to crystalline structures, Kitle concluded that the MFP ~lattice constant, thus, TC~constant irrespective of the structure size [109]. In such cases where the MFP ~lattice constant, the vibrational modes are no longer propagating as assumed in the phonon gas model, therefore, a new approach is demanded.

Allen and Feldman [110], [111] introduced a novel theory (A-F theory) to address an intermediate regime where disorder is sufficient for modes to cause diffuse while insufficient to cause localised, revealing deep insight into the contribution of vibrational modes to the heat conduction process. Their theory was based on harmonic approximation, therefore, material should be stiff enough and/or at low temperature to satisfy the approximation. This study led to some detail and rigorous classification of vibrational modes considering their propagating/diffusing and extended/localised characteristics. Concerning the extended properties, modes are categorized into two groups called extendons and locons and subsequently,extendons are further categorized as propagons and diffusions. The propagons behave similar to phonons which propagate carrying heat with a corresponding group velocity. On the other hand wave vector cannot be defined for diffusions, thus, heat is diffusively transported by them. It is important to note that diffusion is extended throughout the structure unlike locons which is localised in a limited space. Following a Kubo-based harmonic theory, Allen and Feldman formulated an expression mode diffusity of diffusions as,

$$D_n = \frac{\pi V^2}{\hbar^2 {\omega_n}^2} \sum_{n' \neq n} |\langle n|q_z|n'\rangle|^2 \delta(\omega_n - \omega_{n'}) \qquad \textbf{2-33}$$

where D_n and $|\langle n|q_z|n'\rangle|$ are n^{th} mode diffusivity and z component of heat flux operator projected on n and n' eigenstates. Therefore, mode diffusivity can be related to the thermal conductivity as

$$K = \sum_{n} C_n D_n \qquad \textbf{2-34}$$

where C_n represents the n^{th} mode specific heat capacity.

CHAPTER 3

Modal Analysis of the Thermal Conductivity of Nanowires

3.1 Introduction

Investigating the phonon-driven heat transport mechanism of quasi one dimensional (1D) structures such as nanowires, nanotubes and nanoribbons is important because of their potential uses in thermoelectric (TE) applications [40]. The key differences of thermal transport mechanism in low dimensional structures over their bulk counterparts emerges due to phonon confinement and extra phonon-surface scatterings [8], [55], [112]. The origin of the former effect is connected with the relative dimensions of characteristic length of the structure and phonon wavelength [112], [113]. This confinement effect of quasi 1D structures modifies the phonon spectrum, thereby increasing the dominance of long wavelength phonons and reducing phonon group velocities [87], [114]. These distinctive characteristics of phonons give rise to anomalous thermal behaviours over bulk materials. For instance, a universal quantum conductance, quantized limiting value for the conductance, was experimentally demonstrated [115] for a 1D ballistic channel at low temperature as $\pi^2 k_b^2 T/6h$.

Bestpfe.com

Furthermore, the problem of “long wavelengthphonons” and convergence issues of quasi 1D thermal conductivity (TC) with the total length have long been the subject of debate. As discussed in Appendix A, the combined effects of 1D Brillouin zone (BZ), linear dispersion and first-order 3-phonon scatterings inevitably lead to the divergence of TC of 1D structures. Several studies [56], [58], [89], [102], [116]–[121] addressed the convergence issue of quasi 1D structures with different material assemblies and techniques which sometimes led to contradictory conclusions. These contradictory conclusions would be consequences of the material structures analysed and the limitations of the techniques employed in the studies. The purpose of this chapter partly is to shed some light on this convergence issue using the techniques based on the Boltzmann transport equation (BTE) in the limit of single mode relaxation time approximation (SMRTA). Among the different varieties of quasi 1D structures, our study is limited for nanowires. In this study, the TC of nanowires is investigated employing normal mode decomposition (NMD) simulations [81], [107], [122] which are based on BTE-SMRTA and subsequently, equilibrium molecular dynamics. The Green-Kubo (GK) method is used for the verification of the results given by NMD. For the investigation, Lennard-Jones (LJ) materials are used to examine thermal transport of solids with a significantly more reduced computational demand than real materials such as Si and Ge [61], [81], [107], [122]. LJ potential is considered as a suitable inter-atomic potential to evaluate the physical and thermal properties of Argon including solid phase. Tretiakov and Scandolo [99] demonstrated that TC evaluated for solid Argon by MD simulations using LJ potential is in good agreement with experimental values. By varying energy depth (ε) and zero-potential pair separation (σ), materials with different properties (soft or hard) can be derived. LJ potential has been widely used to investigate thermal performance of materials due to less computational demand than real materials. LJ potential is popular among researchers for comprehensive analysis of material properties including thermal performance.

Moreover the investigation of the non-monotonic trends in TC of nanowires with cross-sectional width is another case of this chapter which was addressed before [87], [102], [121] with seemingly different explanations. For example, Karamitaheri et al. [121] attributed the increasing TC trend as cross-sectional width is decreased to the emergence of low frequency modes while Zhou et al. [102] attributed that phenomenon to the dominance of the normal process of acoustic phonons which leads to phonon hydrodynamic flow. We revisit the problem using the system derived from LJ materials mentioned above and suggest possible causes for that non-monotonic trend in the limits of the computational procedure employed here.

Seeking further reduction of TC of nanowires via doping or alloying the entire structure with heavier mass atoms has been tested before [123], [124] experimentally and computationally. Even though significant reduction of TC is achieved, it might adversely affect the electrical conductivity of the structure, and thereby the TE figure of merit [125]. Consequently, alloying or doping was confined only to the shell region [125]–[127], thus, the electrons are free to move through the core region while phonons are disrupted with the shell modifications. Despite the significant reduction of TC of shell alloyed/doping nanowires being attributed to the mode localisation [125], [128] depicted by the mode participation ratio (PR), comprehensive analysis is still lacking.Thus, in this chapter, we develop computational techniques which facilitate analyzing and decomposing the contribution of different vibrational modes to the TC of nanowires in which shell is alloyed with heavier mass atoms.

This chapter is organized as follows. Firstly, the theoretical and computational formalisms of the NMD method are presented including lattice dynamics calculations at the harmonic limit. Subsequently, the NMD implementation is demonstrated and compared with GK simulations using pristine and superlattice nanowires with a discussion pertaining to the convergence of TC of the structures considered here. Subsequently, the non-monotonic

BESTPFE.COM
List of research project topics and materials

behaviour of TC of nanowires is addressed and an attempt is made to explain the trend following the insight given by the NMD method. Then we investigate the effect of shell mass disorder on the TC of nanowires by developing techniques to decompose the influence of different vibrational modes such as propagons and diffusions.

3.2 Theoretical and Computational Formalism

3.2.1 Lattice dynamic calculations

The nanowire structures investigated in this study are built upon a crystalline structure with a face centred cubic lattice. Fictitious LJ materials are used as the material constituents. Therefore, atomic interactions are evaluated following LJ potential in the form of equation 2-3 as shown below.

$$\phi_2(\mathbf{r}_i, \mathbf{r}_j) = 4\epsilon\left[\left(\frac{\sigma}{|\mathbf{r}_i - \mathbf{r}_j|}\right)^{12} - \left(\frac{\sigma}{|\mathbf{r}_i - \mathbf{r}_j|}\right)^{6}\right]$$

where ϵ =3.34×10^{-21} J which is two times the corresponding value of Argon [78] and σ=3.4×10^{-10} m which is the same value as Argon. The mass of an atom (m_A) is 6.63×10^{-26} kg which is the value of the Argon atom and the cut-off radius is kept at 2.5σ. The nanowire's Unit Cell (UC) taken for implementing NMD procedure is shown in Figure 3-1(b). The longitudinal direction is along the X axis where lateral dimensions are along the Y and Z axes. Here BZ is one dimensional and UC is repeated only along the X axis contrary to the bulk structures such as bulk Ar, Si [81] and superlattices [122]. The number of atoms per UC in this particular case is 64 atoms. With this definition, nanowire can be presented as a 1D Bravais Lattice of lattice vector $\vec{\boldsymbol{R}} = n''\lambda\hat{\boldsymbol{x}}$ where λ, n'' and $\hat{\boldsymbol{x}}$ are distance to adjacent UCs, an integer and unit vector along X axis respectively. Furthermore,the reciprocal lattice vector is given by= $\frac{2\pi}{\lambda}\hat{\boldsymbol{x}}$. Then the allowed wave vectors of the nanowire can be obtained from,

$$\mathbf{k} = \mathbf{G}\frac{n}{N_x}$$

Nx is an even integer and n" is an integer which satisfies $\frac{-N_x}{2} < n" \leq \frac{N_x}{2}$.

The lattice dynamics calculations are conducted using the General Utility Lattice Program (GULP) [129] to find harmonic phonon eigenfrequencies, eigenvectors and group velocities. The UC information is fed to the GULP package and the large lateral dimensions are applied to make free nanowire's surface instead of a periodic boundary condition. Figure 3-2(a) shows the dispersion curve of nanowire for the above described UC definition indicating the different acoustic branches where AT, AL and AF refer to acoustic torsional, longitudinal and flexural branches, respectively. Vector plots of the atomic velocities relevant to different branches are given in Appendix B. Furthermore, Figure 3-2(b) shows participation ratios for each mode in harmonic limit. The participation ratio (PR_n) [130] is defined as,

$$PR_n = \frac{\left(\sum_i^P \boldsymbol{e}_{i,n}{}^2\right)^2}{P\sum_i^p \boldsymbol{e}_{i,n}{}^4} \qquad \textbf{3-1}$$

which provides an indication of the localisation behavior of vibration modes at the harmonic limit [131]. Here, $\boldsymbol{e}_{i,n}$ represents the eigenvector of the i^{th} atom of mode n and PR_n varies from 1 to $1/P$ (P represents total number of atoms). The number of atoms participating to a given mode n is equal to $PR_n \times P$. As shown in Figure 3-2(b), the modes do not show any significant localisation since the *PR* of majority of the modes is higher than 0.1.

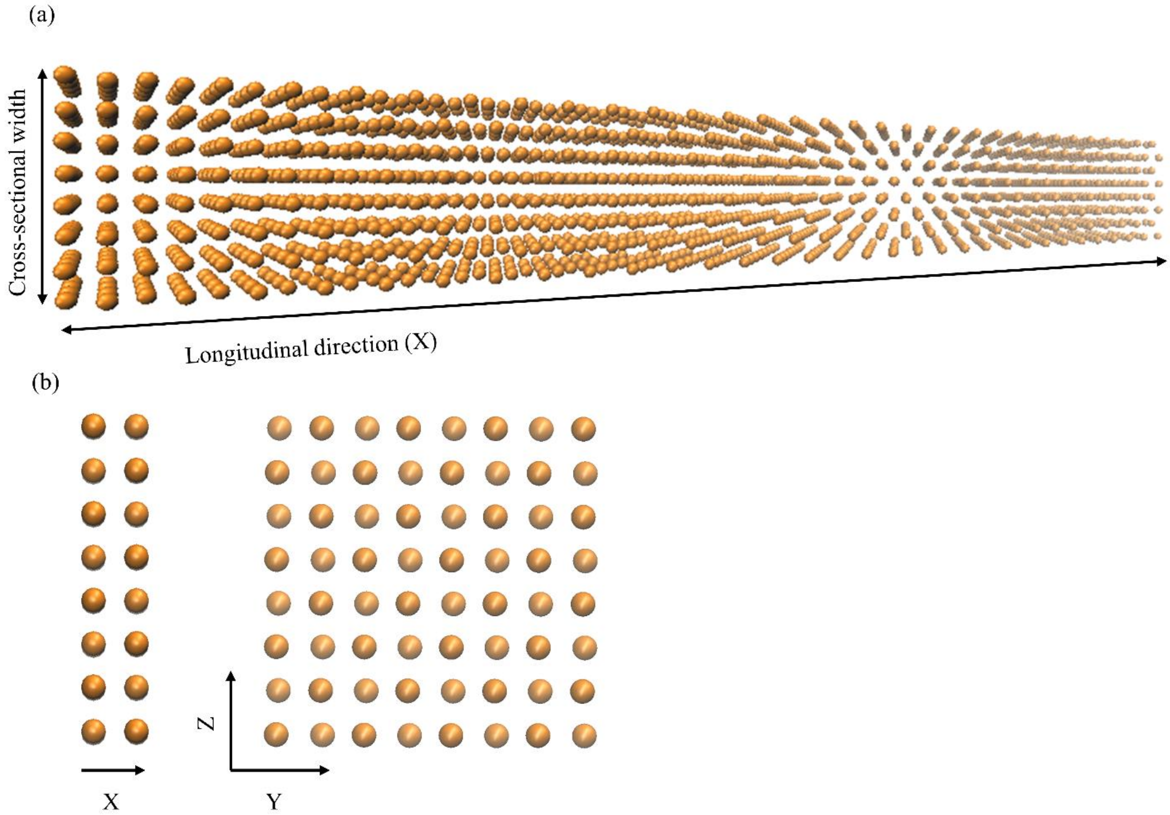
(a)
Cross-sectional width
Longitudinal direction (X)
(b)
X
Z
Y

Figure 3-1: Atomic configurations of (a) nanowire of cross-sectional width 2.1 nm and (b) unit-cell (UC) defined for the nanowire.

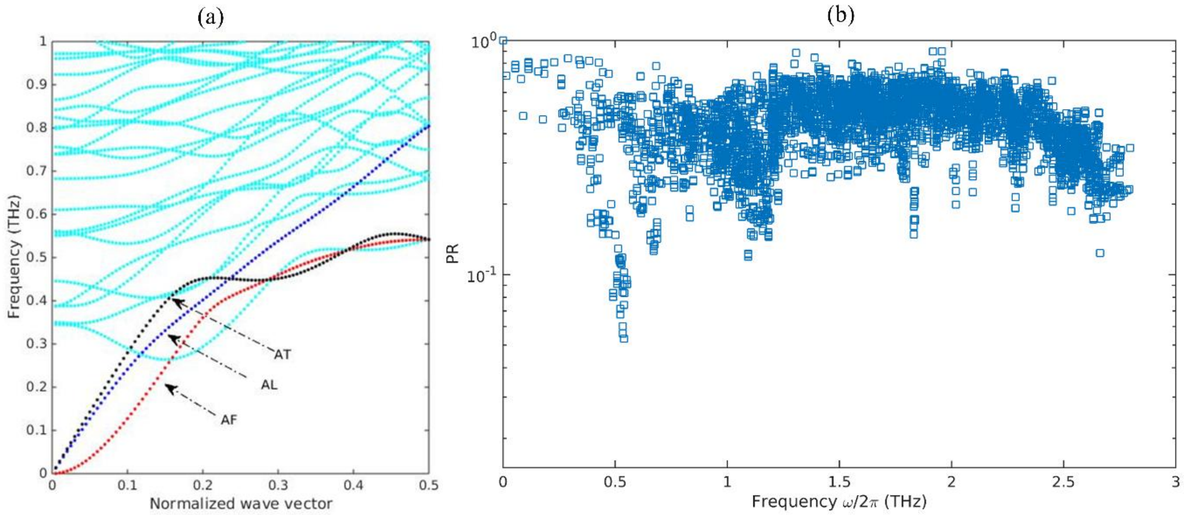

Figure 3-2: (a) Dispersion curve of the nanowire in Figure 3-1. (b) *PR* of modes of nanowire of total length 32 UCs.

3.2.2 Normal mode decomposition

To begin the NMD implementation, first the atomic velocities of nanowire are extracted by EMD simulations. The time step is keptat 2 fs which is in accordance with the arguments stressed in McGaughey(2004) [132]. Periodic boundary conditions are applied along the longitudinal direction while free boundary conditions are imposed along transverse directions. Firstly, the nanowire structure is relaxed in the NPT (constant number of atoms, pressure and temperature) ensemble for 400 ps and once equilibration is achieved, atomic velocity components are collected for a given velocity sampling lag while the structure is running at NVE (constant mass, volume and energy) ensemble for a prescribed total simulation time. The velocity sampling lag is determined as atomic velocity data can capture the system’s highest frequency and the total simulation time is evaluated in accordance with the frequency resolution required to capture the relaxation times accurately. Structure size therefore plays a key role on determination of total simulation time since low frequency phonons (which have a higher relaxation time) get activated as the structure size gets larger.

Therefore the SED of such phonons is extremely narrow. To evaluate the relaxation time of such modes, a higher frequency resolution is important.

Using the atomic velocities sampled, the time derivative of normal mode coordinates is evaluated applying equation 2-14 with the harmonic eigenvectors calculated at wave vector **k** as shown in equation 3-2.

$$\dot{Q}\left(\begin{matrix}\mathbf{k}\\ \nu\end{matrix}, t\right) = \sum_{\alpha,i,l}^{3,P,N} \sqrt{\frac{m}{N}}\, \mathrm{v}_{\alpha}\left(\begin{matrix}l\\ i\end{matrix}, t\right) \boldsymbol{e}^{*}\left(\begin{matrix}\mathbf{k}\ i\\ \nu\ \alpha\end{matrix}\right) \exp\left(\sqrt{-1}\mathbf{k}.\boldsymbol{r}_{0}\left(\begin{matrix}l\\ i\end{matrix}\right)\right) \tag{3-2}$$

Here $\mathrm{v}_{\alpha}\left(\begin{smallmatrix}\boldsymbol{l}\\ i\end{smallmatrix}, t\right)$ represents the α^{th} Cartesian component of velocity **v** of i^{th} atom of l^{th} UC at time t. $\boldsymbol{e}^{*}\left(\begin{smallmatrix}\mathbf{k}\ i\\ \nu\ \alpha\end{smallmatrix}\right)$ and $\boldsymbol{r}_{0}\left(\begin{smallmatrix}l\\ i\end{smallmatrix}\right)$ represent the conjugate of eigenvector and equilibrium position vector of the i^{th} atom of the l^{th} UC. Subsequently, following the Wiener-Khintchine theorem, the phonon spectral energy density (SED) is evaluated using equation 2-30 as shown below omitting the autocorrelation of time derivative of normal mode coordinates at the time domain [106], [107].

$$\Psi\left(\begin{matrix}\mathbf{k}\\ \nu\end{matrix}, \omega\right) = \lim_{T_{0}\to\infty} \frac{1}{2t_{0}} \left| \frac{1}{\sqrt{2\pi}} \int_{0}^{t_{0}} \dot{Q}\left(\begin{matrix}\mathbf{k}\\ \nu\end{matrix}, t\right) \exp(-\sqrt{-1}\omega t) dt \right|^{2}$$

Moreover, following the anharmonic theory[108], the SED shown in equation 2-30 is fitted to the Lorentzian function which is centered at $\omega_{0}\left(\begin{smallmatrix}k\\ \nu\end{smallmatrix}\right)$ while full width at half maximum is $\Gamma\left(\begin{smallmatrix}\boldsymbol{k}\\ \nu\end{smallmatrix}\right)$ as given in equation 2-31,

$$\Psi\left(\begin{matrix}\mathbf{k}\\ \nu\end{matrix}, \omega\right) = \frac{C_{0}\left(\begin{smallmatrix}\mathbf{k}\\ \nu\end{smallmatrix}\right)}{2} \frac{\Gamma\left(\begin{smallmatrix}\mathbf{k}\\ \nu\end{smallmatrix}\right)/\pi}{\left(\omega_{0}\left(\begin{smallmatrix}\mathbf{k}\\ \nu\end{smallmatrix}\right) - \omega\right)^{2} + \Gamma^{2}\left(\begin{smallmatrix}\mathbf{k}\\ \nu\end{smallmatrix}\right)}$$

where $C_{0}\left(\begin{smallmatrix}\boldsymbol{k}\\ \nu\end{smallmatrix}\right)$ is associated with the average energy of the mode. Therefore following equation 2-32 the phonon relaxation time (τ) is given by [108],

$$\tau\binom{\mathbf{k}}{\nu} = \frac{1}{2\Gamma\binom{\mathbf{k}}{\nu}}$$

The BTE is used to evaluate the TC of structures in terms of phonon relaxation times given by normal mode decomposition and phonon group velocities calculated using harmonic lattice dynamics as described above. The application of BTE is valid when modes are phonons which are delocalised plane waves. Following the SMRTA the lattice TC along direction $\hat{\boldsymbol{x}}$ can be written using equation 2-26 as shown below.

$$K_{\hat{\boldsymbol{x}}} = \sum\nolimits_{\boldsymbol{k}}\sum\nolimits_{\nu} C_{ph}\binom{\mathbf{k}}{\nu}\,\mathrm{v}_{g,\hat{\boldsymbol{x}}}^{2}\binom{\mathbf{k}}{\nu}\,\tau\binom{\mathbf{k}}{\nu}$$

Even though the SMRTA fails for materials with large thermal conductivities such as GaN [133] and diamond [134], it has been shown that this approximation can be successfully applied for materials such as Si and LJ Argon [81]. Due to the classical nature of MD simulation which follows the Maxwell-Boltzmann statistics, $C_{ph}\binom{\boldsymbol{k}}{\nu}$ is equal to k_B/V at the harmonic limit [81], [122].

3.3 Results and Discussion

3.3.1 Case Studies: pristine and superlattice nanowires

In this section, we demonstrate the NMD implementation procedure carried out throughout this study using two scenarios: pristine nanowire (PNW) and superlattice nanowire (SLNW). The NMD implementation is carried out for a few stages to minimise the computational cost of the procedure. For the case of PNW of cross sectional width 2.1×2.1 nm^2, the UC contains 64 atoms and 196 modes per given wave vector while SLNW contains 128 atoms and 384 modes per given wave vector. The both systems are kept at 40 K. The atomic masses of the SLNW are m_A and $2m_A$. The existence of long wavelength phonons demands longer nanowire to have proper evaluation of TC making the process extremely computationally expensive. The strategy we apply to circumvent this issue is addressing modes separately as acoustic and optical modes following the nanowire's dispersion curve. As the first step, we take the PNW structure of size ≤ 32UCs and SLNW of size ≤ 32UCs and implement NMD procedure as described in sections 2.7 and 3.2.2 . The velocity sampling lag and the total simulation time are shown in Table 3-1. Subsequently,TC due to the optical phonons is evaluated following equations 2-30, 2-31, 2-32 and 2-26. The optical modes are identified using the information given by the dispersion curves. Figure 3-3 illustrates the cumulative TC given by optical phonons (K_OP) for three different structure sizes over the angular frequency (ω). It can be seen that K_OP is converged at 16 UCs in both structures. Therefore, the structures of 32 UCs yield converged values of K_OP for both cases.

Table 3-1: Computational parameters of NMD implementation of PNW and SLNW.

	STEP 1	*Velocity sampling lag*	*Total time steps*	***STEP 2***	*Velocity sampling lag*	*Total time steps*
PNW	$\leq$ 32 UCs	2^6	2^{22}	$\leq$ 192 UCs	2^9	2^{24}
SLNW	$\leq$ 32 UCs	2^6	2^{22}	$\leq$ 120 UCs	2^9	2^{25}

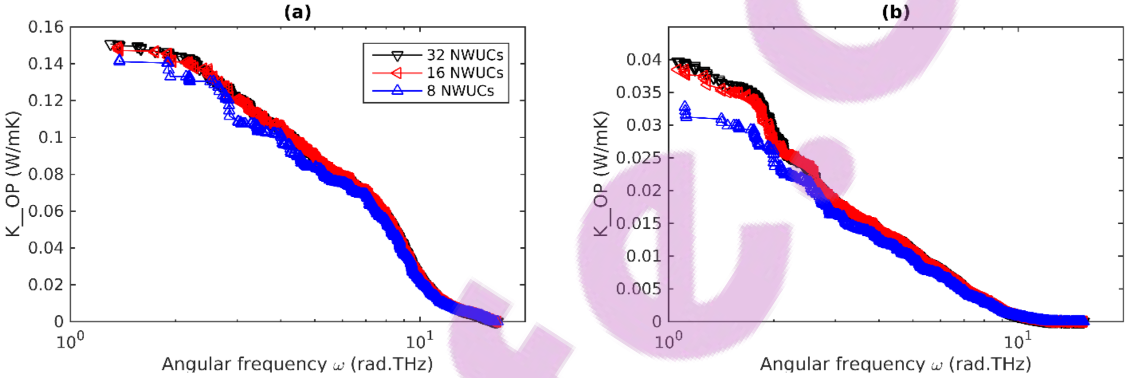

Figure 3-3: Cumulative K_OP of (a) PNW and (b) SLNW.

However, contrary to optical phonons, acoustic branches demand a longer structure to attain the convergence of TC. Consequently, NMD procedure is implemented for PNW structures of size ≤ 192UCs and SLNW structure of size ≤ 120 UCs taking only acoustic branches, which curtail the computational cost significantly. The new velocity sampling and total simulations are shown in Table 3-1for both structures, which are later shown to be large enough to capture the dynamics of acoustic phonons. The phonon relaxation time (τ) against ω evaluated following the two steps described above is illustrated in Figure 3-4 for both structures.

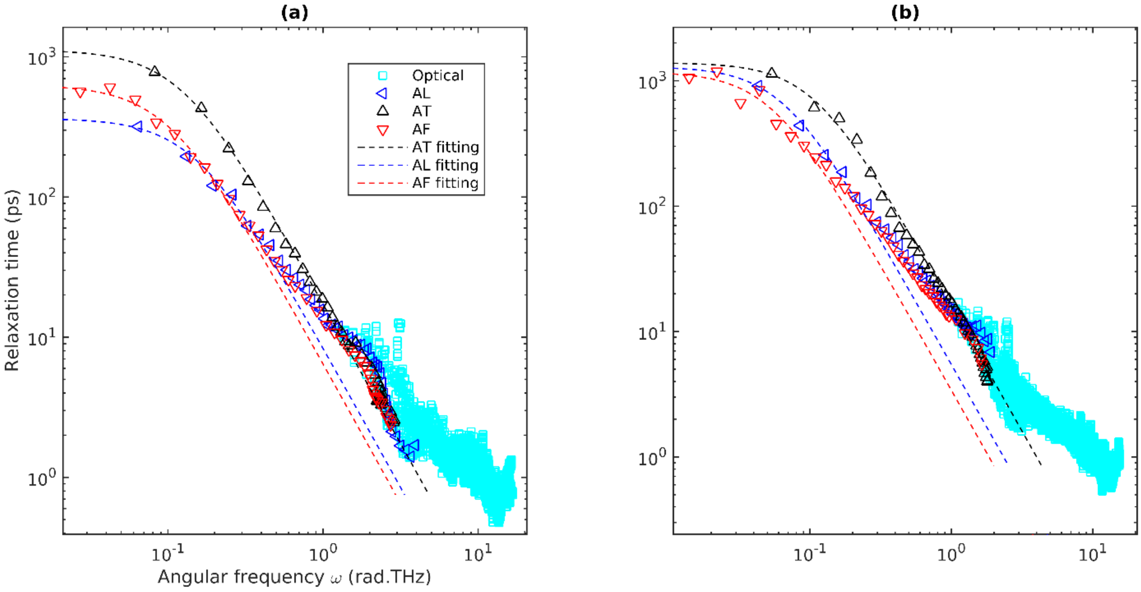

Figure 3-4: Phonon relaxation times of the (a) PNW and (b) SLNW.

It can be clearly noticed that three different acoustic branches follow distinct trends as ω approaches lower values. Moreover, it is interesting to observe that the relaxation time of low frequency phonons tends to attain a constant value contrary to the relaxation time observed in bulk structures before [81], [122] where ω^2 scaling was followed. This trend can be seen very clearly for the AF branch since it extends towards ultra-low frequencies compared to other two branches. This constant trend at lower frequencies could be a result of second-order 3-phonon scatterings as suggested by Mingo and Broido [119]. They showed that the convergence of the TC of carbon nanotubes can be attained by adding an extra term representing second-order 3-phononprocess in addition to the conventional first order 3-phonon scattering term [135] as given below,

$$\frac{1}{\tau} = B\omega^2 T exp\left(\frac{-C}{T}\right) + \ AT^2 \qquad \textbf{3-3}$$

where A, B and C are constants. However, AL and AT branches also indicate some curvature at low frequencies. We assume here that both AL and AT branches follow a similar trend as shown by AF branch at low frequencies. However, carrying out simulations is computationally prohibited as it demands a significantly larger structure. Following Mingo's derivation on second-order 3-phonon scatterings, we fit each branch using the function in the form of $1/(A_1\omega^2 + A_2)$ (see equation 3-3). A better agreement between fitting function and relaxation time values is achieved particularly at low frequencies as depicted in Figure 3-4 indicating the validity of the assumptions we made above.

This agreement is important for attaining a converged TC of the nanowires as length increases. Moreover, this fitting function facilitates extrapolating the relaxation values at ultra-low ωwhich are computationally prohibited to evaluate as stated earlier. This is an important step to evaluate the TC at the limit of infinitely long nanowires since finite size structures offer only a finite number of points in the 1st BZ instead of the entire volume. Therefore, we infer the converged thermal conductivities of each branch utilizing the fitted function (as shown in Figure 3-4) and consequently the total TC. It is important to note that the extrapolation procedure implemented before [136] for bulk materials is not applicable for quasi 1D structures (e.g. nanowires).This is because the DOS of quasi 1D structures no longer exhibits quadratic variation with respect to ω. As shown in the Figure 3-5(a) and (d), AF branches in both structures yield converged TC for the structure sizes considered here. However, there is no guarantee that the other two branches achieve a converged value for the structure sizes taken here. Therefore, the curve fitting procedure introduced in the study assists achieving the points near to the centre of BZ, and thereby the converged value TC. It is important to note that the frequencies at the harmonic limit are taken for the fitting procedure.

BESTPFE.COM
List of research project topics and materials

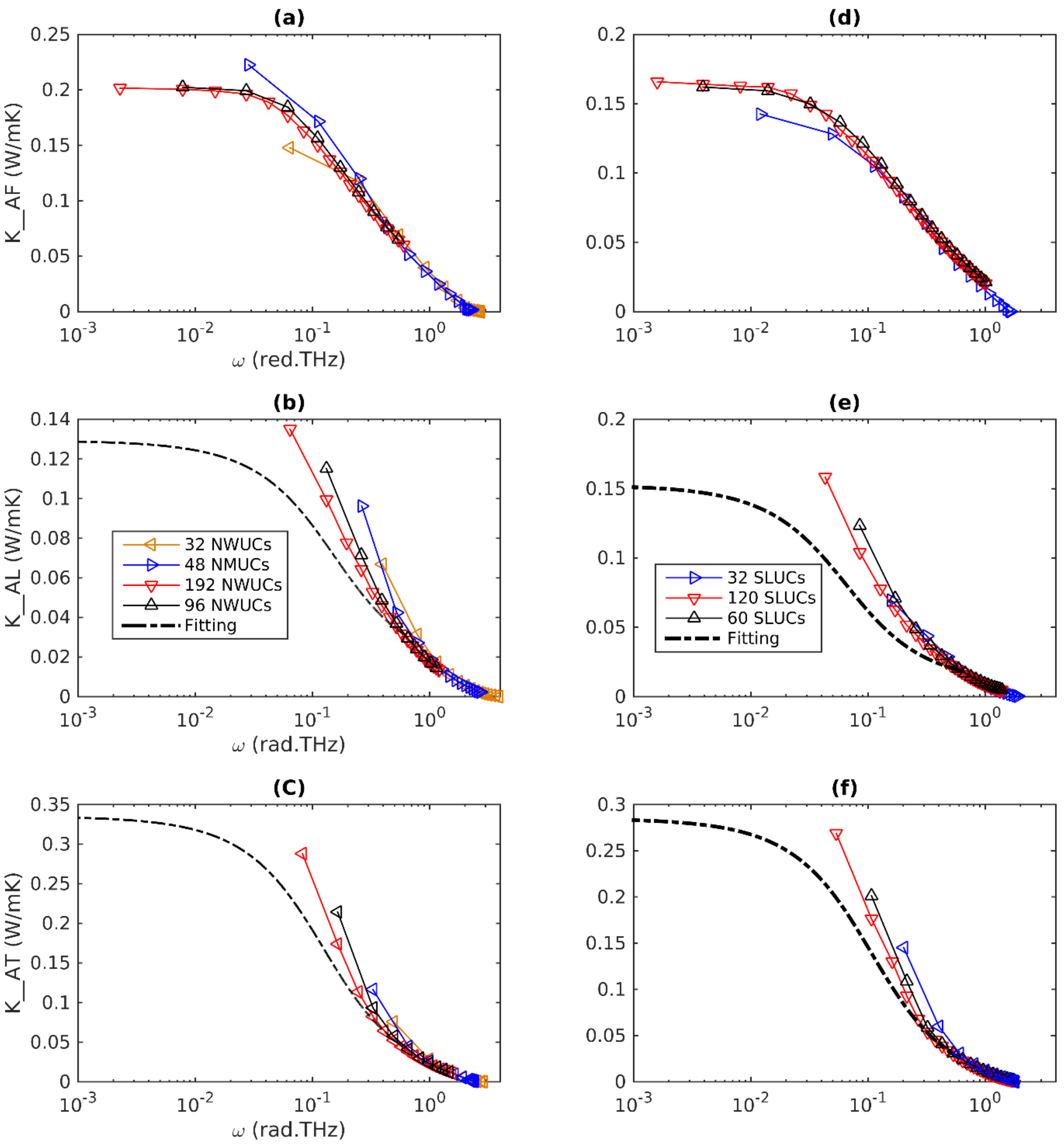

Figure 3-5: Cumulative TC of PNW's (a) AF, (b) AL, (c) AT and SLNW's (d) AF, (e) AL, (f) AT branches over $\boldsymbol{\omega}$ at different structure size.

GK simulations which are based on an alternative physical perspective are implemented to evaluate the TC of structures, in order to verify the procedure mentioned above. This method is used to evaluate the TC of Si nanowires by Zhou et al. [102] demonstrating the ability to have a converged value for TC of Si nanowires. Unlike the BTE based methods such as NMD, the GK method is based on the correlation of heat current which is a fundamentally different way of looking at the heat conduction mechanism. The comparison of TCs evaluated by the NMD and GK methods was conducted for bulk LJ alloys [81] and LJ superlattices [122] showing the close agreement between the results given by both methods. We implement the GK method following the equation 2-6. Here 20 independent simulations are conducted to attain a steady TC curve over the correlation time for both cases as shown in Figure 3-6.

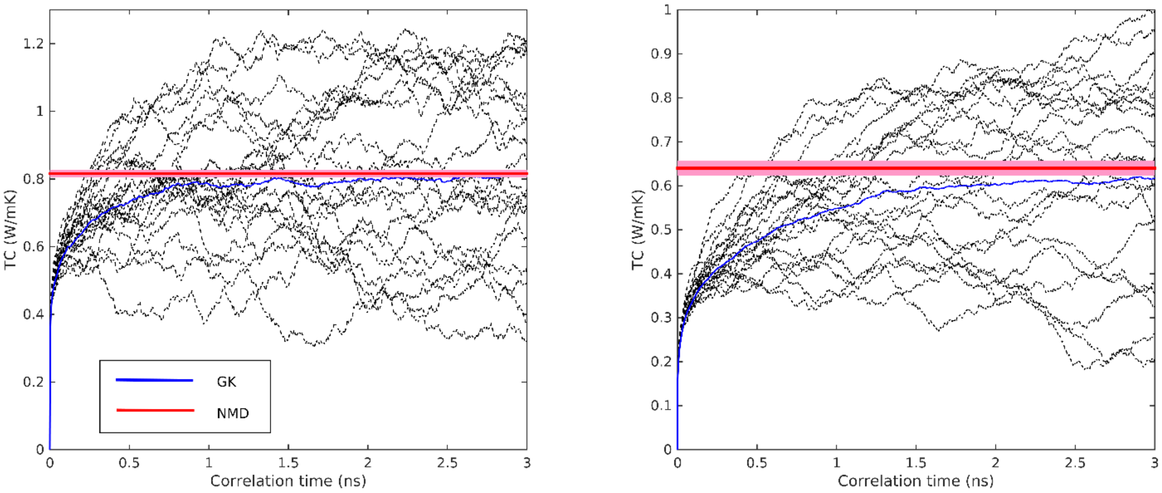

Figure 3-6: Comparison of TC evaluated by NMD and GK methods of (a) PNW and (b) SLNW.

The calculated TC of PNW and SLNW are 0.82∓0.118 and 0.64∓0.171 W/mK respectively. As shown in Figure 3-6 the results given by the NMD procedure described above closely follow the results given by the GK method. The validation given by the GK method, which is free from the assumptions made in BTE-SMRTA, justifies the multi-stepped NMD procedure including the fitting procedure described in this section.

3.3.2 Non-monotonic diameter dependence of TC of nanowires

In this section, we address the non-monotonic diameter dependence of the TC of ultra-narrow nanowires reported before for Si based structures [87], [102], [121]. The non-monotonic trend is first demonstrated using the LJ materials mentioned before using the GK method as shown in Figure 3-7. A minimum of TC can be seen when the width is at 2.6 nm indicating a crossover of the dominance of competing mechanisms of phonon transport at this width. The NMD evaluation is performed for nanowires of cross-sectional widths 2.1, 2.6 and 3.2nm to get more understanding on the competing phonon transport mechanisms. The procedure for the NMD evaluation for these structures is similar to the one followed in the above case studies in section 3.3.1 . As can be seen in Figure 3-7, the NMD evaluated results closely follow the GK ones within 10% difference. Furthermore, the contribution of each acoustic branch and optical modes is illustrated.

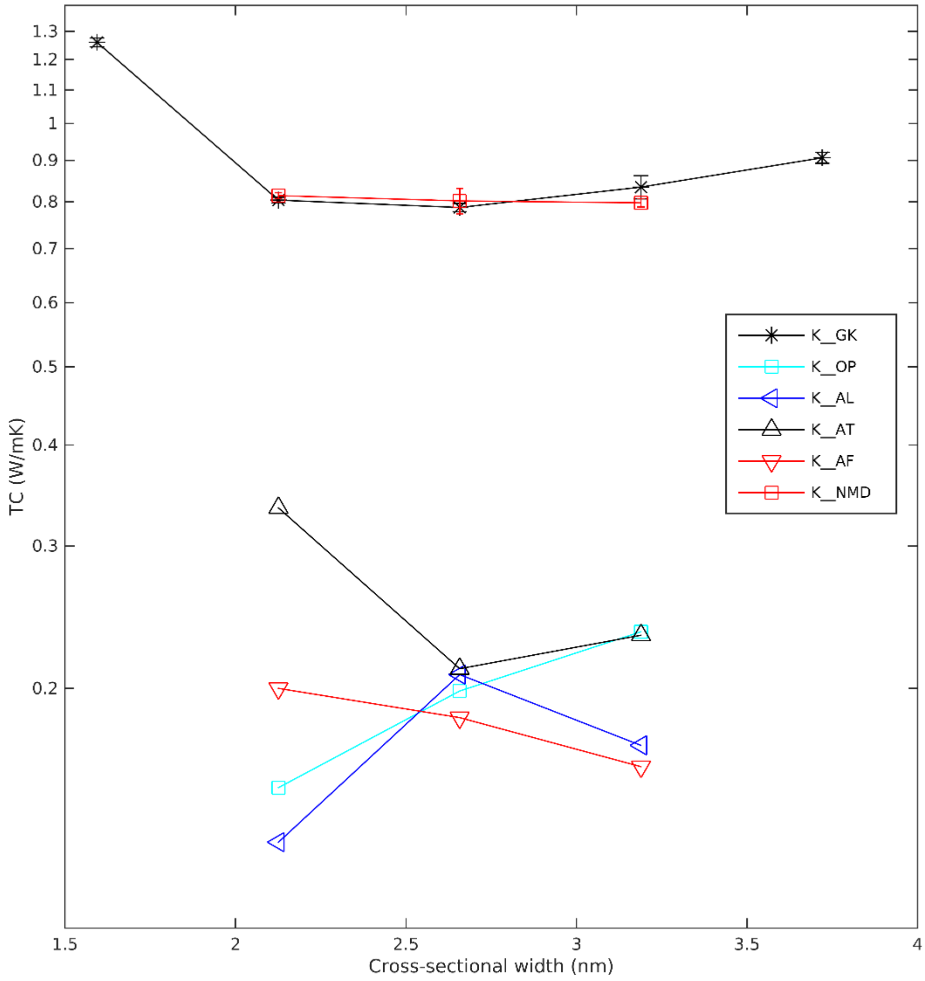

Figure 3-7:TC variation with the NW cross-sectional width.

Figure 3-8(a) illustrates the DOS, evaluated using the velocity autocorrelation function [104], of the three different nanowires with the corresponding bulk counterpart. The DOS is shifted to lower frequencies as cross-sectional width decreases indicating more influence of low frequency phonons for the TC of narrower nanowires. The cumulative TC curves for the structures in Figure 3-8(b) further verify that fact, demonstrating the distinct cumulative trend of nanowires over the bulk counterpart. All the nanowires taken here carry more than 70% of the heat using the phonons of 0-2 rad.THz spectrum while bulk material transports only 10% within that spectrum. As shown in the inset of Figure 3-8(a), nanowires deviate from the ω^2

trend of bulk material giving a constant value of DOS. It is important to note that at very low frequencies the DOS seems to be diverging from the constant DOS due to the effect of flexural modes; however, it does not affect to convergence of TC since the velocity of flexural modes approaches zero at low frequencies.

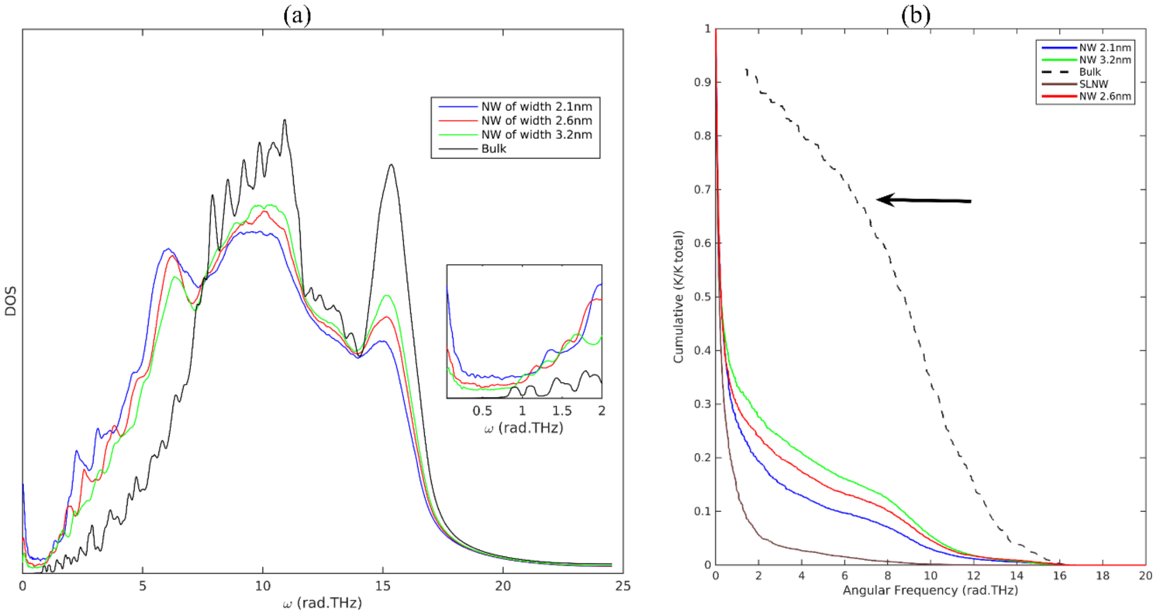

Figure 3-8: (a) DOS over $\boldsymbol{\omega}$. (b) Normalized cumulative TC of structures over $\boldsymbol{\omega}$.

To explain the trends of the TC of different branches shown in Figure 3-7, three important phonon characteristics are considered in the discussion: phonon DOS, group velocities and relaxation times. The phonon group velocity evaluated at the harmonic limit illustrated in Figure 3-9(a) shows lower group velocities for narrower nanowires. Higher DOS and lower group velocities of narrow nanowires stem from the effect of phonon confinement as the nanowire’s cross-sectional width is decreased. Furthermore, the effect of phonon-surface scatterings is shown in Figure 3-9(b), which shows a higher relaxation time as width is increased. This trend remains throughout the spectrum including acoustic modes. Even though the phonon group velocities and relaxation times are getting higher values particularly at low frequencies as cross-sectional width increases, the TC of acoustic branches does not follow the same pattern due to the effect of higher DOS as width is lowered. This effect is critical for the AT branch of the nanowire of 2.1 nm width over the nanowire of 2.6 nm as shown in Figure 3-7. The contribution of the AT branch dominates the total TC of the nanowire of width 2.1 nm compared to its effect on higher cross-sectional width nanowires. Therefore, it can be concluded that a higher TC can be achieved as cross-sectional width decreases from 2.6 nm due to the effect of low frequency phonons and increases again for values larger than 2.6 nm. The latter phenomenon is due to the lesser effect of phonon-boundary scatterings, which is illustrated by higher group velocities, and relaxation times of higher width nanowires. Thus, the key reason for the higher TC before a critical cross-sectional width is the increment of DOS of narrower nanowires. A similar conclusion was attained in the study by Karamitaheri et al. [121] which addressed the thermal transport of Si nanowires based on analytical formulations.

We would now like to compare the treatment of Zhou et al. [102] on a similar case using Si nanowires. In their study, effect of phonon hydrodynamic flow was attributed to the higher TC of narrow Si nanowires and non-monotonic behaviour was described as the competing effect of the dominance of normal and umklapp scatterings. However, the NMD formulation we implemented is based on SMRTA, therefore, all the scatterings are assumed to be momentum destroying and heat dissipative [137], [138]. The close agreement of the TC results given by both the NMD and GK methods indicates that the NMD formulation is accurate enough to evaluate the TC of LJ nanowires taken in this study. More importantly, the ability to model and explain the non-monatomic TC behaviour without considering the hydrodynamic behaviour of phonons suggests that the mechanism proposed in this study is more responsible than the mechanism suggested in Zhou et al. which could sharpen the effect.

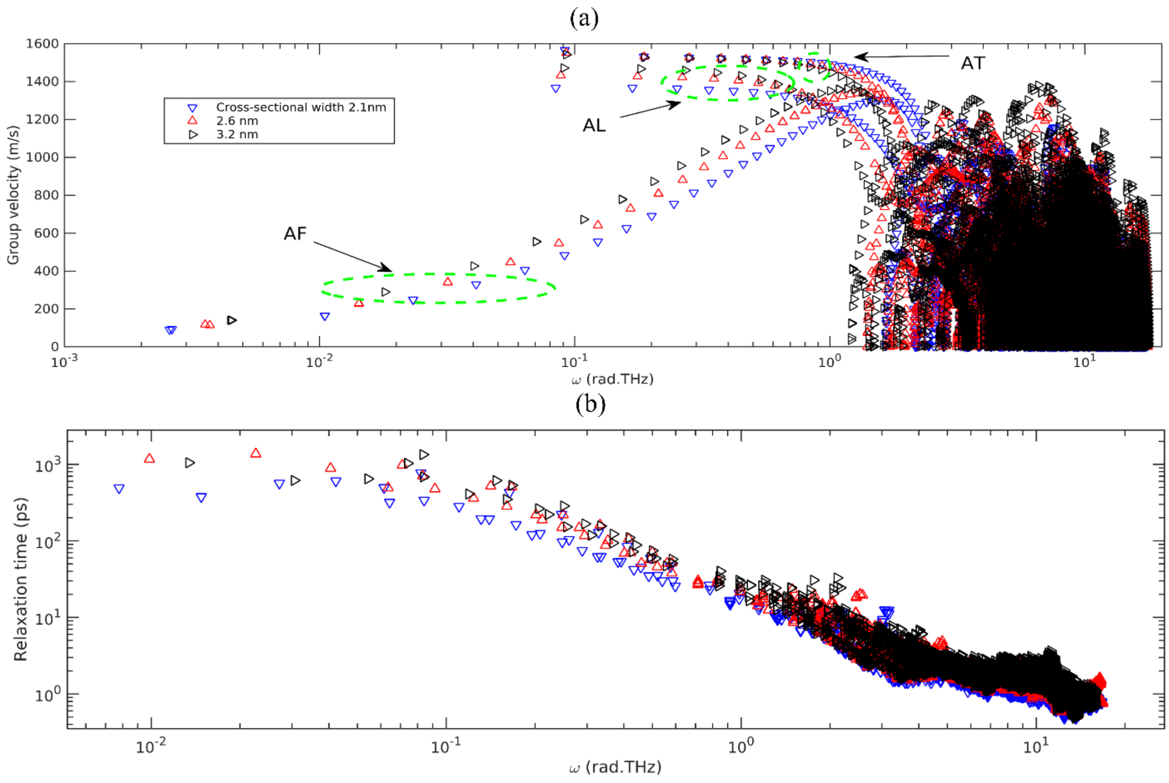

Figure 3-9: Modal (a) group velocity and (b) relaxation time of NWs of three different cross-sectional widths.

3.3.3 TC evaluation of shell alloyed nanowires (SANWs)

In this section, we begin to explore the thermal transport characteristics of shell alloy nanowires (SANWs). For the investigation, PNWs of cross-section 2.1×2.1 nm^2 are taken and 50% of shell atoms are randomly replaced by heavy mass atoms (see Figure 3-10). Here three cases are considered in which alloy atomic masses (m_B) are 2, 3 and 5 times the mass of an Argon atom (m_A). As demonstrated by the seminal work of Allen and Feldman [110], [111], three kinds of modes exist in disordered solids: propagons, diffusions and locons. Propagons, as the name suggests, exhibit propagating behaviour in which aperiodically modulated atomic velocity field can be identified. Therefore, BTE can be used to evaluate the contribution by propagons to the TC of structures. On the other hand, Locons yield a spatially localised velocity field in the structure, therefore their contribution to the TC can be neglected at harmonic approximation. Diffusions are delocalised, the corresponding atomic velocity field features are spatially randomised in contrast to propagons, and mode group velocity is impossible to define. Nonetheless, diffusions actively participate in the heat transport of structures and their contribution to TC is firmly formulated in A-F theory [110], [111] within the limits of harmonic approximation.

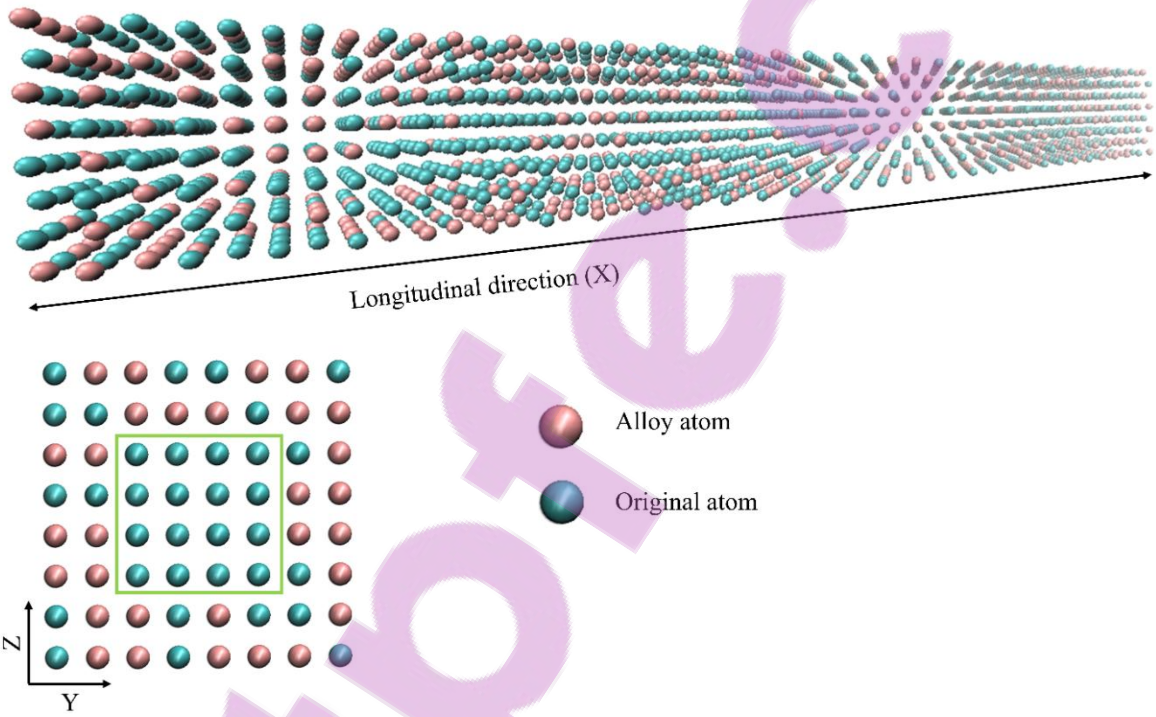

Figure 3-10: Atomic configuration of SANW. The green box encloses the core region of the SANW.

Identification of locons has been known for a long time [130], but there was not a universal technique for identifying diffusions until the work of Seyf and Henry [139] which started using the eigenvector periodicity argument for modes. Before that, Allen and Feldman [110] applied a structure factor-based method to distinguish propagons and diffusions evaluating plane wave characteristics of modes. However, this method lacks generality, as it produces different magnitudes for different materials [139]. Since eigenvectors are directly

Bestpfe.com

related to the velocity field of modes, different spatial behaviour of modes' velocity fields can be revealed through the spatial behaviour of eigenvectors. For example, it is reasonable to accept that corresponding eigenvectors of propagons feature spatial periodicity while diffusions show spatially randomised patterns[139].

Here, we develop an alternative method, which is also based on the same principle of eigenvector periodicity, but correlation techniques are used to identify the spatial pattern of eigenvectors. A method is developed for evaluating eigenvector periodicity of modes in crystalline structures and details of the method are presented in Appendix C. As can be seen in Figure 3-11(a)-(d), SANWs demonstrate distinct deviation from the mode periodicity index I_n =0 (which corresponds to the eigenvector periodicity) after some frequency (see the dotted line in Figure 3-11). By comparing the I_n of the PNW, it can be taken the modes of I_n> 0.2 as non-propagons (diffusions or locons). The propagon/non-propagon boundaries (ω_{cut}) lie at ~2, ~1.75 and ~1.1 THz for the alloy species of mass $2m_A$, $3m_A$ and $5m_A$, respectively, indicating that the higher the alloy mass, the sooner it deviates from the propagon behaviour. Figure 3-11(f)-(h) depicts the localisation of mode due to shell alloying indicating that higher alloy mass leads to more localisation. Interestingly, the limit which shows the distinct change of I_n coincides with the limit that marks the distinct change of PR indicating that shell alloying makes modes' eigenvectors simultaneously more localised and random after that limit.

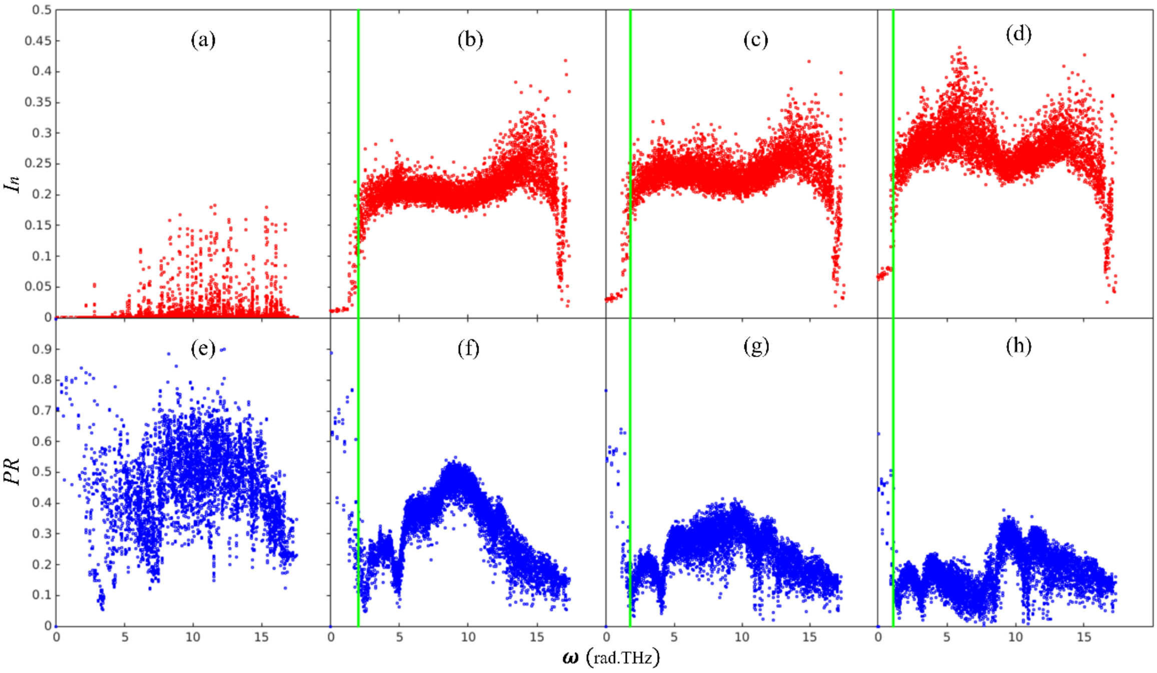

Figure 3-11: I_n of (a) PNW, (b) SANW of m_B=2m_A, (c) SANW of m_B=3m_A and (d) SANW of m_B=5m_A. PR of (e) PNW, (f) SANW of m_B=2m_A, (g) SANW of m_B=3$m_A$and (h) SANW of m_B=5m_A.

BESTPFE.COM
List of research project topics and materials

Once the ω_{cut} is evaluated, the next task is to estimate the TC contribution of different kinds of modes with respective methods. The application of NMD procedure described in section 2.7 is not straightforward to the propagons (modes before ω_{cut}) of the structures which do not possess the periodicity. Thus, we utilize the idea of VC approximation developed by Abeles [140] to evaluate the lattice TC of semiconductor alloys where alloy atoms are scattered randomly. The VC approximation facilitates to define an ordered crystal in terms of the parameters of an actual disordered crystal by treating disorder as a perturbation. Abeles used VC approximation to evaluate the TC of Si/Ge, GaAs/InAs and InAs/InP alloys via Klemens [141]-Callaway [142] theory and found an excellent agreement with experimental results for Si/Ge, GaAs/InAs systems.

The parameters of a virtual crystal are determined as it possesses the same density and elastic constants of the disordered system. Therefore, the atomic mass of a virtual crystal (m_{vc}) is defined as,

$$m_{vc} = \sum_i c_i \, m_i \qquad \textbf{3-4}$$

where c_i and m_i represent the concentration and atomic mass of the i^{th} material constituent. The systems in this study possess only mass disorder confined to the shell region.Therefore, the virtual crystal is defined such that a disordered shell is replaced by an ordered structure of atoms of single mass while keeping the same core structure of the original structure as shown in Figure 3-12. The atomic mass of the new structure is determined according to equation 3-4.The DOS, based on velocity autocorrelation, of the original disordered and new VC are evaluated and compared as shown in Figure 3-13 for the three different structures considered here. It can be seen that corresponding DOS curves closely follow at low frequencies while deviating from each other at high frequencies, but again overlap at highest frequencies.

Furthermore, we have evaluated the phonon relaxation times following NMD at the GAMMA point (GNMD) for the disordered structure and VC-NMD for the newly defined virtual crystal as shown in Figure 3-14. It is interesting to note that the relaxation time trend at low frequencies closely follows the trend observed in DOS curves revealing important characteristics of the VC defined above. The agreement of low frequency phonons is attributed to the similar mass and elastic characteristics which are influential to the behaviour of long wavelength, low frequency modes, of both disordered and VC crystals. Furthermore, a close overlap at highest frequencies can be ascribed to the similar core atomic structure of both crystals.However, the TC contribution of this spectrum is negligible for nanowires. The VC approximation was used by Larkin and McGaughey [81] to evaluate the thermal performance of mass disordered alloy systems such as LJ Argon and Stillinger-Weber (SW) silicon. In their cases, heavy mass species were added to alloy the perfect crystals and lattice dynamics calculations were verified by the GK analysis. Discrepancies were found for the predictions of relaxation times of high frequency modes evaluated for the virtual crystal and real disordered alloy. These discrepancies were notable for higher concentrations of alloy atoms. Moreover, this disagreement led to under-prediction of thermal conductivity of LJ Argon since high frequency phonons play a dominant role for heat conduction in LJ Argon. However, close agreement of the thermal conductivity predictions of SW silicon was attained by both lattice dynamics and GK analyses since the insignificant role of high frequency phonons in Si thermal conductivity. The VC defined here is also capable of accurately modelling the behaviour of low frequency modes which play the dominant role of the TC of nanowires.

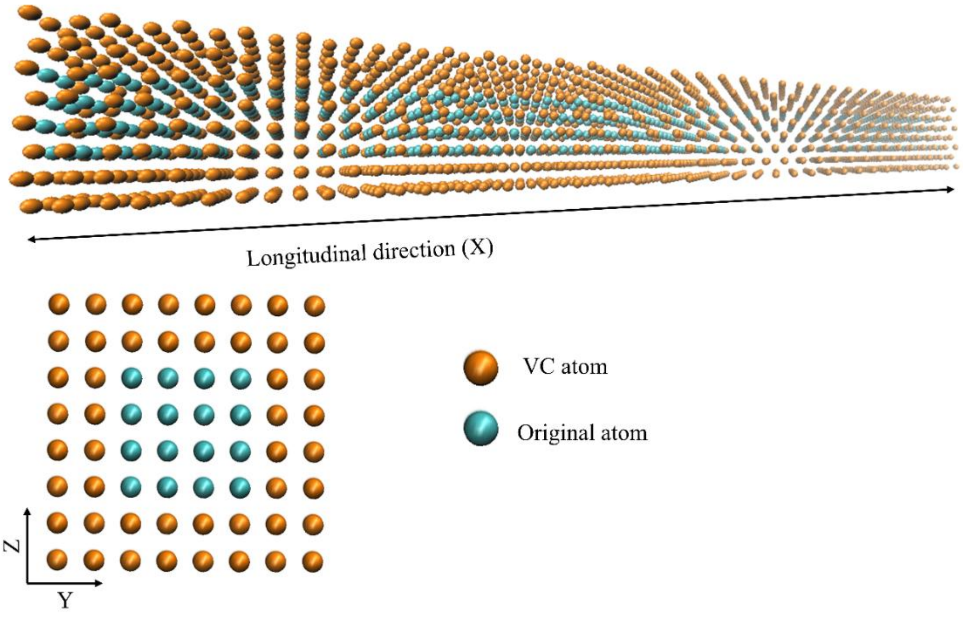
Longitudinal direction (X)
VC atom
Original atom
Z
Y

Figure 3-12: Corresponding virtual crystal atomic configuration for the one shown in Figure 3-10.

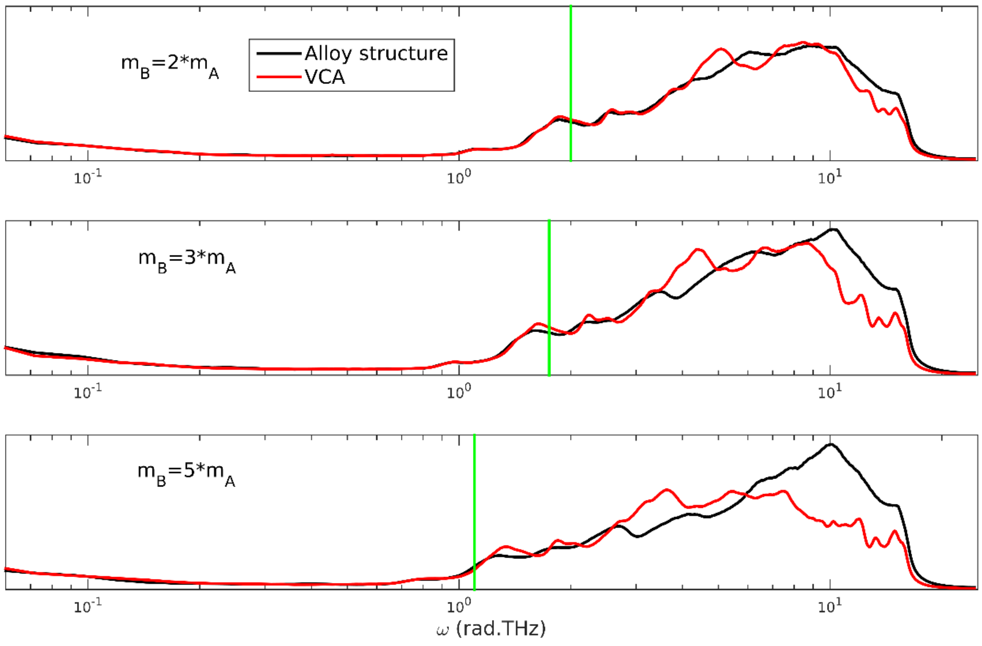

Figure 3-13: Comparison of the DOS of SANW and corresponding virtual crystal structure.

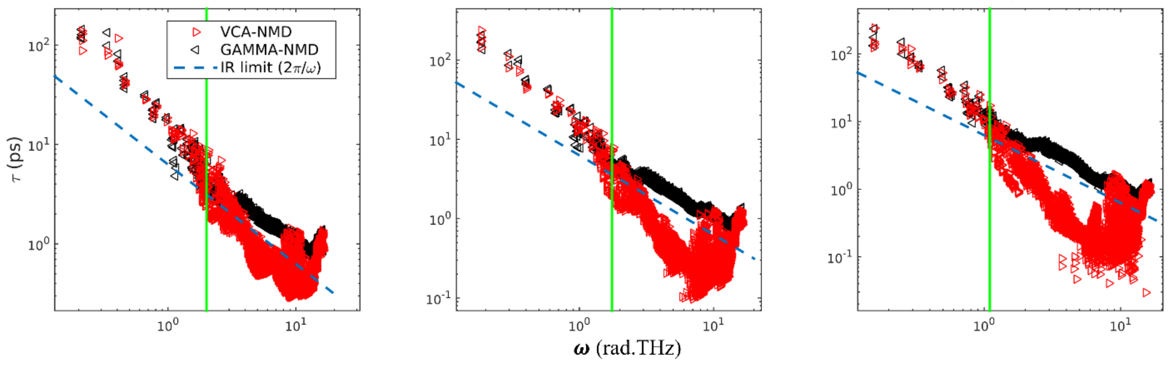

Figure 3-14: Comparison of relaxation times evaluated by VC-NMD and GNMD.

In case of TC evaluation of SANWs, several implications derived in previous discussion must be taken into consideration. The deviation of mode behaviour from propagons to non-propagons as shown above leads to implementing different treatment for TC evaluation discussed so far. However, the depiction of propagons' behaviour by the modes at low frequency can be treated as described before as VC approximation facilitates to do so. To evaluate the contribution of non-propagons to the TC, we follow the A-F theory as described in section 2.8 .

As shown in Figure 3-15, the diffusivities of modes following respective methods are evaluated.

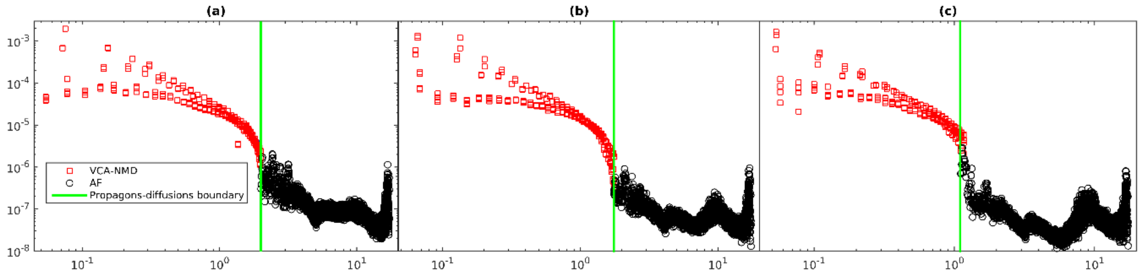

Figure 3-15: Diffusivities evaluate by both VC-NMD and AF for SANWs of alloy atomic mass of (a)$2m_A$, (b)$3m_A$ and (c)$5m_A$.

The TC of SANWs is evaluated with the combined method of A-F and VC-NMD and compared with the GK method as shown in Figure 3-16(a). The K_D evaluated for three different broaden factors are presented in the inset of the figure. As can be seen, there is no significant variation of the values and K_D is evaluated taking the mean of those three values.The gradual decline of K_VC with the shell with heavier mass species can be attributed to the combined effect of low group velocities and large ω_{cut} associated. Furthermore, a similar decline trend can be seen for K_D also due to heavier alloy mass. Thus, one can expect a lower TC with a heavier alloy mass. It is important to point out that the TC calculated by GK analysis is within 10% of the TC evaluated by the combined method of VC-NMD and A-F theories. As shown in Figure 3-16(b), adding heavier alloy atoms led to a shift of dominance of lower frequency modes for the TC. For example, 80% of the heat is transported by the modes of ω less than 1.85, 1.21, 0.80 and 0.52 rad.THz for PNW and SANW of m_B= $2m_A$, $3m_A$ and $5m_A$, respectively.

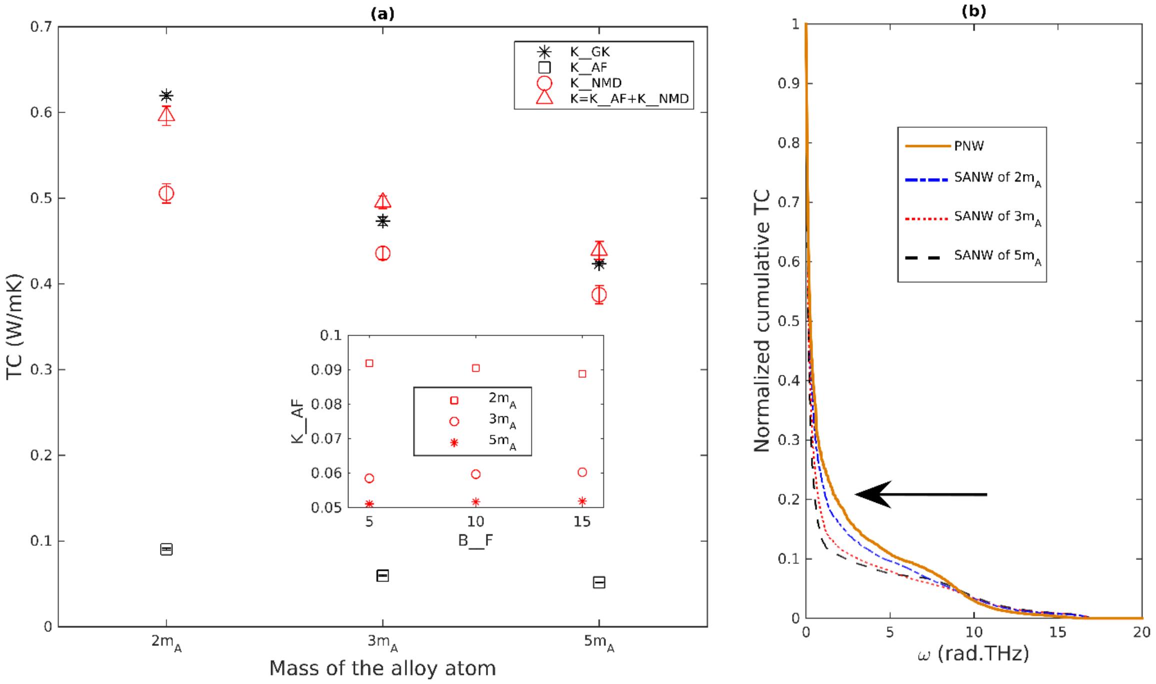

Figure 3-16: (a) TC evaluation different modes of SANWs. (b) Comparison of normalized cumulative TC of SANWs of different alloy mass species and the PNW counterpart.

CHAPTER 4

Thermal Performance of Si/Ge Random Layer Nanowires

4.1 Introduction

Nanostructures yielding ultra-low thermal conductivity (TC) have been receiving significant attention due to their potential applicability in thermoelectric (TE) devices. It has been demonstrated both experimentally and theoretically [7], [8], [143] that Si nanowires can be used as a potential TE material which can achieve up to a two-order reduction of TC over those bulk constituents while retaining the same electrical conductivity and Seebeck coefficient of doped bulk Si [8]. This notable TC reduction of Si nanowires over bulk counterparts is attributed to phonon confinement and phonon-surface scattering [8], [55], [112]. The former leads to modification of the phonon spectrum, thereby reducing group velocity [87], [114]. Furthermore, the larger surface to volume ratio of nanowires causes a phonon-surface scattering effect and hence further reduction of TC can be attained [114]. These two factors make nanowires' heat conduction process different from the bulk constituent as illustrated by the experimental results of Li et al. [144].

Further enhancements of nanowires' TE efficiency along the pathway of reducing TC have been investigated considering different means such as geometric effects [14], [145], [146], doping [147], [148], adding impurities [149] or making defects [150], generating polycrystalline structure [88], change of crystal orientations [65], [151],introducing porosity [152], surface [86], [153]–[155] or interface functionalisation [87], [93], [144], [156]–[158] and any combinations of them. Chen et al. [146] studied the effect of different cross sectional shapes of nanowires on TC and claimed that triangular shapes yield the lowest TC over circular and rectangular shapes of same area due to highest surface-to-volume ratio. The kinked Si nanowires were investigated by Jiang [14] who reported up to 70% TC reduction over straight Si nanowires at room temperature demonstrating phonon interchange and pinching effects are the possible reasons for that.The significant TC reduction due to random distribution of point defects reported in the literature is mainly attributed to high frequency phonon scatterings with defects thereby generating the localised vibration modes. Yang [148] reported an exponentially decreasing TC trend for the case of randomly doping Si isotopes on Si nanowires. In their study, ^{28}Si nanowire doped with 50% of ^{42}Si and ^{29}Si isotopes yielded 27 and 77% of the TC of pristine Si nanowire, respectively, showing the effectiveness of higher mass isotopes that suppress phonon propagation. A strong anisotrophy of TC along different crystal orientations of Si nanowires was observed at room temperature, indicating 50 to 75 % larger thermal conductance along <1 1 0> over <1 0 0> and <1 1 1>[151]. Zhou [88] investigated the TC of polycrystalline Si nanowire and achieved a TC reduction of 77 times less TC over pristine Si nanowires. The reason for such significant TC reduction is attributed to the presence of non-propagating modes and more importantly the suppression of propagating modes.

Improving phonon scattering on the surface of nanowires is another successful approach to obtain significant TC reduction. Surface amorphosization of nanowires was shown to be an effective technique to reduce the TC of Si nanowires significantly [86] due to the presence of non-propagating modes. An experimental treatment for rough Si nanowires was conducted [154], suggesting roughness influences a broadband of phonon spectrum via frequency dependent scatterings that results in reduction of TC of Si nanowires. By incorporating a second material, such as Ge with Si to exploit interface effects, a significant reduction of TC of nanowires has been achieved. For instance, different forms of heterogeneous nanowire structures were suggested in the literature including Si/Ge superlattice nanowires (SLNWs) [87], [144], [157], hierarchical SLNWs [93] and Si/Ge core/shell or vice versa nanowires [156], [158]. Hu and Poulikakos [87] predicted that ~ 92% TC reduction can be achieved by Si/Ge SLNWs with optimal periodic length over pristine Si nanowires. Newly introduced hierarchical SLNWs in which defective layers are added to disrupt the superlattice periodicity, is claimed to have an ~38% reduction over corresponding regular SLNW.

The thermal insulating performance of structures which have randomly organized material layer thicknesses, instead of regular layer ones (superlattice), was tested for fictitious LJ materials [49], [61] and Si/Ge [159]. These studies have reported a lower TC compared to corresponding superlattice structures. Furthermore, in these investigations it was demonstrated that the random alloy limit can be broken for some arrangements [61]. The phonon suppressing mechanism of random multi-layer strctures is thought to be a result of Anderson localisation due to the random nature of layer thickness distribution [49]. The aim of this study is to incorporate the idea of random material layer thickness for nanowires made of Si and Ge and investigate the distinctive thermal behaviours specific to those structures.

The main focus of this chapter is to provide a comparison of TC between random layer nanowires (RLNWs) and corresponding SLNWs at different physical and geometrical conditions. Note that the term ‘random layer’ (RL) is used throughout this paper which is identical to the term ‘random multi-layer’ used by Wang et al. [49]. Furthermore, superlattice

Bestofe.com

(SL) or RL structure implies that the lateral dimensions are infinitely large while a ‘nanowire’ has finite lateral dimensions.

4.2 Simulation Procedures

4.2.1 Constructing random layer structures

All nanowires investigated in this paper are built on the diamond lattice structure of lattice length 0.543 nm. The longitudinal direction lies along the <1 0 0> crystal axis while lateral dimensions are built along the <0 1 1> crystal axis. This particular choice of surface orientation is selected since the other surface orientations were found to be unstable for nanowires resulting in surface disordering [160]. Atoms of the structures are populated keeping epitaxial material interfaces which preserve coherent phonons. Nanowire configurationsare depicted in Figure 4-1.

As the name implies, random layer thicknesses seem rather arbitrary. In this study, however, the simulations are restricted to layer thicknesses with uniform random distribution. The criterion of comparing TC of RLNWs and SLNWs is based on the mean layer thickness [49]. Therefore, a RLNW with particular mean thickness is generated by the random alternative arrangement of sets of Si and Ge layers, and each set follows a uniform random distribution in which mean is equal to the expected mean layer thickness of the structure. The lower bound of the uniform random thickness distribution is a unit cell.

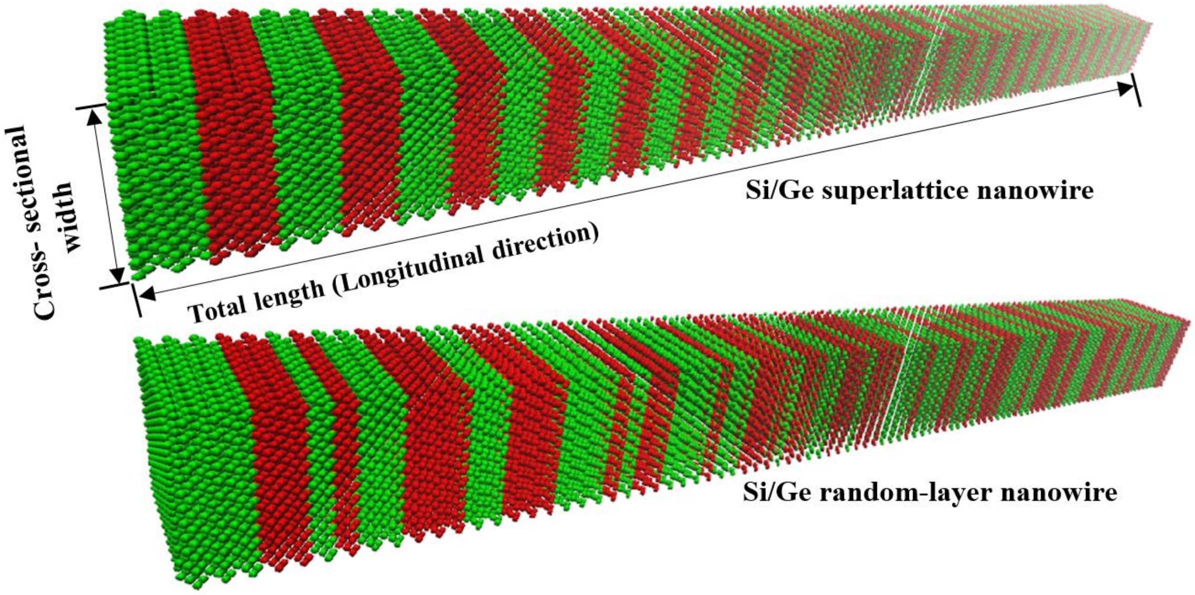
Cross- sectional width
Total length (Longitudinal direction)
Si/Ge superlattice nanowire
Si/Ge random-layer nanowire

Figure 4-1:(top) Atomic configuration of SLNW of mean layer thickness 1.08 nm and cross-sectional width 1.54 nm. (Bottom) Atomic Configuration of RLNW of same mean layer thickness and cross-sectional width.

BESTPFE.COM
List of research project topics and materials

4.2.2 Implementation of non-equilibrium molecular dynamics

The non-equilibrium molecular dynamics (NEMD) method is used to evaluate the TC of the structures and all MD simulations are conducted by an efficient MD solver, Large Scale Atomic/Molecular Massively Parallel Simulator [161] (LAMMPS) package. Furthermore, atomic interactions are modelled by Tersoff potential with the original parameter optimized for Si-Ge systems [85]. The time step is kept at 1 fs. The NEMD procedure of this study is basically similar to the method followed by Hu and Poulikakos [87] and is, briefly, as follows.

The nanowire structure is sandwiched by a heat source and a heat sink and two additional regions are added to the two extremes of the structure to prevent atoms in baths from sublimating. Free boundary conditions are applied in lateral directions and periodic boundary conditions are applied along the longitudinal direction (Figure 4-1). Initially the structure is relaxed along the longitudinal axis corresponding to the zero pressure keeping in NPT ensemble for 4 - 6 ns depending on the number of atoms. After that the structure is further relaxed 1 ns for each in NVT and NVE ensemble respectively. Once the structure is fully relaxed following the above procedure, a HEX algorithm [162] is implemented by adding heat flux to the source while removing same amount from the sink. Simulations take 20-50 ns to achieve steady state depending on the size and type of the structure and simulations continue for an additional 10 -15 ns to evaluate the steady state temperature field along the longitudinal direction (see Figure 4-2). Basically, two different methods can be found in the literature to evaluate the temperature gradient (dT/dx) of structures in NEMD implementations. Hu et al. [87] and Mu et al. [93] obtained dT/dx by fitting the linear portion of the temperature profile along the structure avoiding the non-linear effects near the heat baths. However, Samvedi and Tomar [163] and Wang et al. [49] argued differently that the non-linear effects at interfaces (thermal resistance) nearest to the baths are attributed to the filtering of phonons not following the dispersion of multilayer structures. Thus, dividing the temperature difference by the length of the nanowire accurately captures the interface effects. Therefore, the latter procedure to evaluate the temperature gradient is followed.

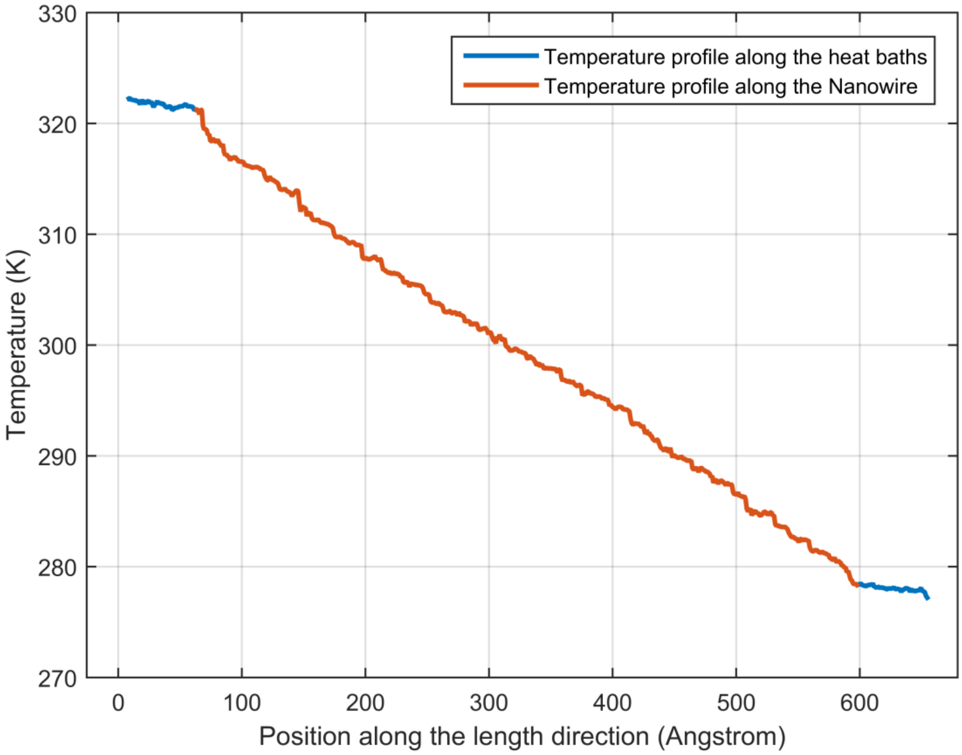

Figure 4-2: Temperature profile of a RLNW of 52.1 nm long.

4.2.3 Implementation of GAMMA-normal mode decomposition

For GAMMA-normal mode decomposition (GNMD) implementation, all the MD simulations are done using LAMMPS [161] and harmonic eigenvectors are evaluated using the GULP [129] package. The procedure is similar to the one described in section 3.2.2 , but the wave vector **k** is kept at the GAMMA point only. Firstly, structures are relaxed in the NPT ensemble for 500 ps. The time step is kept at 1fs. Subsequently the system is run in 2^{23} timesteps in the NVE ensemble and atomic velocities are collected every 2^4 time steps. The sampling frequency is selected according to the maximum frequency the structure possesses.

Using the atomic velocities sampled, the time derivative of normal mode coordinates is evaluated using the harmonic eigenvectors calculated at the GAMMA point as shown in equation 4-1.

$$\dot{\boldsymbol{Q}}\begin{pmatrix}\boldsymbol{k}=0 & \\ \nu & ,t\end{pmatrix}=\sum_{\alpha,i}^{3,P}\sqrt{m}\mathbf{v}_{\alpha}(i,t)\boldsymbol{e}^{*}\begin{pmatrix}\mathbf{k}=0 & i\\ \nu & \alpha\end{pmatrix}\exp\left(\sqrt{-1}(\mathbf{k}=\mathbf{0}).\mathbf{r}_{\mathrm{i}}\right) \qquad \textbf{4-1}$$

Here $\mathrm{v}_{\alpha}(i,t)$ represents the α^{th} Cartesian component of velocity **v** of the i^{th} atom at time *t*. ***e*** and $\mathbf{r}_i$ represent the eigenvector and equilibrium position vector of the i^{th} atom, respectively. Subsequently, following the Wiener-Khintchine theorem, the phonon spectral energy density (SED) is evaluated using equation 4-2 as shown below omitting the autocorrelation of time derivative of normal mode coordinates at the time domain [106], [107].

$$\Psi\begin{pmatrix}\mathbf{k}=0 & \\ \nu & ,\omega\end{pmatrix}=\lim_{t_0\to\infty}\frac{1}{2t_0}\left|\frac{1}{\sqrt{2\pi}}\int_{0}^{t_0}\dot{Q}\begin{pmatrix}\mathbf{k}=\mathbf{0} & \\ \nu & ,t\end{pmatrix}\exp(-\sqrt{-1}\omega t)dt\right|^{2} \qquad \textbf{4-2}$$

Finally the anharmonic mode frequency ω_0 and linewidth are predicted by fitting the SED to a Lorentzian function and subsequently the phonon relaxation time (τ) is evaluated as described in sections 2.7 and 3.2.2 .

4.3 Results and Discussion

4.3.1 Mode level analysis of SL and RL structures

As will be demonstrated in this study, the structures with random layer arrangements (RLs or RLNWs) always demonstrate improved thermal insulating performance over corresponding regular layer ones (SLs or SLNWs) at different physical and geometrical conditions. Therefore, our focus is first directed towards the mode level properties of structures which would shed some light on the nature of vibrational modes and possible causes of reduction of TC.

The Participation Ratio (PR_n) (see equation

3-1) is evaluated for both SL and RL structures as illustrated in Figure 4-3(a). It can be seen a distinct localisation effect for phonons in the RL structure over SLs indicating the effect of random layer arrangement on the mode spatial extension. Further, the higher the total length of RL structures, the more suppression of modal spatial behaviour can be seen as shown in Figure 4-3(b). It can be taken that the lower TC given by the structures of random layer arrangement over their regular counterparts emerges due to the degree of localisation of modes.

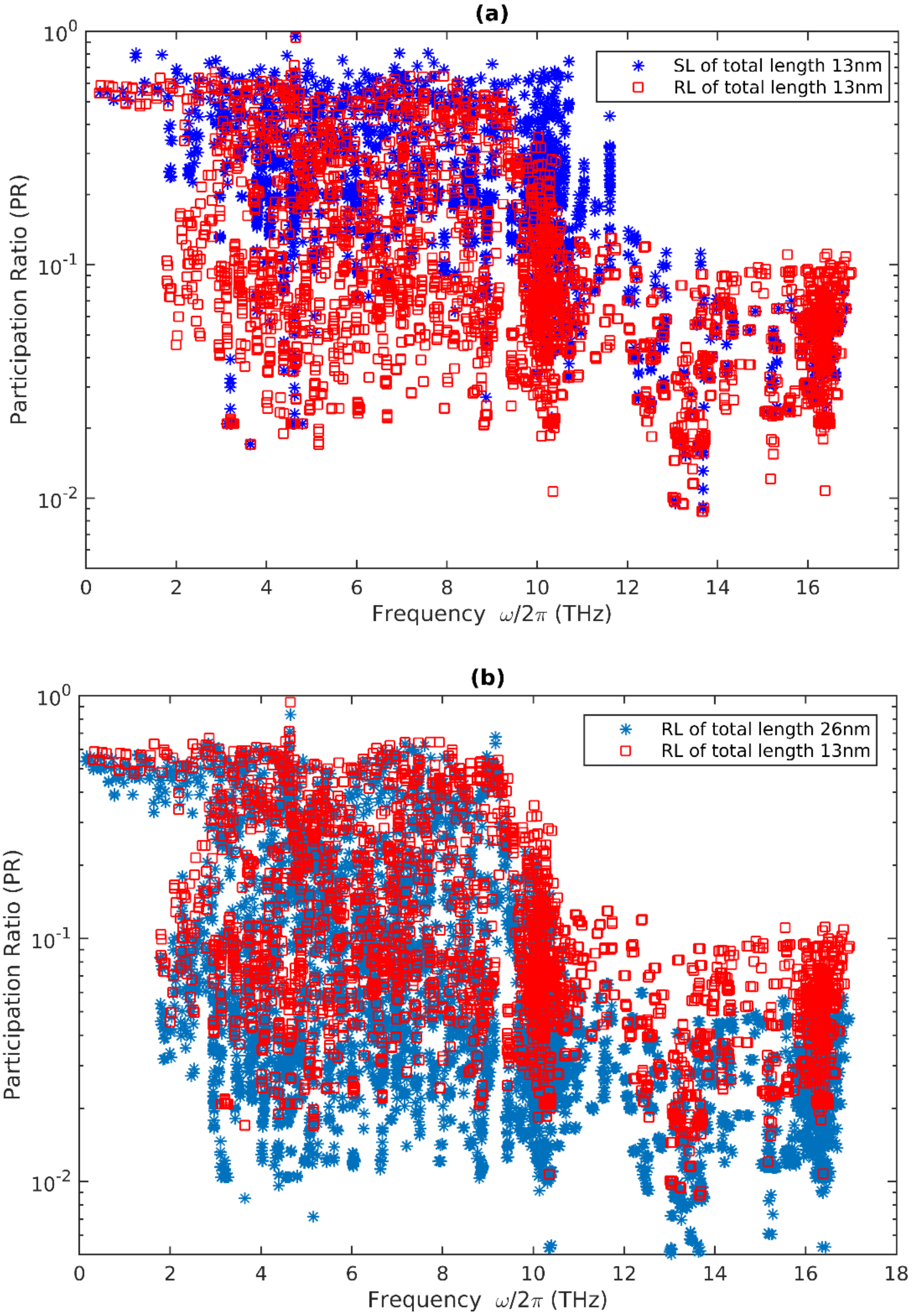

Figure 4-3: Comparison of PR of (a) SL and RL structures and (b) RL structures of different total lengths.

NMD is conducted to evaluate the mode relaxation times of RL and SL structures. For NMD implementation, the supercell of structures of dimensions $13\ nm \times 1.54\ nm \times 1.54\ nm$ are taken. The wave vector is kept at the GAMMA point since periodicity cannot be applied for the RL structure. Atomic velocities are mapped to the time derivative of the vibrational mode coordinates $\dot{Q}\left(\begin{matrix}\boldsymbol{k=0}\\ \nu\end{matrix}, t\right)$ and the phonon spectral energy density [107] (SED) of a mode of angular frequency ω and branch ν is evaluated. Subsequently, the Lorentzian function is used to fit the energy density as shown in Figure 4-4(a) in SL and (b) in RL structures for selected modes against the frequency spectrum.The NMD analysis on SLs was done previously [122] where plane wave characteristics of modes were illustrated. Having well-defined peaks of energy spectrum is considered as an indication of plane wave characteristics of modes [81].

As demonstrated in Figure 4-4(a) and (b), the selected modes of the RL structure also yield well-defined peaks for the mode energy densities similar to its superlattice counterpart. Figure 4-4(c) illustrates that the mode relaxation time is evaluated for both SL and RL structures. The majority of mode relaxation times of the RL structure closely follow those of the SL structure, and furthermore, at low frequencies, mode relaxation times follow the ω^{-2} scaling in both structures indicating 3-phonon scatterings due to the anharmonic effects [142]. However, some modes (few in number) at mid and high frequency spectrums in the RL structure deviate from the trend acquiring low relaxation times. Further, it is identified that the energy spectrum of these deviated modes demonstrates ill-defined peaks. As a whole, it can be taken that both structures possess similar phonon scattering properties, even though their layer arrangements are different (regular and random). This result is consistent with the claim made by Wang et al. [49] that both RL and SL structures possesses similar phonon properties except the localisation experience by modes in RL structures.

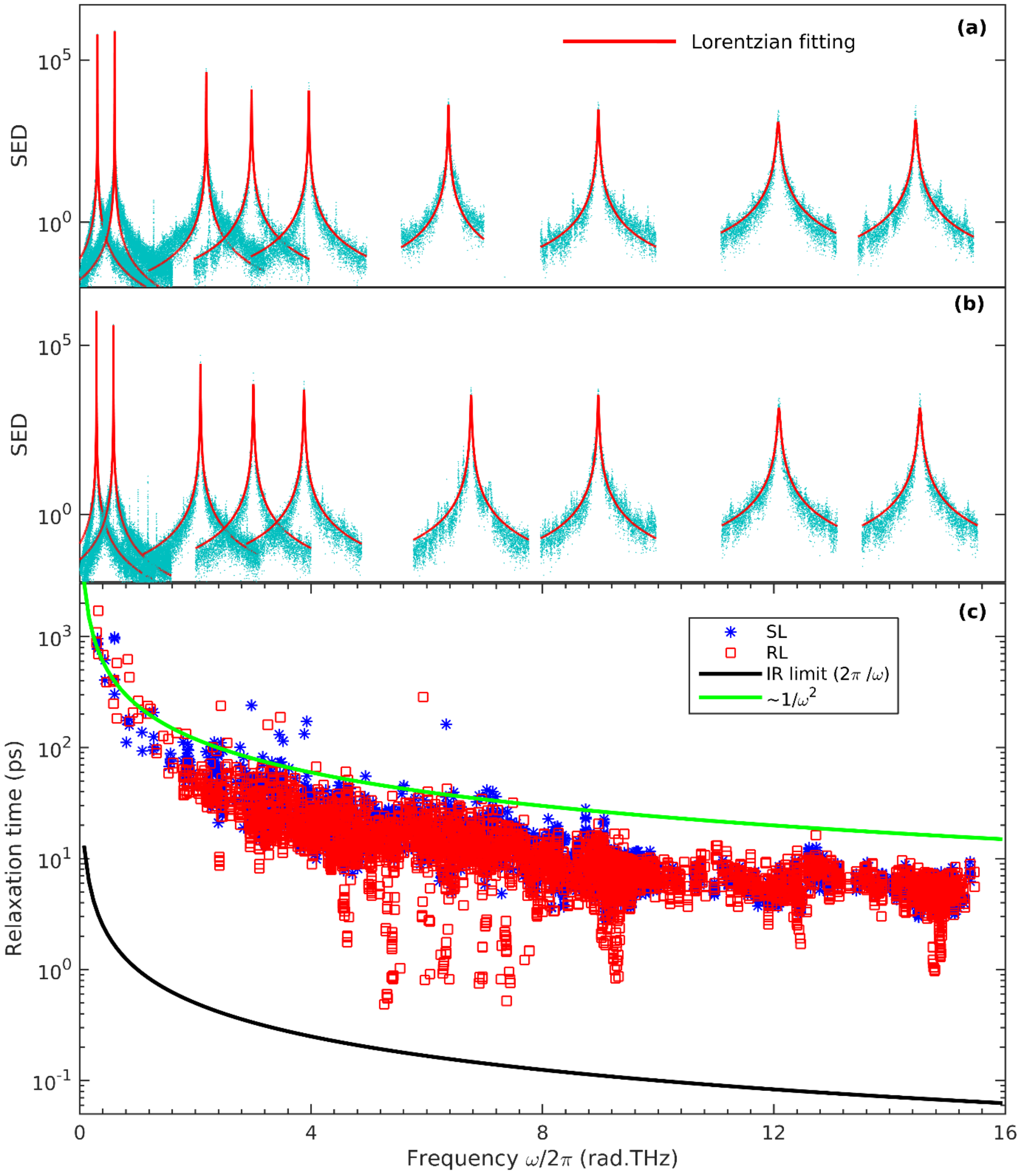

Figure 4-4: SED of selected few modes of (a) SL (b) RL structures, (c) phonon relaxation time values.

4.3.2 Effect of cross-sectional width

Figure 4-5 shows a variation of TC as a function of cross-sectional width for RLNWs and corresponding SLNWs. The non-monotonic trend of TC of SLNWs with cross-sectional widths featuring here, is attributed to the contradictory effects of long wavelength (LW) phonons and phonon-wall scattering [121]. To get more microscopic insight, the phonon density of states (DOS) of both SL and RL nanowires is evaluated via Fourier transformation of the time-velocity correlation function for different cross-sectional widths as depicted in Figure 4-6. Contrary to the quadratic trend of DOS (i.e. DOS $\propto \omega^2$) when angular frequency $\omega \rightarrow 0$ in bulk materials, nanowires' scaling behaves differently due to the quasi 1D nature of BZ [119]. However, type of phonon branch is also a factor here, where longitudinal and torsional branches follow linear dispersion which results in constant DOS when $\omega \rightarrow 0$ while quadratically dispersive flexural branches diverge in a different scaling. As expected, both RLNWs and the equivalent SLNWs exhibit almost the same DOS curve as a consequence of similar material composition and cross-sectional widths.

This result and the plot of mode relaxation times (see Figure 4-4(c)) support the claim of similar phonon properties of a given RLNW and its superlattice counterpart which was shown to be plausible for SL and RL structures (the bulk counterpart of SLNWs and RLNWs, respectively) before [49]. Wang et al. used that claim to decompose coherent and incoherent phonon fractions of TC in SLs and further concluded that only incoherent phonons transmit heat in RL structures since coherent phonons get localised with the total length. Nonetheless, it is rational to take that coherence characteristics of phonons can be directly attributed to the mean layer thickness [47]. Extending this idea to the NWs discussed here, demands an additional consideration on finite cross-sectional width of NWs which causes extra phonon-wall scatterings and originating LW phonons. These two affect the degree of phonon coherence opposite ways where phonon-wall scattering destroys the coherence while origin

Bestpfe.com

of LW phonons increases the coherence. However, at this point it is taken that those coherent characteristics of phonons in nanowires can be safely attributed to the cross-sectional width as well as mean layer thickness.

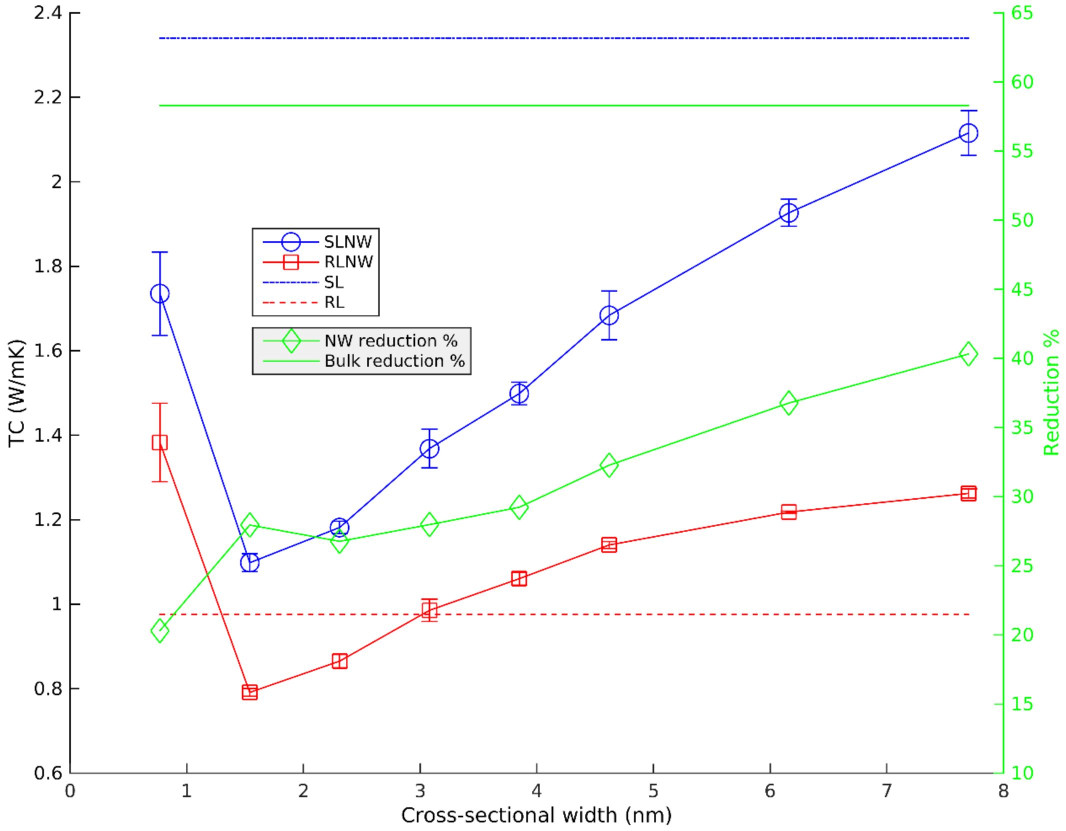

Figure 4-5: Illustration of TC of RLNWs and corresponding SLNW of different cross-sectional widths. The total length of all the nanowires in the figure is 52.1 nm.Here NW reduction % is corresponding to the reduction % of RLNWs over SLNWs while bulk reduction % is for bulk counterparts.

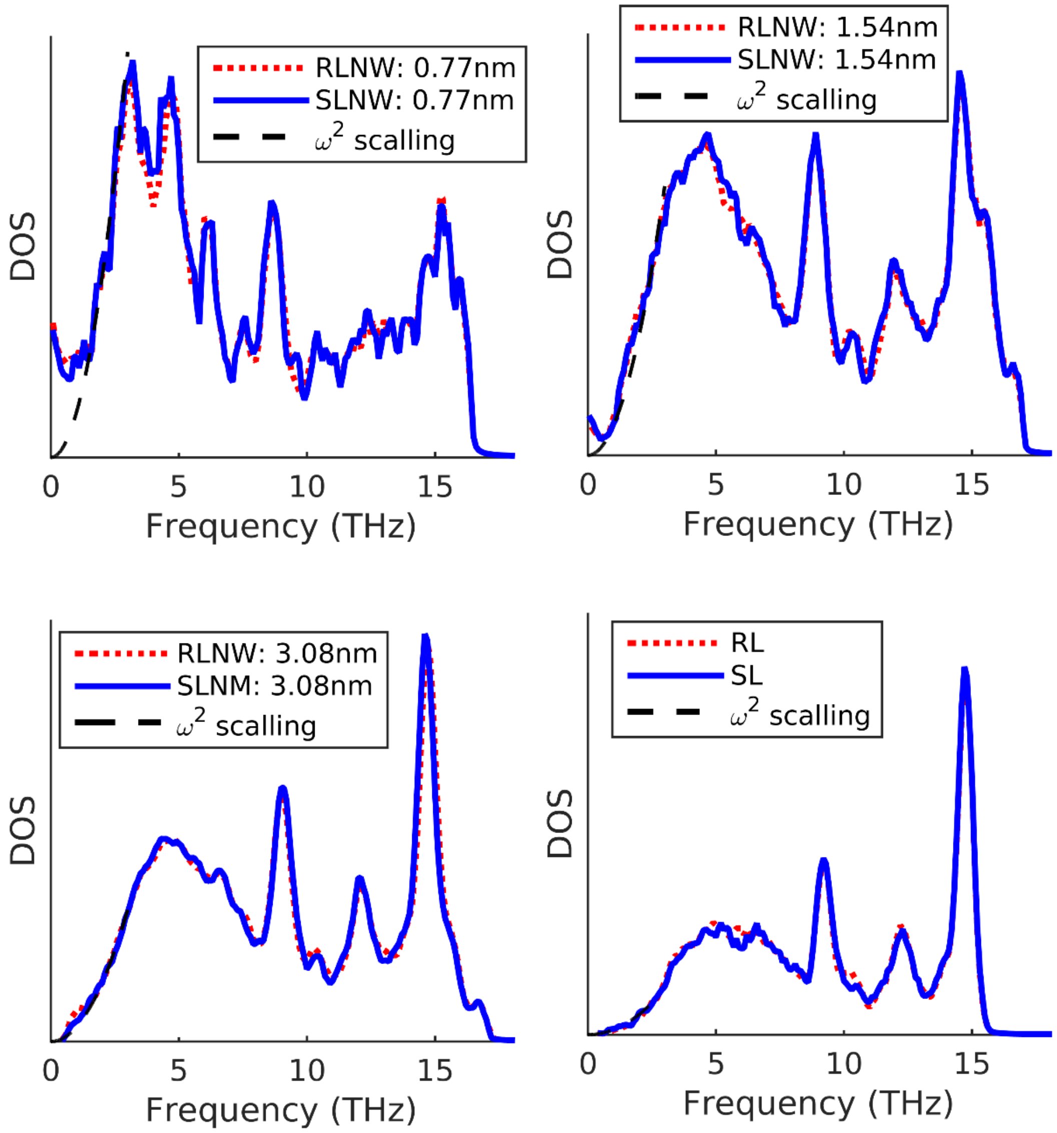

Figure 4-6: DOS against Frequency for nanowires of three different cross-sectional widths and corresponding bulk counterpart. The mean layer thickness of all the nanowires is kept as 1.08 nm

BESTPFE.COM
List of research project topics and materials

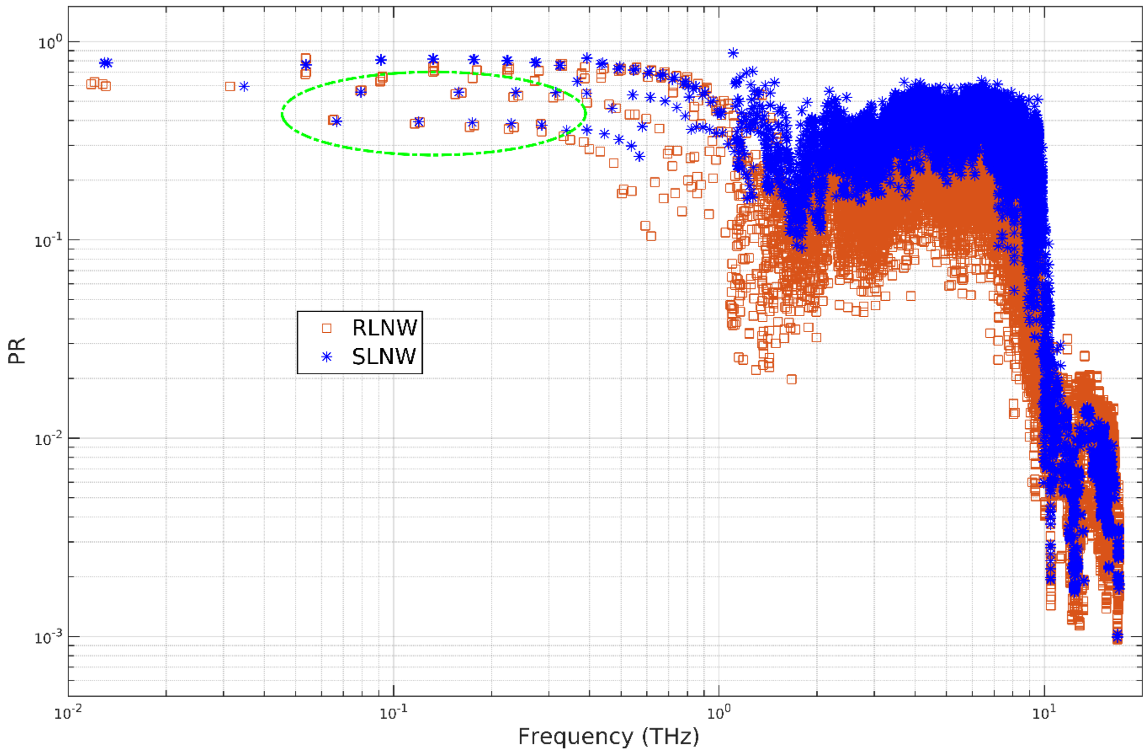

Figure 4-7: *PR* of SLNW and RLNW of mean layer thickness 1.08 nm, cross-sectional width 1.54 nm and total length 52.1 nm.

Despite the fact of originating LW phonons in RLNWs, their behaviour under the localisation inside RLNWs is not still clear. Thus, PR_n is evaluated to test the localisation of LW phonons as shown in Figure 4-7. According to the figure, the RLNW shows a distinct localisation effect compared to the SLNW, which is pronounced at the mid frequency spectrum. The *PR* at the very low frequency spectrum indicates (highlighted in the green circle in the figure) some LW phonons hardly get localised. This phenomenon is consistent with the study of Anderson localisation at 1D mass disordered harmonic crystal [164] where delocalised low frequency modes were observed at finite length. However, the existence of delocalised LW phonons in the RLNW taken here explains the non-monotonic TC trend at low cross sections shown in Figure 4-5. The TC trend of SLNWs after the minimum can be described as the dominance of phonon-wall scattering over the effect of LW phonons. This statement can be verified by observing the DOS curve of cross-sectional width 3.08 nm. The

ω^2 scaling is closely followed there similar to the bulk case indicating the weak effect of LW phonons. Phonon-wall scatterings dominate the TC of SLNWs henceforth, expected to be decreased with higher cross-sectional width. Even though RLNWs initially follow a trend similar to SLNWs, we can expect a reverse trend after some higher cross-sectional width since the TC of bulk RL is lower than the TC of RLNWs of higher cross-sectional width. However, determining this point of inflection is computationally prohibitive. To explain this behaviour, it is important to consider the effect of phonon-wall scatterings on the phonon localisation effect. The decrease in phonon-wall scatterings as cross-sectional width increases leads coherent phonons to propagate longer distances, thereby phonon localisation becomes more efficient which finally leads to a reverse trend of the TC of RLNWs. When it comes to an analysis of the difference of the TC of a RLNW and its equivalent SLNW, the assumption of similar phonon characteristics, as we tested before, is taken into consideration. This leads to the argument that the difference between the TC of RLNW and SLNW arises from how far the localisation mechanism is effective in RLNW to suppress coherent phonons. The reduction percentage is calculated as,

$$\frac{TC_{SLNW} - TC_{RLNW}}{TC_{SLNW}} \times 100.$$

Even though the reduction percentage fluctuates at low cross-sectional widths due to the competing influence of both LW phonons and phonon-wall scatterings, after some cross-sectional width (3.08 nm where DOS follows ω^2 scaling) it can be observed a gradual increment of reduction percentage as phonon-wall scatterings are declining.

4.3.3 Effect of mean layer thickness

In order to investigate how mean layer thickness affects the TC, it is evaluated for both RLNWs and equivalent SLNWs by varying mean layer thickness while keeping the total length of 100 nm as shown in Figure 4-8. Wang et al. [61] investigated a similar case using fictitious LJ material and the results from the present study closely follow the implication derived there qualitatively. The reason for the non-monotonic trend of the TC of SL structures was established elsewhere [47], [54] as the change of dominance of coherent phonons to incoherent phonons.The fact of declining coherent phonon dominance as layer thickness increases, yields a monotonic TC trend for RLNWs. Here, the TCs of RLNWs of two extreme uniform distributions are illustrated in the Figure 4-8. However, the selected two different distributions show no significant difference. The lower (type2) and upper (type1) variances were determined based on the prescribed mean layer thickness (see Appendix D). As can be seen, the reduction percentage is gradually decreasing from 42 to 4% with the increasing mean layer thickness from 1.08 to 3.8 nm. It is interesting to see that that RLNW of the lowest mean layer thickness can attain a lower TC than that of corresponding random alloy nanowire.

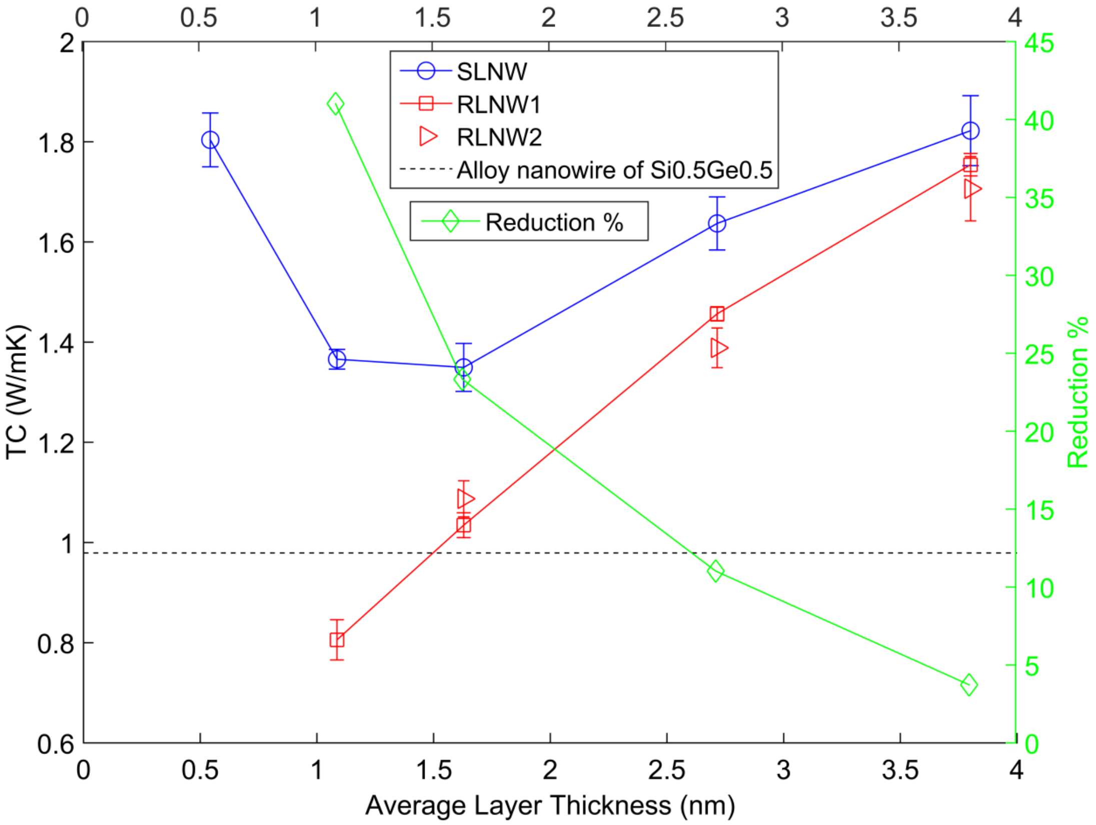

Figure 4-8:Comparison of TC between RLNWs and corresponding SLNWs of different mean layer thicknesses.

4.3.4 Effect of temperature and total length

As shown in Figure 4-9(a), temperature (T) affects the TC of RLNWs and SLNWs in different ways. Temperature causes the reduction of SLNW's TC as the lifetime of phonons decreases following 1/T trend with the enhancement of phonon-phonon umklapp scattering[86]. It is established that increased temperature reduces the phonon coherence length dramatically for opticals[47], thus, a fraction of coherent phonons turns into incoherent. If the same case is viewed using the concept of coherence, it can be argued that faster heat carriers which pass several interfaces freely (coherent phonons) convert to disrupted heat carriers which disperse at interfaces (incoherent phonons). Contrary to that, the role of coherent phonons is different in RLNWs where localisation (see Figure 4-3 andFigure 4-7) makes them extremely inefficient heat carriers. The deterioration of coherent properties of phonons with increasing temperature weakens the localisation mechanism, thereby causing an increase in the TC. However the fraction of incoherent phonons of RLNW follows the 1/T trend leading to a decrease in the TC of RLNWs. These two competing effects lead to a weak increment of the TC of RLNW as shown in Figure 4-9(a). Furthermore, keeping the claim of similar phonon characteristics of both structures, it can be argued that the TC due to incoherent phonons is identical for both structures at a given temperature while the coherent phonons' contribution is lower in the RLNW. Along with this line of argument, we expect to have lower coherent phonon TC contribution with increasing temperature and therefore the difference of TC of both structures must be reducing, which is further verified by the reduction percentage in Figure 4-9(a). The reduction percentage reduces from 56 to 27% as temperature varies from 100 to 600 K.

The effect of nanowire's total length for SLNW and RLNW is presented in Figure 4-9(b). The increasing trend of SLNW's TC was shown before [87] and explained as the emergence of more low frequency phonons with total length. Even though this reason is applicable for

RLNWs, those rate of increment is low as more effective localisation is taking place with the total length (see Figure 4-3(b)). The increasing trend of reduction percentage as total length increases, further verifies that reasoning.

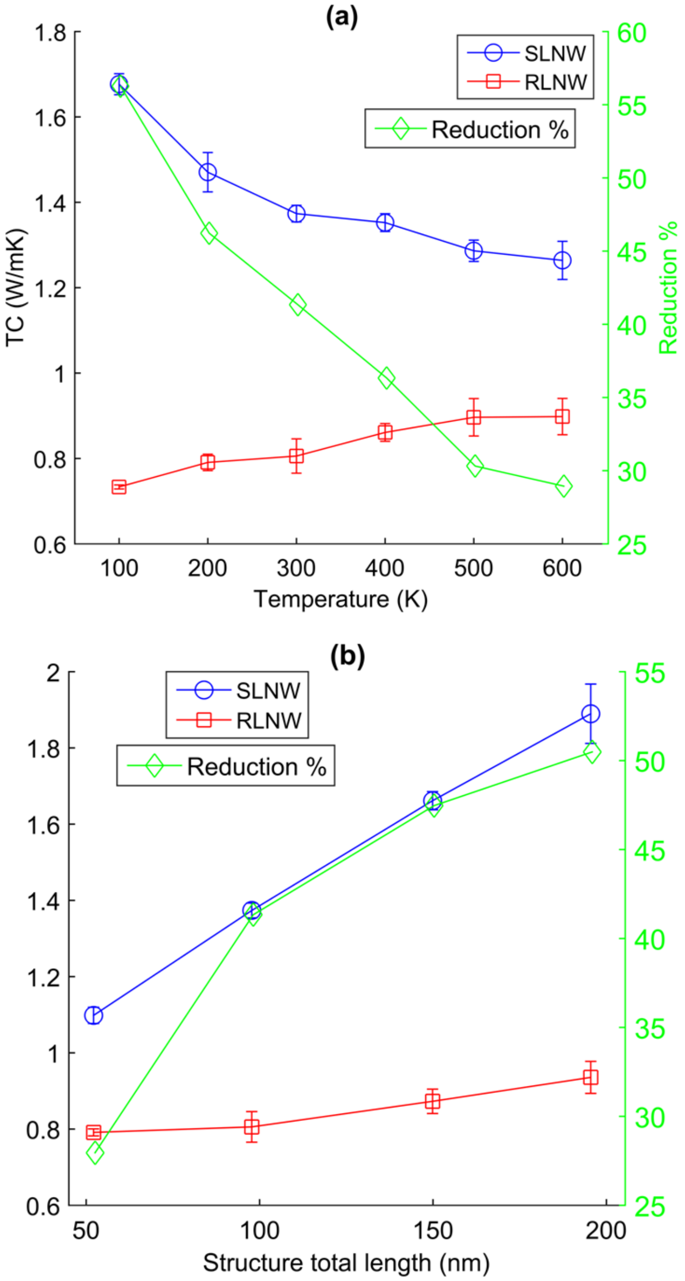

Figure 4-9: (a)TC variation of SLNWs and RLNWs with temperature. The total length and cross-sectional width of NWs are kept at 100 nm and 1.54 nm, respectively. (b) TC variation with respect to nanowire total length. The mean layer thickness and cross-sectional width are kept at 1.08 nm and 1.54 nm, respectively.

4.3.5 Effect of shell modifications

Finally, two kinds of shell modifications to the nanowires are tested and their effects on the TC are evaluated. First, nanowire configurations are created by randomly changing the type of atoms (Si or Ge) of the shell region called mixing in different percentages ranging from 0 to 50%. Therefore, these defects enhance more phonon-defect scatterings which lead to a drastic reduction of SLNW's TC even for 5% (see Figure 4-10(a)). Afterwards, SLNW's TC remains constant up to the complete shell atom mixing case (50%). On the other hand, the TC of RLNWs remains unchanged up to 10% exhibiting weak influence on the localisation process. However, at higher atomic mixing (50%) the TC of RLNW attains the value of the corresponding SLNW due to the disruption of coherence of phonons which was demonstrated in other studies [47], [165]. Moreover, surface roughening is tested by removing shell atoms for a range of percentages up to 3% as illustrated in Figure 4-10(b). As expected the TC of the SLNW gradually decreases as the atom removing percentage is increased due to enhanced phonon-surface scattering. However, lower atom removal percentages do not affect the TC of RLNW but eventually approach the same value of SLNW due to the same reason mentioned for the above case. Furthermore, the reduction percentage is reducing in both cases as shell atomic disorder increases owing to the fact of breaking coherence, thereby, weakening the localisation in RLNWs.

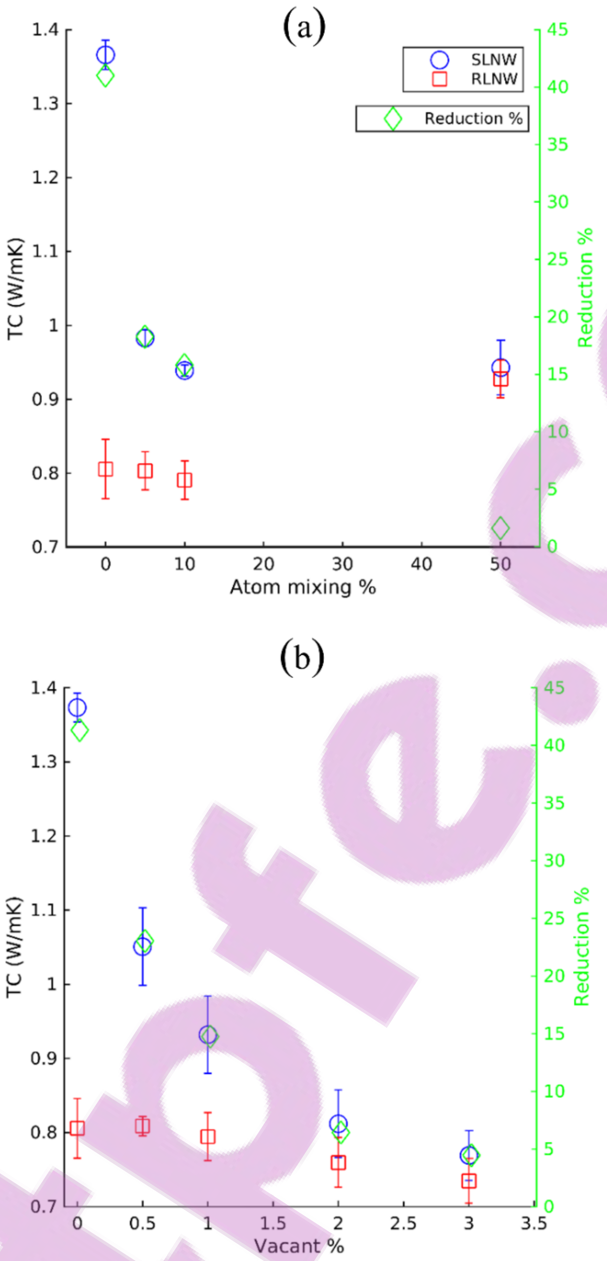

Figure 4-10: TC of nanowires with (a) random shell atom mixing and (b) random shell atom removal. Total length, cross-sectional width and mean layer thickness are kept as 100 nm, 1.54 nm and 1.08 nm, respectively.

Bestfe.com

Chapter 5

Thermal Performance of Nanotwinned Random Layer Structures

5.1 Introduction

The nanostructuration of Si is considered as an effective way of improving the thermoelectric figure of merit over bulk Si essentially due to the yield of significantly low thermal conductivities [166]. Therefore, large varieties of Si based nanostructures such as nanowires [7], [8], superlattices [167], nanomeshes [168], [169], alloy [170], [171] and nanograin polycrystalline [88], [172] structures etc. have been proposed and investigated experimentally and theoretically. The low thermal conductivity (TC) of Si polycrystalline materials was attributed to the presence of a large number of phonon-grain boundary scatterings [172]. Recently, a few studies [65]–[67], [173] attempted to introduce a new kind of nanostructuring utilizing the twin boundary orientation of Si. A twin boundary is a special form of grain boundary where one side of the crystal is a mirror image of the other [174]. Lower excess energy is possessed for twin boundary formation compared to other grain boundaries [175], and therefore the formation of twin boundaries is frequent. Moreover, nanotwinning (creating twin boundaries in nanoscale) was shown as an effective mechanism

BESTPFE.COM
List of research project topics and materials

for improving the physical and mechanical properties of materials such as hardness, thermal stability and fracture toughness [176]–[178].

The atomistic study by Porter et al. [65] on Si nanotwinned superlattices (NTSL) in bulk and nanowire forms demonstrated crossover of phonon transport from diffuse interface scatterings (incoherent) to superlattice-like (coherent) behaviour yielding a minimum TC. In their study, intrinsic interface scattering was identified when the twin period was higher than 22.6 nm, having a constant value to interface conductance (6.8 GW/m^{2}K) for two different temperatures irrespective to the heat flux. However, the Kapitza thermal boundary resistance was seen to be decreasing with decreasing twin period after 22.6 nm indicating the existence of coherent phonons. Comparisons of TC of Si/Ge hetero-twinned SLs and conventional Si/Ge SLs were performed by Dong et al. [67]. Both structures have almost similar thermal conductivities over the twin period. However, further investigations suggested that two different mechanisms affect the lower thermal conductivities of both structures where Si/Ge hetero-twinned SLs had lower group velocities and higher relaxation times compared to conventional SLs.

The motivation of this study is the realisation of coherent phonons (superlattice phonons) in NTSL structures [65], [67], which may be subject to localisation for the structures with random arrangement of twin boundaries due to the Anderson localisation [164]. The coherent phonon localisation effect has been demonstrated for Si/heavy-Si [179], Si/Ge structures [159] and Lennard-Jones fictitious materials [49], [61] before. In this study we introduce nanotwinned random layer (NTRL) structures in which twin boundaries are randomly distributed, and compare their performance with the corresponding NTSL structures where twin boundaries are regularly distributed (see Figure 5-1). Moreover, the comparison is extended towards the Si/Ge hetero-structures and examines the techniques for getting ultra-low thermal conductivities utilizing random arrangements of both twin boundaries and Si/Ge interfaces.

5.2 Computational Procedure

As illustrated in Figure 5-1, the atoms in the structures are populated in a diamond lattice structure of lattice length 0.543 nm keeping crystal orientations along <1 1 1>, <1 0 $\bar{1}$>, <1 $\bar{2}$ 1> and <1 1 1>, <1 0 $\bar{1}$>, <$\bar{1}$ 2 $\bar{1}$>. Even though different random twin boundary distributions can be suggested here, a uniform random distribution is taken for this investigation. The criterion of comparing the TC of RLs and SLs is based on the mean-layer thickness [49], therefore, a NTRL with particular mean-layer thickness is generated by the random placement of twin boundaries following uniform random distribution in which the mean is equal to the expected mean layer thickness of the structure.

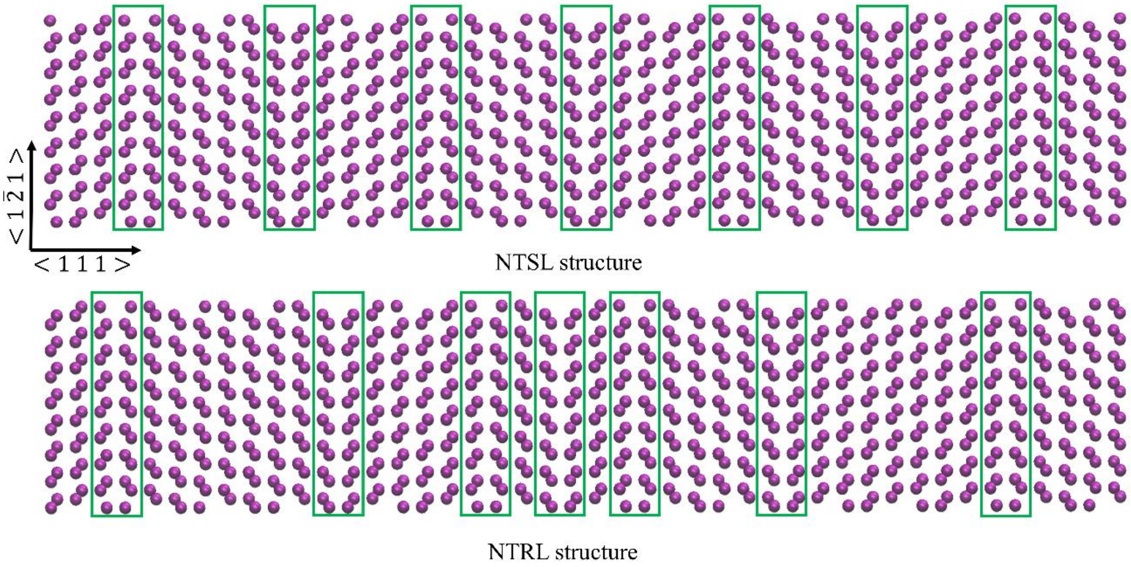

Figure 5-1: Atomic configurations of NTSL (top) and NTRL structures (bottom). Twin boundaries are highlighted in boxes.

The NEMD simulations are conducted to evaluate the TC of the structures using an efficient MD solver, LAMMPS [161]. Furthermore, atomic interactions are modelled by Tersoff potential with the original parameter optimized for Si-Ge systems [85]. The time step is kept at 1 fs. The NEMD procedure of this study is basically similar to the method followed in Chapter 4 and is, briefly, as follows.

The structure is sandwiched by a heat source and heat sink each 18.81 nm thick. Two additional regions each 2.82nm long are added to the two extremes of the structure. Periodic boundary conditions are prescribed along all three directions. Initially, the entire structure is relaxed corresponding to the zero pressure at the NPT ensemble for 500 ps. Subsequently, two extreme regions are fixed while the rest of the structure is further relaxed for 100 ps each in the NVT and NVE ensembles respectively. Once the structure is fully relaxed following the above procedure, the HEX algorithm [162] is implemented by adding heat flux to the source while removing the same amount from the sink. Simulations take 1-15 ns to achieve steady state depending on the size and type of the structure and simulations are continued for an additional 5 ns to evaluate the steady state temperature field along the longitudinal direction <1 1 1>. The reason stated in section 4.2.2 dividing temperature difference by the length of the nanowire accurately captures the interface effects. Therefore, the latter procedure to evaluate temperature gradient is followed in the present study.

5.3 Results and Discussion

5.3.1 Evaluation the TC of NTRL structures

As shown in Figure 5-2, the TC of NTSL and NTRL of different mean-layer thickness are compared for the structure lengths of 90 and 170 nm. The variance of the uniform random distributions is kept at 0.5897 nm^2. It is interesting to see that NTRL structures yield a clear reduction of TC over their superlattice counterparts which is pronounced at low mean-layer thicknesses. Contrary to the non-monotonic trend exhibited by the NTSL structures [65], NTRL structures produce a monotonic trend indicating the effectiveness of phonon localisation procedure for low mean-layer thicknesses. Similar illustrations were shown before for Si/Ge hetero-structures [159] and fictitious LJ materials [49], [61]. However, those studies utilized the mass dissimilarity at interfaces to achieve a lower TC while this work employs the crystalline orientation dissimilarity. To quantify the difference of TC of NTRL and corresponding NTSL structures, the reduction percentage is defined as,

$$\frac{TC_{NTSL} - TC_{NTRL}}{TC_{NTSL}} \times 100.$$

The NLRL of mean-layer thickness 1.88 nm attains reduction percentages of ~23 and ~27% over corresponding NTSL for the structure sizes 90 and 170 nm, respectively. This reduction is as high as ~55 and ~53% for corresponding twin-free Si counterparts. The higher reduction percentage of NTRL with lower mean-layer thickness is attributed to the higher fraction of coherent phonons [47], since the localisation effect, one of the wave phenomena, is effective with coherent phonons [49]. The NTRL's results in Figure 5-2(a) are compared with a different random layer distribution proposed by Wang et al. [49], [61] (see Appendix E). The results of both distributions closely follow each other.

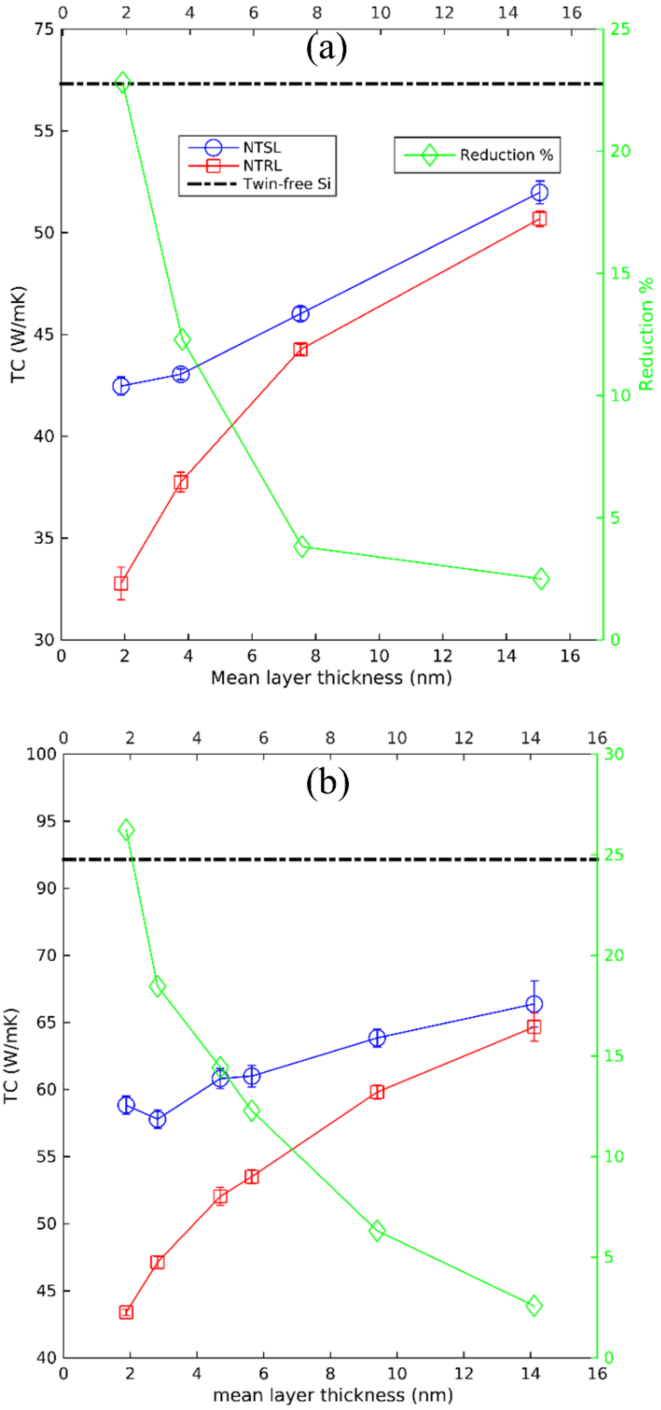

Figure 5-2: Illustration of TC of NTSL and NTRL structures of length (a) 90 nm (b) 170 nm.

The Participation Ratio (PR_n) is evaluated for similar structures mentioned above as illustrated in Figure 5-3. A distinct localisation effect of modes can be seen particularly at the mid frequency spectrum of the NTRL over the NTSL structure indicating the possible cause of lower TC of NTRL structures. The *PR* at the very low frequency spectrum indicates phonons hardly get localised. This phenomenon is consistent with the study of Anderson localisation at a 1D mass disordered harmonic crystal [164] where delocalised low frequency modes were observed at finite length.

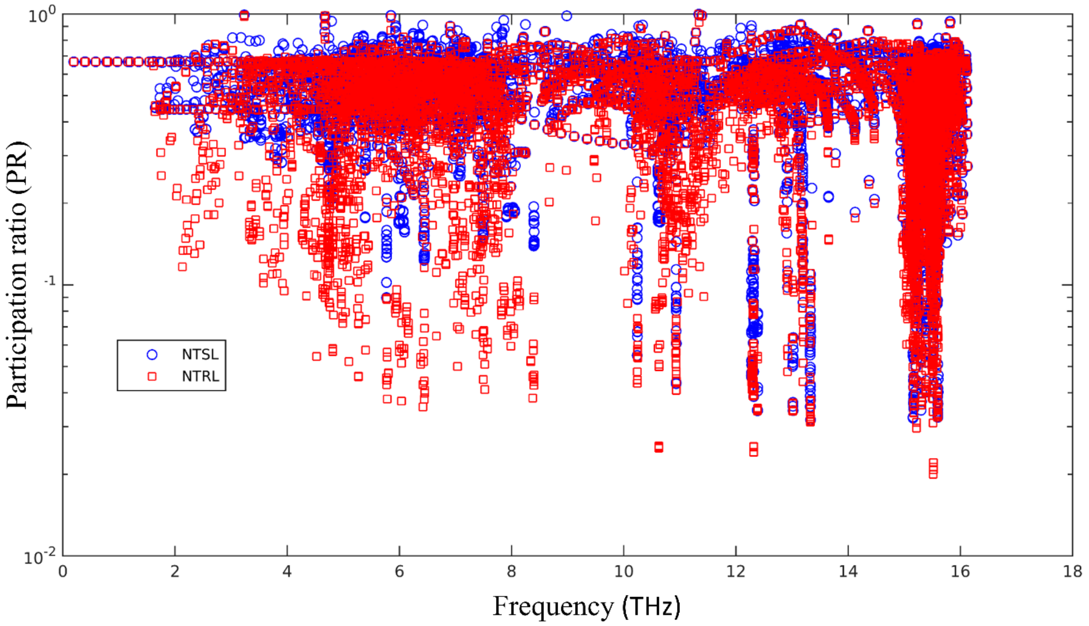

Figure 5-3:*PR* of NTSL and NTSL of total length 22.5 nm.

5.3.2 Effect of temperature for TC of NTRL structures

Figure 5-4 demonstrates the TC of NTSL and NTRL structures of mean layer thickness 1.88 nm at different temperatures varied from 300 to 700 K. The TC reduction of NTSL can be explained as a result of increasing umklapp scatterings which causes a decrease in the phonon life time in 1/T scaling [86]. To figure out the TC reduction of NTRL, further explanation is required for the phonon localisation process as temperature is varied. It is established that increments of temperature destroy the fraction of coherent phonons [47] leading to an increase in the incoherent phonon fraction which is not subject to localisation effect anymore. Even though the fraction which turns from coherent to incoherent with the temperature increment causes higher TC, the existing incoherent phonons seem to overshadow the trend finally leading to a decreasing pattern. Along with this line of argument, we expect to have a lower coherent phonon TC contribution with increasing temperature and therefore the difference in TC of both structures must be reducing, which is further verified by the reduction percentage in Figure 5-4. The reduction changes from ~26 to 17% as temperature varies from 300 to 700 K.

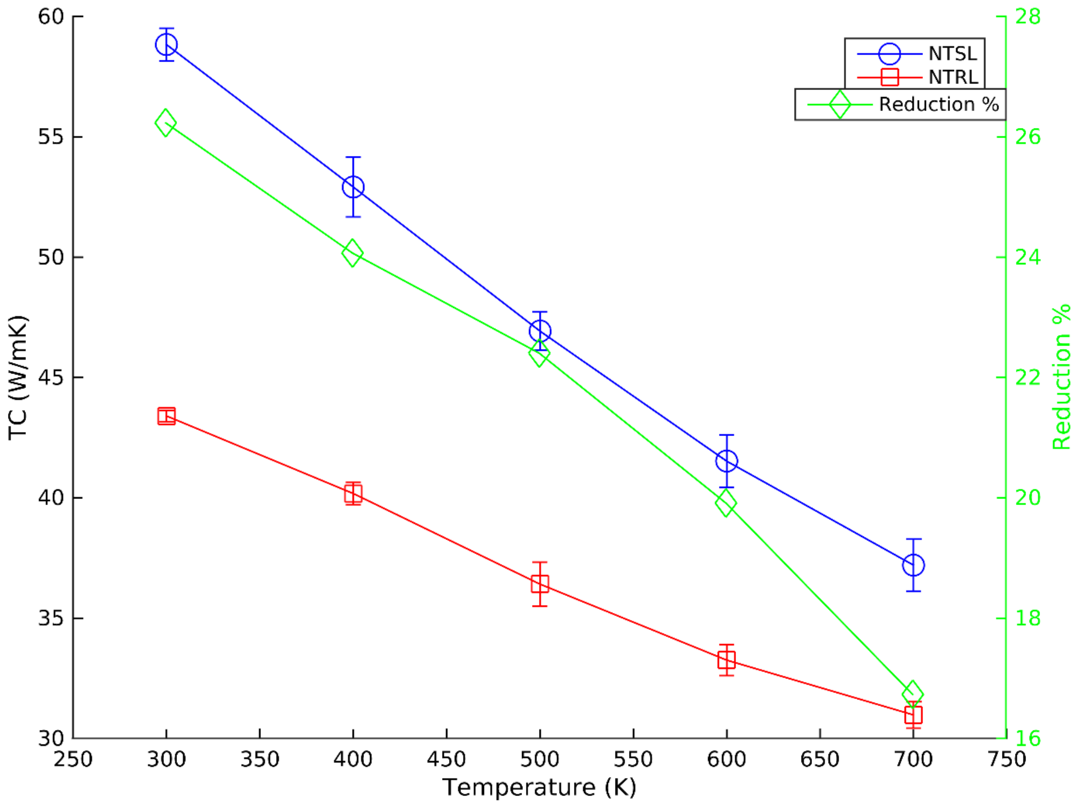

Figure 5-4: Effect of temperature on TC of NTSL and NTRL structures.

5.3.3 Ultra-low TC of mix hetero-nanotwinned random layer structures

We systematically apply and investigate the effect of twin boundary on the TC of Si/Ge hetero random layer structures. Thus, in the present case, three different structures are suggested: (i) Si/Ge conventional hetero-random layer (c-HRL) structures (ii) hetero-nanotwinned random layer (HNTRL) structures where twin boundaries coincide with Si/Ge material interfaces and (iii) mix-HNTRL structures in which twin boundary placement and the Si/Ge interface placement are arbitrary as shown in Figure 5-5.

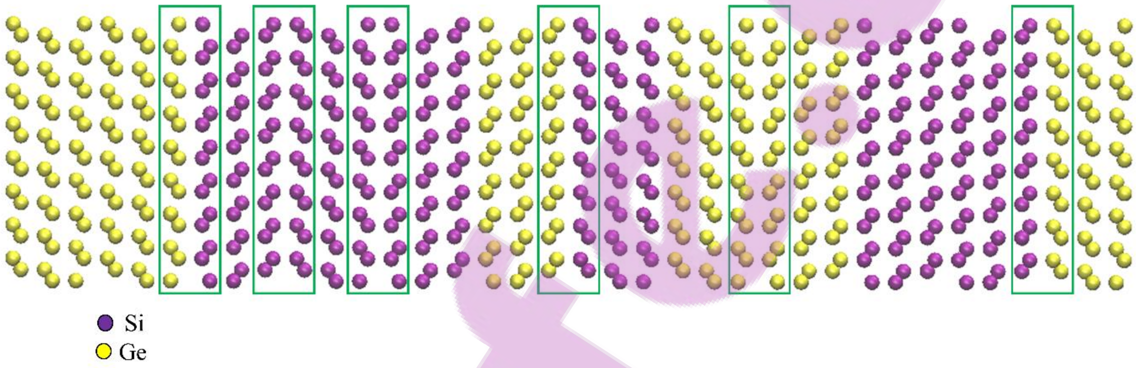

Figure 5-5:Atomic configuration of a mix-HNTRL structure in which mean layer thicknesses from both twin and material random distributions are kept at 1.88 nm. Twin boundaries are highlighted in boxes.

Figure 5-6 illustrates the TC of c-HRL, HNTRL and mix-HNTRL structures in which the mean-layer thickness of Si/Ge interface distribution varies from 1.25 to 7.52 nm while the mean of twin boundary distribution varies from 1.88 to 7.52 nm. In both distributions, the variance is kept at 0.5897 nm^2. As illustrated in Figure 5-6, the impact of Si/Ge random interface distribution is critical for reducing TC. However, random twin boundary distributions also contribute towards further reduction of TC. This fact is clear by observing the reduction percentage which stays between 20-30% as shown in Figure 5-6. It is important to note that the reduction correlates with the structure’s lower mean-layer values in both twin

Bestpfe.com

boundary and Si/Ge interface distributions. Furthermore, we compare the TC results with the corresponding amorphous-Si (a-Si) structure in which atomic coordinates are generated following the melt-quench procedure [180]. Via the NEMD method, the TC is evaluated for the corresponding a-Si (total length of 90 nm) structure as 1.68 ± 0.04 W/mK which is comparable with the TC obtained by He et al. [180] in which TC is reported for a structure of a-Si of total length 98 nm as 1.73 W/mK verifying the procedure followed here. It is interesting to report that the reduction of ~31% is attained over a corresponding a-Si structure by mix-HNTRL in which mean-layer thickness of twin boundary and Si/Ge interface distributions are 1.88 and 1.25 nm, respectively. Moreover, this same HNTRL structure attains up to ~98% reduction compared to the twin-free Si counterpart. These results thus provide strong indications of the effectiveness of mix-HNTRL as thermoelectric materials.

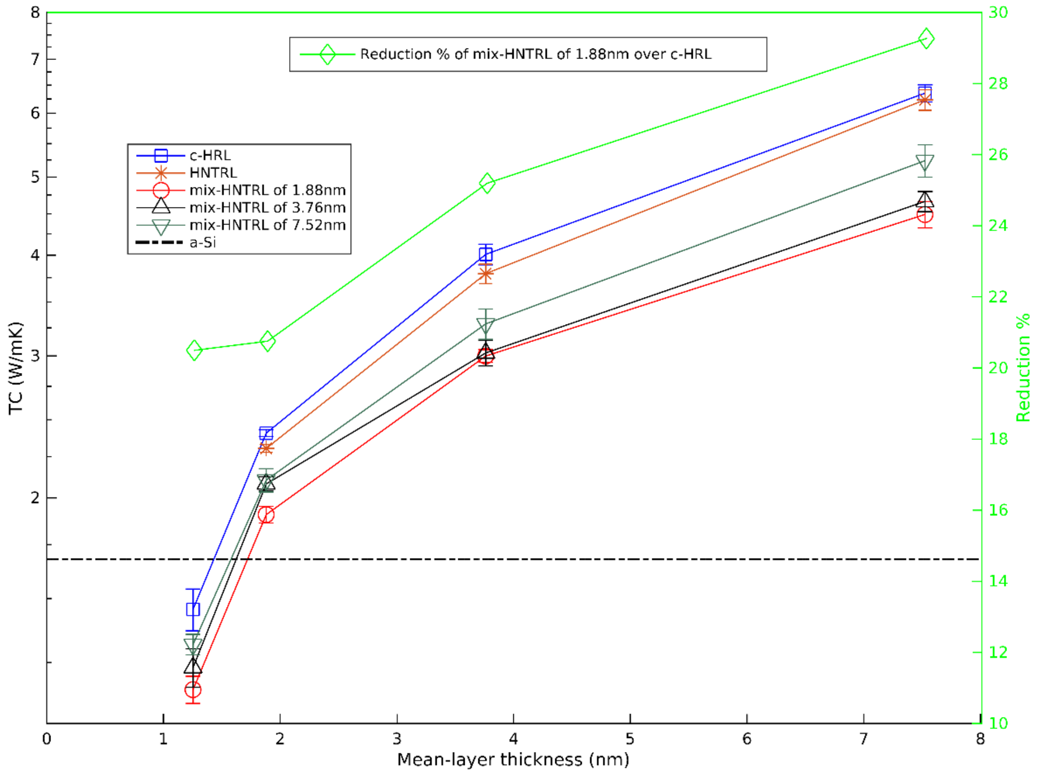

Figure 5-6: TC of c-HRL, HNTRL and mix-HNTRL structures of total length 90 nm for different random twin boundary and Si/Ge random distributions.

CHAPTER 6

Conclusions, Limitations and Future Work

6.1 Conclusions

The aim of this work was to investigate the phonon or vibrational-mode driven TC of nanostructures. The nanostructures discussed in this study included nanowires, hetero-structures and combinations of them constructed using LJ materials and Si/Ge. These structures are considered as potential efficient thermoelectric materials.

In Chapter 3, we investigated the TC of nanowires governed by vibrational modes using an NMD method based on BTE-SMRTA. The EMD-GK method was employed as an alternative approach to verify the NMD procedure. A multi-step approach and separate branch analysis were used for the NMD implementation which significantly reduced the computational requirements. The convergence issue of TC in nanowires as the structure total length increases was looked at in detail.

As can be seen from Figure 3-4 in Chapter 3, each acoustic branch follows different trends as frequency tends to zero. However, all show signs of approaching a constant value. This trend is clearly visible for AF branches since those are extended towards ultra-low

BESTPFE.COM
List of research project topics and materials

frequencies due to the quadratic nature of the branch. Moreover, phonon relaxation times of each acoustic branch were fitted to the form proposed by Mingo et al. [119]. The fitted function represented the corresponding data points well indicating the sign of second-order 3-phonon scatterings at low frequencies which finally led to converged TC values. The close agreement of the results of the NMD and EMD-GK methods suggested a few interesting observations.Firstly, it verified the NMD procedure implemented in the study. More importantly, phonon hydrodynamic behaviour for Si nanowires [102] and single-wall carbon nanotubes [181] shown before was not visible for the structure with geometrical and physical conditions taken here since NMD (applicability of SMRTA) was capable of accurately evaluating the TC.

It was concluded that higher DOS resulted in narrower nanowires to exhibit non-monotonic behaviour of TC. Even though phonon group velocities and relaxation time values decreased with cross-sectional width, the TC trend was reversed by the higher DOS of the nanowires of ultra-low cross section. It was shown that the behaviour of acoustic modes, especially AT branch, are responsible for that.

The Eigenvector correlation-based technique developed in this study (Appendix C) showed that mid and high frequency modes deviate from the propagating behaviour due to shell alloying. The TC contribution given by low frequency propagating modes was evaluated by the VC-NMD method while the effect of diffusions/locons was calculated by A-F theory. Several implications were made on the shell alloy nanowires (SANWs) in this study. The reduced TC of SANWs, as the mass of alloy species is increased, emerges due to several factors. The fact of converting propagons to non-propagons is partially responsible for the reduced TC of SANWs. Furthermore, as illustrated, the cutoff frequency shifted towards lower values as the mass of alloy species was increased. The behaviour of low frequency modes (modes before the ω_{cut}) is similar to the corresponding modal behaviour of

PNWs. The combined effects of lower cutoff frequency and higher group velocity are, on the other hand, responsible for the reduced TC of SANWs as the mass of alloy species is increased.

In Chapter 4, the NMD results together with PR analysis indicated that the modes in RL structures show characteristics similar to those of superlattice counterparts except the higher degree of mode localisation of RL structures which leads to the lower TC. The NEMD simulations were conducted to investigate the improvement of thermal insulation properties of random layer nanowires (RLNWs) over equivalent superlattice counterparts at different geometrical parameters such as cross-sectional width, mean layer thickness, total length and physical parameters such as temperature. An anomalous pattern with two inflection points (minimum and maximum) of RLNW's TC against cross-sectional width was identified contrary to the pattern of superlattice nanowires (SLNWs) with one inflection point (minimum). The possible cause for the maximum could be due to the competing effect of phonon-wall scatterings and the phonon localisation process. The simulation results verified that the reduction percentage is strongly correlated with the fraction of coherent phonons and how effectively they get localised. The lower mean layer thickness, lower temperature and longer total lengths cause a higher fraction of coherent phonons and efficient localisation, which result in a higher reduction percentage. These considerations would help to realize RLNWs from fabrication and application perspectives in the future.

As shown in Chapter 5, we tested the effect of random placement of twin boundaries in nanoscale on the TC of Si and Si/Ge structures via NEMD simulations. The results show that significant improvement of thermal insulation properties can be attained following nanotwinning in both Si and Si/Ge structures. The mix-HNTRL structures introduced here achieved ~31 and ~98% of TC reduction over corresponding a-Si and twin-free Si structures indicating the effectiveness of mixing both twin boundary and Si/Ge interface distributions randomly. These structures may be important for developing efficient thermoelectric materials in the future not only due to the significant enhancement of thermal insulating properties while preserving the crystalline atomic structure, but also to other desirable characteristics such as improved hardness and thermal stability.

6.2 Limitations

In this section, limitations of the current workare discussed. These are primarily due to structural sizes and the implemented computational methods.

The number of atoms (P) of a nanostructure and the type of material constituents were determined considering the available computer resources. In doing so, scaling of CPU and memory with number of atoms for each computational method was taken into account. As given by Larkin (2013) [182], both CPU time and memory in MD simulations (which include GK and NEMD) scales as P^1 while NMD method scales as P^2. Furthermore, in A-F theory, CPU time scales as P^3 and memory scales as P^2. Taking these factors into consideration and with the multi-step NMD implementations, we managed to investigate the atomic structures up to ~28,000 which is approximately four times larger than the structures addressed in Larkin (2013) [182]. Moreover, the maximum number of atoms in the NEMD simulations were taken up to ~200,000. The statistics of the number of simulations against the number of atoms in the NMD simulations (Chapter 3) and the NEMD simulations (Chapters 4 and 5) are given in Appendix F.

The inherent drawback of the NMD method is taking all kinds of phonon-phonon scattering (including normal process) as momentum destroying and heat dissipative due to the single mode relaxation time approximation (SMRTA). Even though the results derived by the NMD method closely agreed with those from the GK method for the nanowires of the LJ parameters used here, such agreement may not attain for the LJ nanowires of higher energy depth. Moreover NMD implementation does not provide more insight into the difference of the scattering rates of the normal process, umklapp process, phonon-defect and phonon-surface scatterings which is required for more rigorous investigation.

The MD simulations implemented in this work are classical, therefore applicable only in the high temperature limit. The application of this method in situations where quantum effects are dominant is questionable. Operating temperatures of the structures were carefully selected as these are not well below the Debye temperature.Therefore in case of analysing nanostructures at well below the Debye temperature, the implementation procedure of this work is not appropriate.

6.3 Future Work

1. In this study, the NMD analysis on nanowires was limited to investigating PNWs, SLNWs and SANWs. This analysis can be extended further for various other nanowire configurations such as core/shell and surface modulated nanowires etc. which would reveal the interesting modal behaviourssuch nanowires demonstrate.
2. The close agreement of TC calculated by the NMD and GK methods of LJ nanowires suggest that LJ nanowires do not illustrate the phonon hydrodynamic flow demonstrated for Si nanowires. This reason could be the dominance of umklapp phonon scatterings over normal scatterings of LJ nanowires. It may be important to investigate the phonon hydrodynamic flow of nanowires made of soft materials such as PbTe, PbS and GeTe to gain a comprehensive understanding of the phonon behaviour of ultra-thin nanowires.
3. An extension of the procedure developed for the SANW based on VC-NMD and A-F

methods to the rough and amorphous nanowire is important to check. The ability to apply VC approximation to the rough nanowires, in which some of the shell atoms are displaced or amorphous nanowires where atomic structure deviate from crystalline form, would be challenging tasks since lattice disorder is also involved with those. In that case, a proper way of defining corresponding VC structure which satisfied both density and elastic constants of the original structure, must be investigated.

4. Even though the Si/Ge RLNWs, Si NTRLs and Si/Ge NTRLs demonstrate low phonon governed TC, it is vital to investigate those effects on the Seebeck coefficient and electrical conductivity to make sure of the improved thermoelectric performance. Further, it is important to establish the optimum parameters such as layer thickness, cross sectional widths etc. which gain the maximum figure of merit.
5. Conducting comprehensive mode level analysis for RL or RLNW structures has significant importance since the behaviour of modes of those are not fully revealed. This would shed more insight on the performance of RL structures as geometrical and physical parameters are varied. For instance, as far as temperature is concerned, it affects on degree of coherence of modes and the degree of mode localisation, and thereby, the TC of the structure are noteworthy to investigate to reveal phonon behaviour of nanostructures in general.

Appendix A: Convergence Issue of 1D Structures

The TC of a system of volume V is given by

$$K = \frac{1}{V k_b T^2} \sum_{k,v} C_{ph}(k,v) \mathbf{v}_g{}^2(k,v) \tau(k,v)$$

When the system is large, therefore, BZ is dense, and the summation can be replaced by the integration and with the Debye approximation the above equation can be arranged as

$$K = \frac{k_b}{V} \int_0^{\omega_c} \mathbf{v}_g{}^2 \tau(\omega) DOS(\omega)\, d\omega$$

where ω_c is the cutoff frequency. In bulk materials, the TC is bounded since ω^2 scaling of DOS [183] is cancelled out by the first-order 3-phonon scattering rate $\tau \sim 1/\omega^2$. However, DOS of a 1D structure is finite at low frequencies as below [183]

$$DOS(\omega) = \frac{L}{2\pi \mathrm{v}_g}$$

which leads to divergence of TC as shown below.

$$K \sim \int_{2\pi \mathrm{v}_g/L}^{\omega_c} \frac{1}{\omega^2} d\omega \sim L$$

where TC is diverging with the length for linear dispersion branches. The lower argument of the integrand which denotes the lowest mode frequency comes from the linearly dispersive assumption. The equation above demonstrates the divergent trend of TC for the combined effects of 1D BZ and first order 3-phonon scatterings.

Appendix B: Identification of Acoustic Branches

Eigenvector representation of the nanowire configuration shown in Figure 3-1 for three different acoustic branches at $\omega = 0.3448\ \text{rad. THz}$.

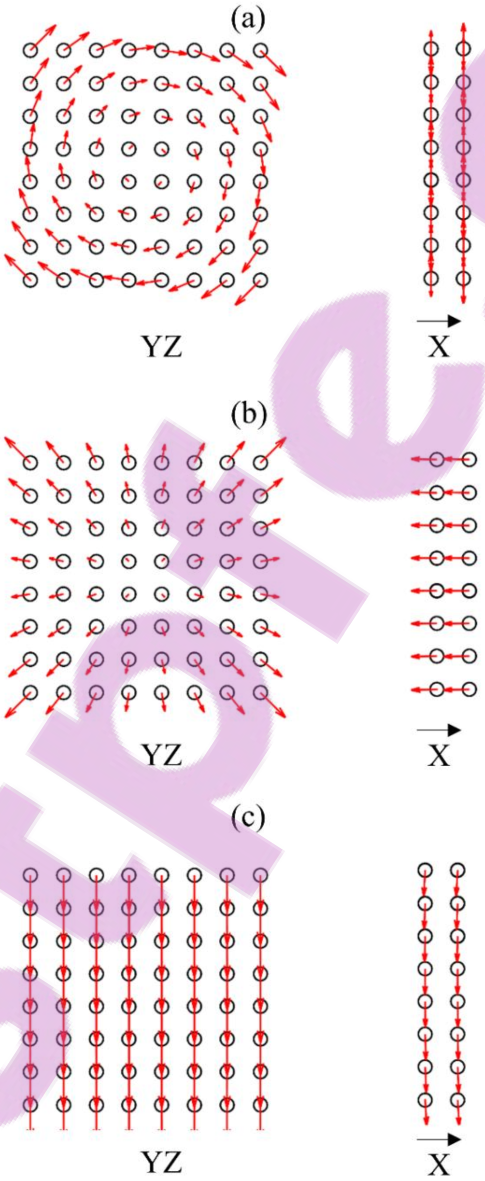

Figure B-1:Vector plot of eigenvectors of (a)AT (b)AL and (c)AF branches.

Bestpfe.com

Appendix C: Evaluation of Eigenvector Periodicity Index (I_n)

The formulation of eigenvector periodicity index (I_n) is, briefly, as follows. Firstly, modal eigenvectors of the structure (nanowires in this study) are calculated by feeding the entire structure as a supercell. The lattice dynamics calculations are done by the GULP package [129]. Here we take

$$\Theta_n^{\alpha}\left(Y_j, Z_k\right) = \left(e_{n,I}^{\alpha}\, \mathcal{F}\left(y_i - Y_j\right) \mathcal{F}(z_i - Z_k)\right)$$

$$\mathcal{F}(x) = \begin{cases} 1 & x = 0 \\ 0 & x \neq 0 \end{cases}$$

where $\Theta_n^{\alpha}\left(Y_j, Z_k\right)$ represents the array of absolute value of eigenvector components along α direction corresponding to the n^{th} mode at Y_j, Z_k lateral spatial coordinates and $e_{n,i}^{\alpha}$ represents the eigenvector component of the i^{th} atom (equilibrium position of the i^{th} atom at [x_i , y_i , z_i]) along α direction corresponding to the n^{th} mode (refer to Figure 3-1). The spatial autocorrelation is performed to Θ_n^{α}, thereby, periodicity of the corresponding mode and coordinate components of a particular set of atoms can be evaluated. Subsequently, summation of autocorrelated Θ_n^{α} *(AC [*Θ_n^{α}*])* over all the lateral coordinates and Cartesian components are conducted as below.

$$\Pi_n^{\alpha} = \sum_{j,k} AC\left[\Theta_n^{\alpha}\left(Y_j, Z_k\right)\right]$$

BESTPFE.COM
List of research project topics and materials

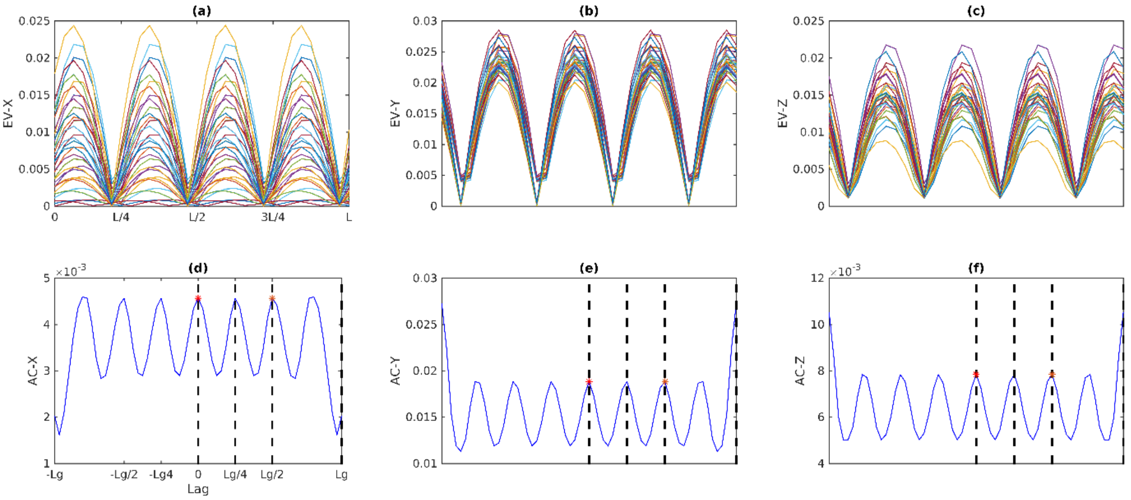

Figure C-1: Variation of Eigenvector components of PNW of mode $\boldsymbol{\omega}$= 0.3448 rad.THz along (a) X, (b) Y and (c) Z axis, and (d)-(f) corresponding autocorrelation (Π), respectively. The * at (d)-(f) denotes the corresponding points of lag equals 0 and $Lg/2$.

Figure C-1(a)-(c) illustrates the variation of eigenvector components (x, y and z respectively) along the structure's longitudinal length (L) for different lateral directions for a given mode as described above. Furthermore, Figure C-1(d)-(f) shows the corresponding Π_n^α against the lag. As can be seen Π_n^α follows a periodic pattern according to the eigenvector components. Subsequently, an index (I_n^α) is defined taking the standard deviation of the Π_n^α at lag of 0 and $Lg/2$.

$$I_n^\alpha = SD\left[1, {\Pi_n^\alpha @\,(lag = Lg/2)} \Big/ {\Pi_n^\alpha @\,(lag = 0)}\right]$$

The peak at $Lg/2$ can be seen for any kind of periodicity of eigenvector components, otherwise Π_n^α is seen to be decayed to zeros as shown in Figure C-2(e)-(f). When $I_n^\alpha = 0$ corresponds to a mode of periodic eigenvector distribution while aperiodic eigenvector distributions significantly deviate from 0 (see Figure 3-11). Finally I_n is defined as

$$I_n = \max\left[I_n^x, I_n^y, I_n^z\right].$$

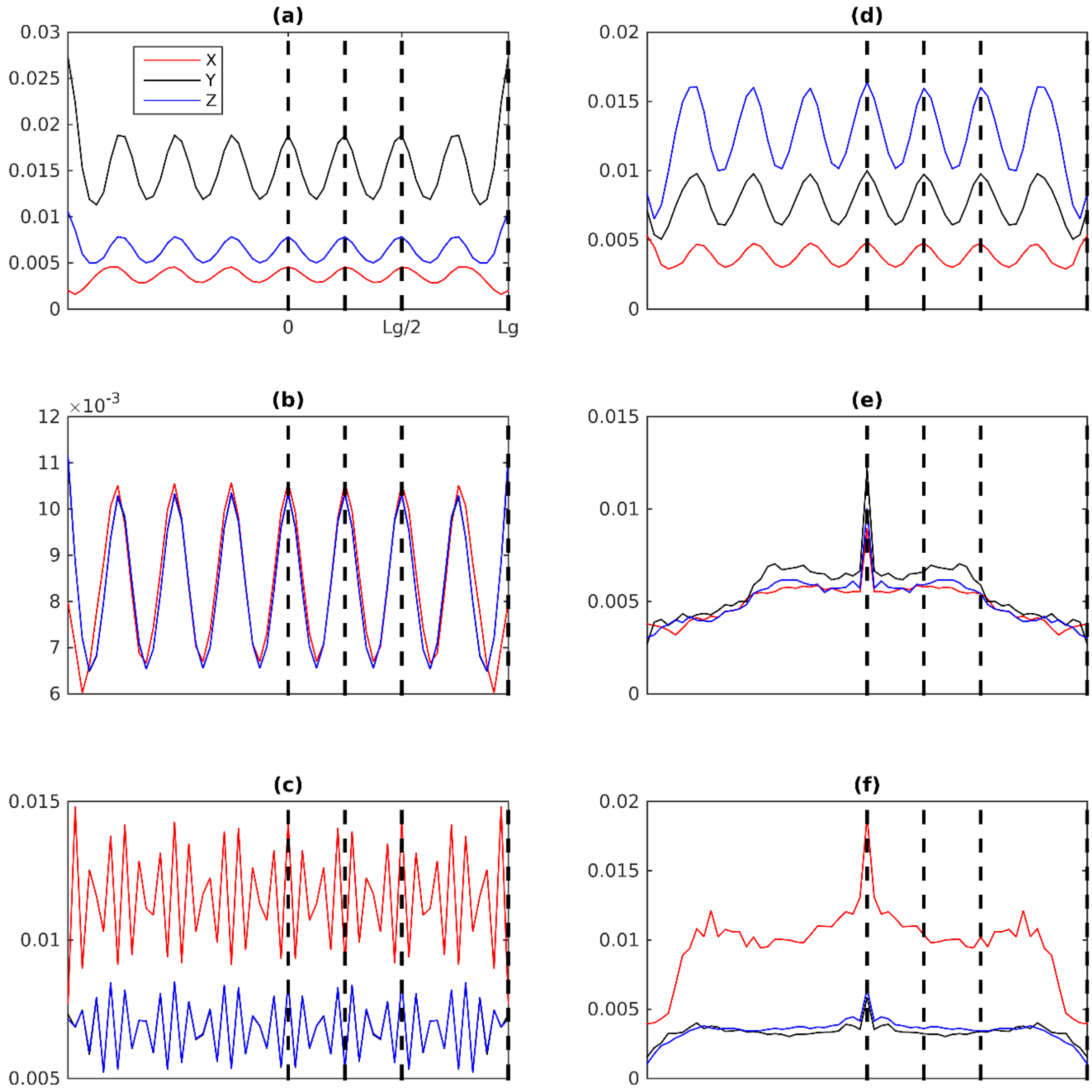

Figure C-2: *Π* of PNW for modes of $\boldsymbol{\omega}$ equals to (a) 0.3448, (b) 8.2554 and (c) 16.6858 rad.THz. *Π* of SANW of m_B=2m_A for modes of $\boldsymbol{\omega}$ equals to (a) 0.2903, (b) 7.0679 and (c) 16.4460 rad.THz.

Appendix D: Details of Random Layer Distributions

This section describes the layer thickness variation of type1 and type2 RLNWs illustrated in Figure 4-8. The uniform random distribution of layer thicknesses is characterised by two parameters: mean layer thickness and variance. Here type1 and type2 belong to two distributions of highest and lowest variances that can be defined while keeping the lowest layer thickness as single UC (0.543 nm). For example if the supposed mean layer thickness is 5 UCs (2.715 nm), the thickness distribution of highest variance ranges from 1UC to 9 UC with a variance of 20/3 UC^2 while the distribution of lowest variance ranges from 4UC to 6UC with a variance of 2/3 UC^2.

Mean layer thickness	Variance of type1	Variance of type2
2 UC=1.086 nm	2/3 UC^2	2/3 UC^2
3 UC=1.629 nm	2 UC^2	2/3 UC^2
5 UC=2.715 nm	20/3 UC^2	2/3 UC^2
7 UC=3.801 nm	14 UC^2	2/3 UC^2

Table D-1: The variance and mean layer thickness of type1 and type2 RLNWs

Appendix E: Comparison of TC of Two Types of NTRL Structures

Here the TCs given by NTRL of total length 90 nm of two different random twin boundary distributions are compared. NTRL type1 designates the structures discussed in the main manuscript (see Figure 5-2(a)) which follows the uniform random distributions corresponding to the mean-layer thicknesses 1.88, 3.76, 7.52 and 15.05 nm and variance of 0.5897 nm^2. But for the creation of NTRL type2, the procedure described in Wang et al. [49], [61] is followed in which there is no upper bound for the material layers. As can be seen from the figure, there is no significant difference of TC given by both structures.

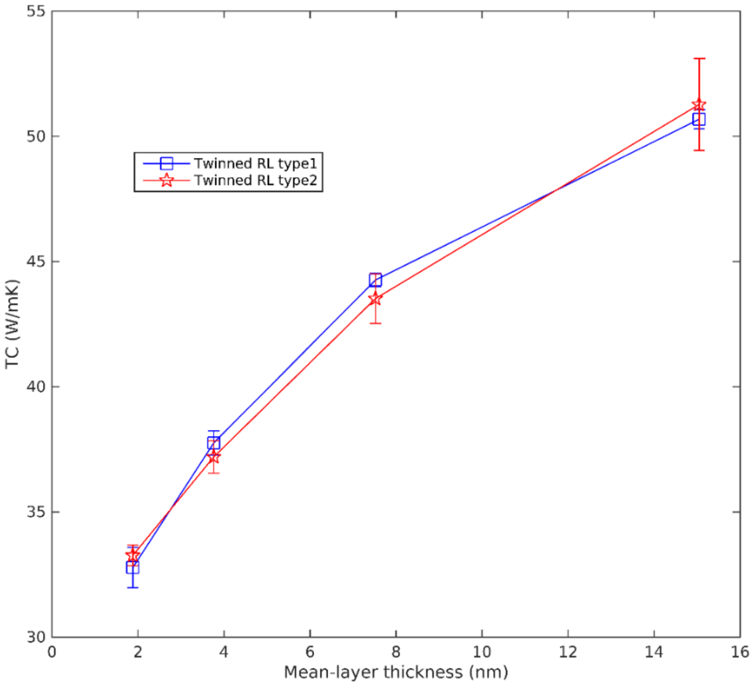

Figure E-1: Comparison of the TC of NTRL of two different random twin boundary distributions.

Appendix F: Statistics of Computational Simulations

In Figure F-1(a), the statistics of the number of NMD simulations against the number of atoms of corresponding structures of Chapter 3 are illustrated. Furthermore similar statistics are given in Figure F-1(b) for the NEMD simulations carried out in Chapters 4 and 5.

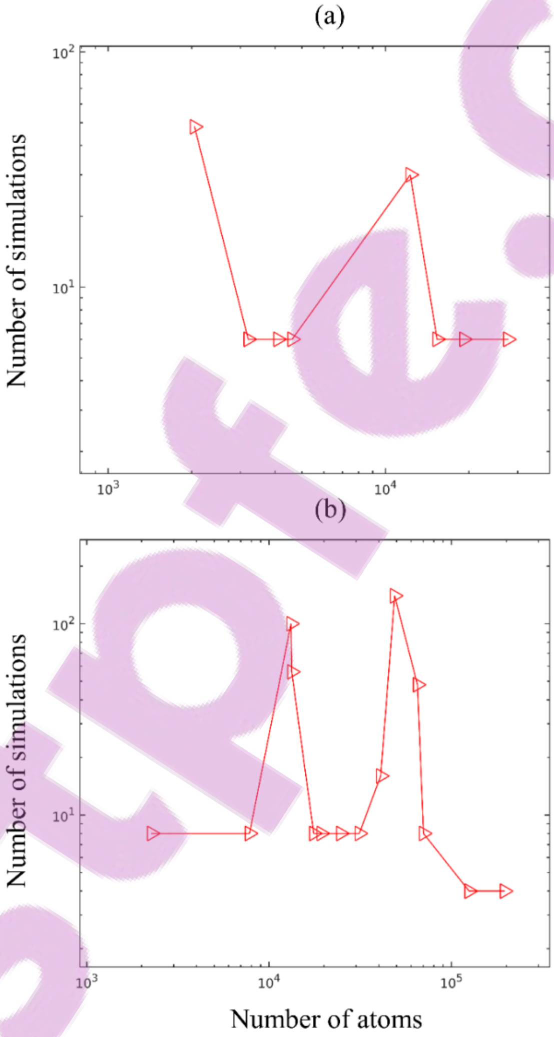

Figure F-1: (a)NMD simulations in Chapters 3 and (b) NEMD simulations in Chapters 4 and 5.

Bestpfe.com

References

[1] A. A. Balandin, “Thermal properties of graphene and nanostructured carbon materials.,” *Nat. Mater.*, vol. 10, no. 8, pp. 569–81, Aug. 2011.

[2] T. Borca-Tasciuc, W. Liu, J. Liu, T. Zeng, D. W. Song, C. D. Moore, G. Chen, K. L. Wang, M. S. Goorsky, T. Radetic, R. Gronsky, T. Koga, and M. S. Dresselhaus, “Thermal conductivity of symmetrically strained Si/Ge superlattices,” *Superlattices Microstruct.*, vol. 28, no. 3, pp. 199–206, Sep. 2000.

[3] C. C. Huang, C. K. Chiang, Z. H. Lin, K. H. Lee, and H. T. Chang, “Bioconjugated gold nanodots and nanoparticles for protein assays based on photoluminescence quenching,” *Anal. Chem.*, vol. 80, no. 5, pp. 1497–1504, 2008.

[4] B. I. Yakobson and P. Avouris, *Carbon Nanotubes*, vol. 80. 2001.

[5] M. J. Biercuk, S. Ilani, C. M. Marcus, and P. L. McEuen, “Electrical Transport in Single-Wall Carbon Nanotubes,” in *Carbon Nanotubes*, 2007, pp. 455–493.

[6] M. K. Samani, N. Khosravian, G. C. K. Chen, M. Shakerzadeh, D. Baillargeat, and B. K. Tay, “Thermal conductivity of individual multiwalled carbon nanotubes,” in *International Journal of Thermal Sciences*, 2012, vol. 62, pp. 40–43.

[7] A. I. Boukai, Y. Bunimovich, J. Tahir-Kheli, J.-K. Yu, W. A. Goddard, and J. R. Heath, “Silicon nanowires as efficient thermoelectric materials.” *Nature,* vol. 451, no. 7175, pp. 168–71, 2008.

[8] A. I. Hochbaum, R. Chen, R. D. Delgado, W. Liang, E. C. Garnett, M. Najarian, A. Majumdar, and P. Yang, “Enhanced thermoelectric performance of rough silicon nanowires,” *Nature,* vol. 451, no. 7175, pp. 163–167, 2008.

BESTPFE.COM
List of research project topics and materials

[9] S. Ghosh, I. Calizo, D. Teweldebrhan, E. P. Pokatilov, D. L. Nika, A. A. Balandin, W. Bao, F. Miao, and C. N. Lau, “Extremely high thermal conductivity of graphene: Prospects for thermal management applications in nanoelectronic circuits,” *Appl. Phys. Lett.*, vol. 92, no. 15, 2008.

[10] J.-K. Yu, S. Mitrovic, D. Tham, J. Varghese, and J. R. Heath, “Reduction of thermal conductivity in phononic nanomesh structures.,” *Nat. Nanotechnol.*, vol. 5, no. 10, pp. 718–21, 2010.

[11] F. Pan, Y. Wang, K. Jiang, Z. Ni, J. Ma, J. Zheng, R. Quhe, J. Shi, J. Yang, C. Chen, and J. Lu, “Silicene nanomesh,” *Sci. Rep.*, vol. 5, 2015.

[12] A. Suzuki, T. Yokotsuka, H. Tanaka, A. Yamada, and Y. Ohki, “Growth, characterization and avalanche photodiode application of strain compensated InGaAsP/InAlAs superlattice,” *J. Cryst. Growth*, vol. 237–239, no. 1–4 II, pp. 1510–1514, Apr. 2002.

[13] M. J. Bierman, Y. K. A. Lau, and S. Jin, “Hyperbranched PbS and PbSe nanowires and the effect of hydrogen gas on their synthesis,” *Nano Lett.*, vol. 7, no. 9, pp. 2907–2912, 2007.

[14] J. W. Jiang, N. Yang, B. S. Wang, and T. Rabczuk, “Modulation of thermal conductivity in kinked silicon nanowires: Phonon interchanging and pinching effects,” *Nano Lett.*, vol. 13, no. 4, pp. 1670–1674, 2013.

[15] C. K. Liu, C. K. Yu, H. C. Chien, S. L. Kuo, C. Y. Hsu, M. J. Dai, G. L. Luo, S. C. Huang, and M. J. Huang, “Thermal conductivity of Si/SiGe superlattice films,” *J. Appl. Phys.*, vol. 104, no. 11, 2008.

[16] T. Ookura, H. Toyota, M. Takeda, T. Kambayashi, and N. Uchitomi, “Preparation of

thermoelectric Si:B/SiGe multilayer structures on quartz glasses by RF-magnetron sputtering with layer-by-layer annealing methods," *Jpn. J. Appl. Phys.*, vol. 53, no. 8, 2014.

[17] T. Zhu and E. Ertekin, "Phonon transport on two-dimensional graphene/boron nitride superlattices," *Phys. Rev. B - Condens. Matter Mater. Phys.*, vol. 90, no. 19, 2014.

[18] D. Bischoff, M. Eich, A. Varlet, P. Simonet, H. C. Overweg, K. Ensslin, and T. Ihn, "Graphene nano-heterostructures for quantum devices," *Materials Today*, vol. 19, no. 7. pp. 375–381, 2016.

[19] C.-Y. Wen, M. C. Reuter, J. Bruley, J. Tersoff, S. Kodambaka, E. A. Stach, and F. M. Ross, "Formation of Compositionally Abrupt Axial Heterojunctions in Silicon-Germanium Nanowires," *Science (80-.).*, vol. 326, no. 5957, pp. 1247–1250, 2009.

[20] L. J. Lauhon, M. S. Gudlksen, D. Wang, and C. M. Lieber, "Epitaxial core-shell and core-multishell nanowire heterostructures," *Nature*, vol. 420, no. 6911, pp. 57–61, 2002.

[21] D. G. Ramlan, S. J. May, J. G. Zheng, J. E. Allen, B. W. Wessels, and L. J. Lauhon, "Ferromagnetic Self-Assembled Quantum Dots on Semiconductor Nanoparticles," *Nano Lett.*, vol. 6, pp. 50–54, 2006.

[22] K. Tomioka, J. Motohisa, S. Hara, and T. Fukui, "Control of InAs nanowire growth directions on Si," *Nano Lett.*, vol. 8, no. 10, pp. 3475–3480, 2008.

[23] Z. Li, S. Tan, E. Bozorg-Grayeli, T. Kodama, M. Asheghi, G. Delgado, M. Panzer, A. Pokrovsky, D. Wack, and K. E. Goodson, "Phonon dominated heat conduction normal to Mo/Si multilayers with period below 10 nm.," *Nano Lett.*, vol. 12, no. 6, pp. 3121–6, Jun. 2012.

[24] L. Vayssieres, “Growth of Arrayed Nanorods and Nanowires of ZnO from Aqueous Solutions,” *Adv. Mater.*, vol. 15, no. 5, pp. 464–466, Mar. 2003.

[25] Z. F. Ren, “Synthesis of Large Arrays of Well-Aligned Carbon Nanotubes on Glass,” *Science (80-.).*, vol. 282, no. 5391, pp. 1105–1107, Nov. 1998.

[26] Z. G. Chen, G. Hana, L. Yanga, L. Cheng, and J. Zou, “Nanostructured thermoelectric materials: Current research and future challenge,” *Progress in Natural Science: Materials International*, vol. 22, no. 6. pp. 535–549, 2012.

[27] X. Zhang and L.-D. Zhao, “Thermoelectric materials: Energy conversion between heat and electricity,” *J. Mater.*, vol. 1, no. 2, pp. 92–105, 2015.

[28] T. M. Tritt and M. A Subramanian, “Thermoelectric Materials, Phenomena, and Applications: A Bird’s Eye View,” *MRS Bull.*, vol. 31, no. 3, pp. 188–198, 2006.

[29] A. F. Ioffe, “Semiconductor thermoelements and thermoelec,” *Phys. Today,* vol. 12, no. 5, p. 42, 1959.

[30] H. J. Goldsmid, A. R. Sheard, and D. A. Wright, “The performance of bismuth telluride thermojunctions,” *Br. J. Appl. Phys.*, vol. 9, no. 9, pp. 365–370, 1958.

[31] M. G. Kanatzidis, “Nanostructured thermoelectrics: The new paradigm?,” *Chemistry of Materials*, vol. 22, no. 3. pp. 648–659, 2010.

[32] L. D. Hicks and M. S. Dresselhaus, “Effect of quantum-well structures on the thermoelectric figure of merit,” *Physical Review B*, vol. 47, no. 19. pp. 12727–12731, 1993.

[33] P. Vaqueiro and A. V. Powell, “Recent developments in nanostructured materials for high-performance thermoelectrics,” *J. Mater. Chem.*, vol. 20, no. 43, p. 9577, 2010.

[34] J. P. Dismukes, L. Ekstrom, E. F. Steigmeier, I. Kudman, and D. S. Beers, “Thermal and electrical properties of heavily doped Ge-Si alloys up to 1300°K,” *J. Appl. Phys.*, vol. 35, no. 10, pp. 2899–2907, 1964.

[35] G. A. Slack, “New Materials and Performance Limits for Thermoelectric Cooling,” in *CRC Handbook of Thermoelectrics*, 1995, pp. 407–437.

[36] B. C. Sales, D. Mandrus, B. C. Chakoumakos, V. Keppens, and J. R. Thompson, “Filled skutterudite antimonides: Electron crystals and phonon glasses,” *Phys. Rev. B*, vol. 56, no. 23, pp. 15081–15089, 1997.

[37] B. C. Sales, D. Mandrus, and R. K. Williams, “Filled Skutterudite Antimonides: A New Class of Thermoelectric Materials,” *Science (80-.).*, vol. 272, no. 5266, pp. 1325–1328, 1996.

[38] R. Venkatasubramanian, E. Siivola, T. Colpitts, and B. O’Quinn, “Thin-film thermoelectric devices with high room-temperature figures of merit,” *Nature*, vol. 413, no. 6856, pp. 597–602, 2001.

[39] S. K. Bux, R. G. Blair, P. K. Gogna, H. Lee, G. Chen, M. S. Dresselhaus, R. B. Kaner, and J. P. Fleurial, “Nanostructured bulk silicon as an effective thermoelectric material,” *Adv. Funct. Mater.*, vol. 19, no. 15, pp. 2445–2452, 2009.

[40] L. D. Hicks and M. S. Dresselhaus, “Thermoelectric figure of merit of a one-dimensional conductor,” *Phys. Rev. B*, vol. 47, no. 24, pp. 16631–16634, 1993.

[41] C. L. Tien and G. Chen, “Challenges in Microscale Conductive and Radiative Heat Transfer,” *J. Heat Transfer*, vol. 116, no. 4, p. 799, 1994.

[42] R. Anufriev, A. Ramiere, J. Maire, and M. Nomura, “Heat guiding and focusing using

ballistic phonon transport in phononic nanostructures," *Nat. Commun.*, vol. 8, 2017.

[43] H. F. C. Hoevers, M. L. Ridder, A. Germeau, M. P. Bruijn, P. A. J. De Korte, and R. J. Wiegerink, "Radiative ballistic phonon transport in silicon-nitride membranes at low temperatures," *Appl. Phys. Lett.*, vol. 86, no. 25, pp. 1–3, 2005.

[44] J. A. Johnson, A. A. Maznev, J. Cuffe, J. K. Eliason, A. J. Minnich, T. Kehoe, C. M. S. Torres, G. Chen, and K. A. Nelson, "Direct measurement of room-temperature nondiffusive thermal transport over micron distances in a silicon membrane," *Phys. Rev. Lett.*, vol. 110, no. 2, 2013.

[45] Y. K. Koh, Y. Cao, D. G. Cahill, and D. Jena, "Heat-transport mechanisms in superlattices," *Adv. Funct. Mater.*, vol. 19, no. 4, pp. 610–615, 2009.

[46] M. N. Luckyanova, J. Garg, K. Esfarjani, A. Jandl, M. T. Bulsara, A. J. Schmidt, A. J. Minnich, S. Chen, M. S. Dresselhaus, Z. Ren, E. A. Fitzgerald, and G. Chen, "Coherent phonon heat conduction in superlattices.," *Science*, vol. 338, no. 6109, pp. 936–9, Nov. 2012.

[47] B. Latour, S. Volz, and Y. Chalopin, "Microscopic description of thermal-phonon coherence: From coherent transport to diffuse interface scattering in superlattices," *Phys. Rev. B - Condens. Matter Mater. Phys.*, vol. 90, no. 1, pp. 1–9, 2014.

[48] B. Latour and Y. Chalopin, "Distinguishing between spatial coherence and temporal coherence of phonons," *Phys. Rev. B*, vol. 95, no. 21, 2017.

[49] Y. Wang, H. Huang, and X. Ruan, "Decomposition of coherent and incoherent phonon conduction in superlattices and random multilayers," *Phys. Rev. B - Condens. Matter Mater. Phys.*, vol. 90, no. 16, p. 165406, 2014.

[50] M. Maldovan, “Phonon wave interference and thermal bandgap materials,” *Nat. Mater.*, vol. 14, no. 7, pp. 667–674, 2015.

[51] M. Prunnila and J. Meltaus, “Acoustic phonon tunneling and heat transport due to evanescent electric fields,” *Phys. Rev. Lett.*, vol. 105, no. 12, 2010.

[52] S. Pailhès, H. Euchner, V. M. Giordano, R. Debord, A. Assy, S. Gomès, A. Bosak, D. Machon, S. Paschen, and M. De Boissieu, “Localisation of propagative phonons in a perfectly crystalline solid,” *Phys. Rev. Lett.*, vol. 113, no. 2, 2014.

[53] J. Ravichandran, A. K. Yadav, R. Cheaito, P. B. Rossen, A. Soukiassian, S. J. Suresha, J. C. Duda, B. M. Foley, C.-H. Lee, Y. Zhu, A. W. Lichtenberger, J. E. Moore, D. A. Muller, D. G. Schlom, P. E. Hopkins, A. Majumdar, R. Ramesh, and M. A. Zurbuchen, “Crossover from incoherent to coherent phonon scattering in epitaxial oxide superlattices,” *Nat. Mater.*, vol. 13, no. February, p. 168, 2013.

[54] M. Simkin and G. Mahan, “Minimum thermal conductivity of superlattices,” *Phys. Rev. Lett.*, vol. 84, no. 5, pp. 927–30, 2000.

[55] K. W. Adu, H. R. Gutirrez, U. J. Kim, G. U. Sumanasekera, and P. C. Eklund, “Confined phonons in Si nanowires,” *Nano Lett.*, vol. 5, no. 3, pp. 409–414, 2005.

[56] E. Fermi, J. Pasta, and S. Ulam, “Studies of nonlinear problems,” *Los Alamos Rep. LA-1940*, 1955.

[57] T. Prosen and D. K. Campbell, “Momentum conservation implies anomalous energy transport in ID classical lattices,” *Phys. Rev. Lett.*, vol. 84, no. 13, 2000.

[58] C. W. Chang, D. Okawa, H. Garcia, A. Majumdar, and A. Zettl, “Breakdown of fourier’s law in nanotube thermal conductors,” *Phys. Rev. Lett.*, vol. 101, no. 7, p.

75903, 2008.

[59] B. Li and J. Wang, “Anomalous heat conduction and anomalous diffusion in one-dimensional systems.,” *Phys. Rev. Lett.*, vol. 91, no. 4, p. 44301, 2003.

[60] H. Zhao, “Identifying diffusion processes in one-dimensional lattices in thermal equilibrium,” *Phys. Rev. Lett.*, vol. 96, no. 14, 2006.

[61] Y. Wang, C. Gu, and X. Ruan, “Optimization of the random multilayer structure to break the random-alloy limit of thermal conductivity,” *Appl. Phys. Lett.*, vol. 106, no. 7, p. 73104, 2015.

[62] Q. Hao, G. Zhu, G. Joshi, X. Wang, A. Minnich, Z. Ren, and G. Chen, “Theoretical studies on the thermoelectric figure of merit of nanograined bulk silicon,” *Appl. Phys. Lett.*, vol. 97, no. 6, 2010.

[63] X. Huang, X. Huai, S. Liang, and X. Wang, “Thermal transport in Si/Ge nanocomposites,” *J. Phys. D. Appl. Phys.*, vol. 42, no. 9, p. 95416, 2009.

[64] Z. Wang, J. E. Alaniz, W. Jang, J. E. Garay, and C. Dames, “Thermal conductivity of nanocrystalline silicon: Importance of grain size and frequency-dependent mean free paths,” *Nano Lett.*, vol. 11, no. 6, pp. 2206–2213, 2011.

[65] A. Porter, C. Tran, and F. Sansoz, “Intrinsic nanotwin effect on thermal boundary conductance in bulk and single-nanowire twinning superlattices,” *Phys. Rev. B*, vol. 93, no. 19, p. 195431, 2016.

[66] H. Dong, J. Xiao, R. Melnik, and B. Wen, “Weak phonon scattering effect of twin boundaries on thermal transmission,” *Sci. Rep.*, vol. 6, p. 19575, 2016.

[67] H. Dong, B. Wen, Y. Zhang, and R. Melnik, “Low thermal conductivity in Si/Ge

hetero-twinned superlattices," *RSC Adv.*, vol. 7, no. 48, pp. 29959–29965, 2017.

[68] M. Tuckermana, R. April, G. J. Martyna, M. L. Klein, M. E. Tuckerman, P. J. Ungar, T. von Rosenvinge, and T. von Rosenvinge, "Ab Initio Molecular Dynamics Simulations," *J. Phys. Chem.*, vol. 3654, no. 96, pp. 12878–12887, 1996.

[69] Q. Zhao, L. Xie, and H. J. Kulik, "Discovering Amorphous Indium Phosphide Nanostructures with High-Temperature ab Initio Molecular Dynamics," *J. Phys. Chem. C*, vol. 119, no. 40, pp. 23238–23249, 2015.

[70] J. E. Turney, A. J. H. McGaughey, and C. H. Amon, "Assessing the applicability of quantum corrections to classical thermal conductivity predictions," *Phys. Rev. B - Condens. Matter Mater. Phys.*, vol. 79, no. 22, 2009.

[71] C. Z. Wang, C. T. Chan, and K. M. Ho, "Tight-binding molecular-dynamics study of phonon anharmonic effects in silicon and diamond," *Phys. Rev. B*, vol. 42, no. 17, pp. 11276–11283, 1990.

[72] Y. H. Lee, R. Biswas, C. M. Soukoulis, C. Z. Wang, C. T. Chan, and K. M. Ho, "Molecular-dynamics simulation of thermal conductivity in amorphous silicon," *Phys. Rev. B*, vol. 43, no. 8, pp. 6573–6580, 1991.

[73] D. Frenkel and B. Smit, *Understanding Molecular Simulation*. Elsevier, 2002.

[74] K. Choudhary, F. Y. P. Congo, T. Liang, C. Becker, R. G. Hennig, and F. Tavazza, "Evaluation and comparison of classical interatomic potentials through a user-friendly interactive web-interface," *Sci. Data*, vol. 4, 2017.

[75] F. H. Stillinger and T. A. Weber, "Computer simulation of local order in condensed phases of silicon," *Phys. Rev. B*, vol. 31, no. 8, pp. 5262–5271, Apr. 1985.

Bestpfe.com

[76] J. E. Jones, “On the Determination of Molecular Fields. I. From the Variation of the Viscosity of a Gas with Temperature,” *Proc. R. Soc. A Math. Phys. Eng. Sci.*, vol. 106, no. 738, pp. 441–462, 1924.

[77] A. J. H. McGaughey and M. Kaviany, “Thermal conductivity decomposition and analysis using molecular dynamics simulations. Part I. Lennard-Jones argon,” *Int. J. Heat Mass Transf.*, vol. 47, no. 8–9, pp. 1799–1816, Apr. 2004.

[78] E. S. Landry, M. I. Hussein, and a. J. H. McGaughey, “Complex superlattice unit cell designs for reduced thermal conductivity,” *Phys. Rev. B - Condens. Matter Mater. Phys.*, vol. 77, no. 18, p. 184302, 2008.

[79] E. S. Landry and A. J. H. McGaughey, “Effect of film thickness on the thermal resistance of confined semiconductor thin films,” *J. Appl. Phys.*, vol. 107, no. 1, 2010.

[80] E. S. Landry and A. J. H. McGaughey, “Effect of interfacial species mixing on phonon transport in semiconductor superlattices,” *Phys. Rev. B*, vol. 79, no. 7, p. 75316, Feb. 2009.

[81] J. M. Larkin and A. J. H. McGaughey, “Predicting alloy vibrational mode properties using lattice dynamics calculations, molecular dynamics simulations, and the virtual crystal approximation,” *J. Appl. Phys.*, vol. 114, no. 2, p. 23507, 2013.

[82] X. Yang, A. C. To, and R. Tian, “Anomalous heat conduction behavior in thin finite-size silicon nanowires,” *Nanotechnology*, vol. 21, no. 15, 2010.

[83] I. Ponomareva, D. Srivastava, and M. Menon, “Thermal conductivity in thin silicon nanowires: Phonon confinement effect,” *Nano Lett.*, vol. 7, no. 5, pp. 1155–1159, 2007.

[84] J. Tersoff, “New empirical approach for the structure and energy of covalent systems,” *Phys. Rev. B*, vol. 37, no. 12, pp. 6991–7000, Apr. 1988.

[85] J. Tersoff, “Modeling solid-state chemistry: Interatomic potentials for multicomponent systems,” *Phys. Rev. B*, vol. 39, no. 8, pp. 5566–5568, 1989.

[86] D. Donadio and G. Galli, “Atomistic simulations of heat transport in silicon nanowires,” *Phys. Rev. Lett.*, vol. 102, no. 19, p. 195901, 2009.

[87] M. Hu and D. Poulikakos, “Si/Ge superlattice nanowires with ultralow thermal conductivity.,” *Nano Lett.*, vol. 12, no. 11, pp. 5487–94, Nov. 2012.

[88] Y. Zhou and M. Hu, “Record Low Thermal Conductivity of Polycrystalline Si Nanowire: Breaking the Casimir Limit by Severe Suppression of Propagons,” *Nano Lett.*, vol. 16, no. 10, pp. 6178–6187, 2016.

[89] D. Donadio and G. Galli, “Thermal conductivity of isolated and interacting carbon nanotubes: Comparing results from molecular dynamics and the Boltzmann transport equation,” *Phys. Rev. Lett.*, vol. 99, no. 25, p. 255502, 2007.

[90] J. R. Lukes, D. Y. Li, X.-G. Liang, and C.-L. Tien, “Molecular dynamics study of solid thin-film thermal conductivity,” *J. Heat Transfer*, vol. 122, no. August, pp. 536–543, 2000.

[91] E. S. Landry, “Thermal transport by phonons across semiconductor interfaces, thin films, and superlattices,” Carnegie Mellon University, 2009.

[92] P. K. Schelling, S. R. Phillpot, and P. Keblinski, “Comparison of atomic-level simulation methods for computing thermal conductivity,” *Phys. Rev. B*, vol. 65, no. 14, p. 144306, Apr. 2002.

BESTPFE.COM
List of research project topics and materials

[93] X. Mu, L. Wang, X. Yang, P. Zhang, A. C. To, and T. Luo, “Ultra-low Thermal Conductivity in Si/Ge Hierarchical Superlattice Nanowire,” *Sci. Rep.*, vol. 5, p. 16697, 2015.

[94] G. Chen, *Nanoscale Energy Transport and Conversion*. Oxford University Press, 2005.

[95] M. S. Green, “Markoff Random Processes and the Statistical Mechanics of Time-Dependent Phenomena. II. Irreversible Processes in Fluids,” *J. Chem. Phys.*, vol. 22, no. 3, pp. 398–413, 1954.

[96] R. Kubo, “Statistical Mechanical Theory of Irreversible Processes. I. General Theory and Simple Applications to Magnetic and Conduction Problems,” *J. Phys. Soc. Japan*, vol. 12, no. 6, pp. 570–586, 1957.

[97] R. Kubo, “The fluctuation-dissipation theorem,” *Reports Prog. Phys.*, vol. 29, no. 1, pp. 255–284, Jan. 1966.

[98] R. Vogelsang, C. Hoheisel, and G. Ciccotti, “Thermal conductivity of the Lennard-Jones liquid by molecular dynamics calculations,” *J. Chem. Phys.*, vol. 86, no. 11, pp. 6371–6375, 1987.

[99] K. V. Tretiakov and S. Scandolo, “Thermal conductivity of solid argon from molecular dynamics simulations,” *J. Chem. Phys.*, vol. 120, no. 8, pp. 3765–3769, 2004.

[100] W. Deng, W. A Goddard, J. Che, C. Tahir, T. Tahir Cagin, W. Deng, and W. A. Goddard III, “Thermal conductivity of diamond and related materials from molecular dynamics simulations,” *J. Chem. Phys.*, 2000.

[101] S. G. Volz and G. Chen, “Molecular-dynamics simulation of thermal conductivity of

silicon crystals," *Phys. Rev. B*, vol. 61, no. 4, pp. 2651–2656, 2000.

[102] Y. Zhou, X. Zhang, and M. Hu, "Nonmonotonic Diameter Dependence of Thermal Conductivity of Extremely Thin Si Nanowires: Competition between Hydrodynamic Phonon Flow and Boundary Scattering," *Nano Lett.*, vol. 17, no. 2, pp. 1269–1276, 2017.

[103] G. P. Srivastava, *The phyiscs of phonons*. New York: Taylor & Francis Group, 1990.

[104] M. T. Dove, *introduction to lattice dynamics*. Cambridge University press, 1993.

[105] R. L. Liboff, *Kinetic Theory: Classical, Quantum, and Relativistic Descriptions*. 2003.

[106] A. J. H. McGaughey and M. Kaviany, "Quantitative validation of the Boltzmann transport equation phonon thermal conductivity model under the single-mode relaxation time approximation," *Phys. Rev. B*, vol. 69, no. 9, p. 94303, 2004.

[107] J. M. Larkin and A. J. H. McGaughey, "Thermal conductivity accumulation in amorphous silica and amorphous silicon," *Phys. Rev. B - Condens. Matter Mater. Phys.*, vol. 89, no. 14, p. 144303, 2014.

[108] A. A. Maradudin and A. E. Fein, "Scattering of neutrons by an anharmonic crystal," *Phys. Rev.*, vol. 128, no. 6, pp. 2589–2608, 1962.

[109] C. Kittel, *Introduction to solid state physics*. Wiley-VCH, 2005.

[110] P. B. Allen and J. L. Feldman, "Thermal conductivity of disordered harmonic solids," *Phys. Rev. B*, vol. 48, no. 17, pp. 12581–12588, 1993.

[111] P. B. Allen, J. L. Feldman, J. Fabian, and F. Wooten, "Diffusons, locons and propagons: Character of atomie yibrations in amorphous Si," *Philos. Mag. B Phys. Condens. Matter; Stat. Mech. Electron. Opt. Magn. Prop.*, vol. 79, no. 11–12, pp.

1715–1731, 1999.

[112] R. Prasher, T. Tong, and A. Majumdar, “Approximate analytical models for phonon specific heat and ballistic thermal conductance of nanowires,” *Nano Lett.*, vol. 8, no. 1, pp. 99–103, 2008.

[113] N. S. Mohammad, “Understanding quantum confinement in nanowires: basics, applications and possible laws,” *J. Phys. Condens. Matter*, vol. 26, no. 42, p. 423202, 2014.

[114] D. L. Nika, E. P. Pokatilov, A. A. Balandin, V. M. Fomin, A. Rastelli, and O. G. Schmidt, “Reduction of lattice thermal conductivity in one-dimensional quantum-dot superlattices due to phonon filtering,” *Phys. Rev. B - Condens. Matter Mater. Phys.*, vol. 84, no. 16, p. 165415, 2011.

[115] K. Schwab, E. A. Henriksen, J. M. Worlock, and M. L. Roukes, “Measurement of the quantum of thermal conductance,” *Nature*, vol. 404, no. 6781, pp. 974–977, 2000.

[116] S. Lepri, R. Livi, and A. Politi, “Thermal conduction in classical low-dimensional lattices,” *Physics Reports*, vol. 377, no. 1. pp. 1–80, 2003.

[117] A. Dhar, “Heat conduction in the disordered harmonic chain revisited,” *Phys. Rev. Lett.*, vol. 86, no. 26 I, pp. 5882–5885, 2001.

[118] G. Wu and J. Dong, “Anomalous heat conduction in a carbon nanowire: Molecular dynamics calculations,” *Phys. Rev. B - Condens. Matter Mater. Phys.*, vol. 71, no. 11, p. 115410, 2005.

[119] N. Mingo and D. A. Broido, “Length dependence of carbon nanotube thermal conductivity and the ‘problem of long waves,’” *Nano Lett.*, vol. 5, no. 7, pp. 1221–

1225, 2005.

[120] D. L. Nika, A. S. Askerov, and A. A. Balandin, “Anomalous size dependence of the thermal conductivity of graphene ribbons,” *Nano Lett.*, vol. 12, no. 6, pp. 3238–3244, 2012.

[121] H. Karamitaheri, N. Neophytou, and H. Kosina, “Anomalous diameter dependence of thermal transport in ultra-narrow Si nanowires,” *J. Appl. Phys.*, vol. 115, no. 2, p. 24302, 2014.

[122] S. C. Huberman, J. M. Larkin, A. J. H. McGaughey, and C. H. Amon, “Disruption of superlattice phonons by interfacial mixing,” *Phys. Rev. B - Condens. Matter Mater. Phys.*, vol. 88, no. 15, p. 155311, 2013.

[123] J. Chen, G. Zhang, and B. Li, “Tunable thermal conductivity of Si1−xGex nanowires,” *Appl. Phys. Lett.*, vol. 95, no. 7, p. 73117, 2009.

[124] A. El Sachat, J. S. Reparaz, J. Spiece, M. I. Alonso, A. R. Goñi, M. Garriga, P. O. Vaccaro, M. R. Wagner, O. V. Kolosov, C. M. Sotomayor Torres, and F. Alzina, “Thermal transport in epitaxial Si1-xGex alloy nanowires with varying composition and morphology,” *Nanotechnology*, vol. 28, no. 50, p. 505704, 2017.

[125] Y. Wang, B. Li, and G. Xie, “Significant reduction of thermal conductivity in silicon nanowires by shell doping,” *RSC Adv.*, vol. 3, no. 48, p. 26074, 2013.

[126] J. W. Lee, J. Lee, S. H. Jung, Y. Jang, B. L. Choi, C. W. Yang, D. Whang, and E. K. Lee, “Large reduction in thermal conductivity for SiGe alloy nanowire wrapped with a Ge nanoparticle-embedded SiO2 shell,” *Nanotechnology*, vol. 27, no. 30, p. 305703, 2016.

[127] G. Xie, B. Li, L. Yang, J. Cao, Z. Guo, M. Tang, and J. Zhong, “Ultralow thermal conductivity in Si/Ge x Si 1−x core-shell nanowires,” *J. Appl. Phys.*, vol. 113, no. 8, p. 83501, 2013.

[128] G. Zhang and B. Li, “Impacts of doping on thermal and thermoelectric properties of nanomaterials,” *Nanoscale*, vol. 2, no. 7, p. 1058, 2010.

[129] J. D. Gale and A. L. Rohl, “The General Utility Lattice Program (GULP),” *Mol. Simul.*, vol. 29, no. 5, pp. 291–341, 2003.

[130] R. J. Bell and P. Dean, “Atomic vibrations in vitreous silica,” *Discuss. Faraday Soc.*, vol. 50, p. 55, 1970.

[131] A. Chaudhuri, A. Kundu, D. Roy, A. Dhar, J. L. Lebowitz, and H. Spohn, “Heat transport and phonon localisation in mass-disordered harmonic crystals,” *Phys. Rev. B - Condens. Matter Mater. Phys.*, vol. 81, no. 6, p. 64301, 2010.

[132] A. J. H. McGaughey, “Phonon transport in molecular dynamics simulations: formulation and thermal conductivity prediction,” University of Mchigani, 2004.

[133] L. Lindsay, D. A. Broido, and T. L. Reinecke, “Thermal conductivity and large isotope effect in GaN from first principles,” *Phys. Rev. Lett.*, vol. 109, no. 9, p. 95901, 2012.

[134] A. Ward, D. A. Broido, D. A. Stewart, and G. Deinzer, “Ab initio theory of the lattice thermal conductivity in diamond,” *Phys. Rev. B - Condens. Matter Mater. Phys.*, vol. 80, no. 12, p. 125203, 2009.

[135] M. G. Holland, “Analysis of lattice thermal conductivity,” *Phys. Rev.*, vol. 132, no. 6, pp. 2461–2471, 1963.

[136] K. Esfarjani, G. Chen, and H. T. Stokes, “Heat transport in silicon from first-principles

calculations," *Phys. Rev. B - Condens. Matter Mater. Phys.*, vol. 84, no. 8, p. 85204, 2011.

[137] A. Cepellotti, G. Fugallo, L. Paulatto, M. Lazzeri, F. Mauri, and N. Marzari, "Phonon hydrodynamics in two-dimensional materials," *Nat. Commun.*, vol. 6, p. 6400, 2015.

[138] Z. Ding, J. Zhou, B. Song, V. Chiloyan, M. Li, T. H. Liu, and G. Chen, "Phonon Hydrodynamic Heat Conduction and Knudsen Minimum in Graphite," *Nano Lett.*, vol. 18, no. 1, pp. 638–649, 2018.

[139] H. R. Seyf and A. Henry, "A method for distinguishing between propagons, diffusions, and locons," *J. Appl. Phys.*, vol. 120, no. 2, p. 25101, 2016.

[140] B. Abeles, "Lattice thermal conductivity of disordered semiconductor alloys at high temperatures," *Phys. Rev.*, vol. 131, no. 5, pp. 1906–1911, 1963.

[141] P. G. Klemens, "The Scattering of Low-Frequency Lattice Waves by Static Imperfections," *Proc. Phys. Soc. Sect. A*, vol. 68, no. 12, pp. 1113–1128, 1955.

[142] J. Callaway, "Model for lattice thermal conductivity at low temperatures," *Phys. Rev.*, vol. 113, no. 4, pp. 1046–1051, 1959.

[143] J. Lee, W. Lee, J. Lim, Y. Yu, Q. Kong, J. J. Urban, and P. Yang, "Thermal Transport in Silicon Nanowires at High Temperature up to 700 K," *Nano Lett.*, vol. 16, no. 7, pp. 4133–4140, 2016.

[144] D. Li, Y. Wu, R. Fan, P. Yang, and A. Majumdar, "Thermal conductivity of Si/SiGe superlattice nanowires," *Appl. Phys. Lett.*, vol. 83, no. 15, pp. 3186–3188, Oct. 2003.

[145] D. Ma, H. Ding, H. Meng, L. Feng, Y. Wu, J. Shiomi, and N. Yang, "Nano-cross-junction effect on phonon transport in silicon nanowire cages," *Phys. Rev. B*, vol. 94,

no. 16, 2016.

[146] J. Chen, G. Zhang, and B. Li, “A universal gauge for thermal conductivity of silicon nanowires with different cross sectional geometries,” *J. Chem. Phys.*, vol. 135, no. 20, pp. 1–8, 2011.

[147] J. Hattori and S. Uno, “Impact of isotope doping on phonon thermal transport in silicon nanowires,” in *Japanese Journal of Applied Physics*, 2013, vol. 52, no. 4 PART 2.

[148] N. Yang, G. Zhang, and B. Li, “Ultralow thermal conductivity of isotope-doped silicon nanowires,” *Nano Lett.*, vol. 8, no. 1, pp. 276–280, Jan. 2008.

[149] W. Chen, L. Yu, S. Misra, Z. Fan, P. Pareige, G. Patriarche, S. Bouchoule, and P. R. I. Cabarrocas, “Incorporation and redistribution of impurities into silicon nanowires during metal-particle-assisted growth.,” *Nat. Commun.*, vol. 5, no. May, p. 4134, 2014.

[150] K. Q. Chen, W. X. Li, W. Duan, Z. Shuai, and B. L. Gu, “Effect of defects on the thermal conductivity in a nanowire,” *Phys. Rev. B*, vol. 72, no. 4, p. , 2005.

[151] T. Markussen, A. P. Jauho, and M. Brandbyge, “Heat conductance is strongly anisotropic for pristine silicon nanowires,” *Nano Lett.*, vol. 8, no. 11, pp. 3771–3775, Nov. 2008.

[152] Y. Zhao, L. Yang, L. Kong, M. H. Nai, D. Liu, J. Wu, Y. Liu, S. Y. Chiam, W. K. Chim, C. T. Lim, B. Li, J. T. L. Thong, and K. Hippalgaonkar, “Ultralow Thermal Conductivity of Single-Crystalline Porous Silicon Nanowires,” *Adv. Funct. Mater.*, vol. 27, no. 40, p. 1702824, 2017.

[153] J. Sadhu and S. Sinha, “Room-temperature phonon boundary scattering below the

Casimir limit," *Phys. Rev. B - Condens. Matter Mater. Phys.*, vol. 84, no. 11, Sep. 2011.

[154] J. Lim, K. Hippalgaonkar, S. C. Andrews, A. Majumdar, and P. Yang, "Quantifying surface roughness effects on phonon transport in silicon nanowires," *Nano Lett.*, vol. 12, no. 5, pp. 2475–2482, May 2012.

[155] H. Li and R. Zhang, "Anomalous effect of hydrogenation on phonon thermal conductivity in thin silicon nanowires," *EPL Europhys. Lett.*, vol. 105, no. 5, p. 56003, Mar. 2014.

[156] M. Hu, X. Zhang, K. P. Giapis, and D. Poulikakos, "Thermal conductivity reduction in core-shell nanowires," *Phys. Rev. B - Condens. Matter Mater. Phys.*, vol. 84, no. 8, Aug. 2011.

[157] C. Dames and G. Chen, "Theoretical phonon thermal conductivity of Si/Ge superlattice nanowires," *J. Appl. Phys.*, vol. 95, no. 2, pp. 682–693, Jan. 2004.

[158] M. C. Wingert, Z. C. Y. Chen, E. Dechaumphai, J. Moon, J. H. Kim, J. Xiang, and R. Chen, "Thermal conductivity of Ge and Ge-Si core-shell nanowires in the phonon confinement regime," *Nano Lett.*, vol. 11, no. 12, pp. 5507–5513, 2011.

[159] B. Qiu, G. Chen, and Z. Tian, "Effects of Aperiodicity and Roughness on Coherent Heat Conduction in Superlattices," *Nanoscale Microscale Thermophys. Eng.*, vol. 19, no. 4, pp. 272–278, 2016.

[160] B. Decker, P. K. Schelling, and S. R. Phillpot, "Interfacial phonon scattering in semiconductor nanowires by molecular-dynamics simulation," *J. Appl. Phys.*, vol. 99, no. 12, p. 123715, 2006.

Bestpfe.com

[161] S. Plimpton, “Fast Parallel Algorithms for Short-Range Molecular Dynamics,” *Journal of Computational Physics*, vol. 117, no. 1. pp. 1–19, 1995.

[162] P. Wirnsberger, D. Frenkel, and C. Dellago, “An enhanced version of the heat exchange algorithm with excellent energy conservation properties,” *J. Chem. Phys.*, vol. 143, no. 12, p. 124104, 2015.

[163] V. Samvedi and V. Tomar, “The role of interface thermal boundary resistance in the overall thermal conductivity of Si-Ge multilayered structures.,” *Nanotechnology*, vol. 20, no. 36, p. 365701, 2009.

[164] C. Monthus and T. Garel, “Anderson localisation of phonons in dimension d=1,2,3: Finite-size properties of the inverse participation ratios of eigenstates,” *Phys. Rev. B - Condens. Matter Mater. Phys.*, vol. 81, no. 22, p. 224208, 2010.

[165] P. Chakraborty, L. Cao, and Y. Wang, “Ultralow Lattice Thermal Conductivity of the Random Multilayer Structure with Lattice Imperfections,” *Sci. Rep.*, vol. 7, no. 1, p. 8134, 2017.

[166] G. Schierning, “Silicon nanostructures for thermoelectric devices: A review of the current state of the art,” *Phys. status solidi*, vol. 211, no. 6, pp. 1235–1249, 2014.

[167] L. Thumfart, J. Carrete, B. Vermeersch, N. Ye, T. Truglas, J. Feser, H. Groiss, N. Mingo, and A. Rastelli, “Thermal transport through Ge-rich Ge/Si superlattices grown on Ge(0 0 1),” *J. Phys. D. Appl. Phys.*, vol. 51, no. 1, p. 14001, 2018.

[168] G. Gesele, J. Linsmeier, V. Drach, J. Fricke, and R. Arens-Fischer, “Temperature-dependent thermal conductivity of porous silicon,” *J. Phys. D. Appl. Phys.*, vol. 30, no. 21, pp. 2911–2916, 1997.

[169] R. J. Mehta, Y. Zhang, C. Karthik, B. Singh, R. W. Siegel, T. Borca-Tasciuc, and G. Ramanath, “A new class of doped nanobulk high-figure-of-merit thermoelectrics by scalable bottom-up assembly,” *Nat. Mater.*, vol. 11, no. 3, pp. 233–240, 2012.

[170] Y. Lee and G. S. Hwang, “Molecular dynamics investigation of the thermal conductivity of ternary silicon-germanium-tin alloys,” *J. Phys. D. Appl. Phys.*, vol. 50, no. 49, p. 494001, 2017.

[171] J. J. Pulikkotil and S. Auluck, “Band gap engineering of Si-Ge alloys for mid-temperature thermoelectric applications,” *AIP Adv.*, vol. 5, no. 3, p. 37145, 2015.

[172] M. Maldovan, “Thermal energy transport model for macro-to-nanograin polycrystalline semiconductors,” *J. Appl. Phys.*, vol. 110, no. 11, p. 114310, 2011.

[173] H. F. Zhan, Y. Y. Zhang, J. M. Bell, and Y. T. Gu, “Thermal conductivity of Si nanowires with faulted stacking layers,” *J. Phys. D. Appl. Phys.*, vol. 47, no. 1, p. 15303, 2014.

[174] H. J. Queisser, “Properties of Twin Boundaries in Silicon,” *J. Electrochem. Soc.*, vol. 110, no. 1, p. 52, 1963.

[175] L. Lu, X. Chen, X. Huang, and K. Lu, “Revealing the Maximum Strength in Nanotwinned Copper,” *Science (80-.).*, vol. 323, no. 5914, pp. 607–610, 2009.

[176] Y. Tian, B. Xu, D. Yu, Y. Ma, Y. Wang, Y. Jiang, W. Hu, C. Tang, Y. Gao, K. Luo, Z. Zhao, L. M. Wang, B. Wen, J. He, and Z. Liu, “Ultrahard nanotwinned cubic boron nitride,” *Nature*, vol. 493, no. 7432, pp. 385–388, 2013.

[177] S. Zheng, R. Zhang, R. Huang, T. Taniguchi, X. Ma, Y. Ikuhara, and I. J. Beyerlein, “Structure and energetics of nanotwins in cubic boron nitrides,” *Appl. Phys. Lett.*, vol.

BEST PFE.COM
List of research project topics and materials

109, no. 8, p. 81901, 2016.

[178] Q. Huang, D. Yu, B. Xu, W. Hu, Y. Ma, Y. Wang, Z. Zhao, B. Wen, J. He, Z. Liu, and Y. Tian, “Nanotwinned diamond with unprecedented hardness and stability,” *Nature*, vol. 510, no. 7504, pp. 250–253, 2014.

[179] A. Frachioni and B. E. White, “Simulated thermal conductivity of silicon-based random multilayer thin films,” *J. Appl. Phys.*, vol. 112, no. 1, p. 14320, 2012.

[180] Y. He, D. Donadio, and G. Galli, “Heat transport in amorphous silicon: Interplay between morphology and disorder,” *Appl. Phys. Lett.*, vol. 98, no. 14, p. 144101, 2011.

[181] L. Lindsay, D. A. Broido, and N. Mingo, “Lattice thermal conductivity of single-walled carbon nanotubes: Beyond the relaxation time approximation and phonon-phonon scattering selection rules,” *Phys. Rev. B*, vol. 80, no. 12, p. 125407, 2009.

[182] J. M. Larkin and C. Maloney, “Vibrational mode properties of disordered solids from high-performance atomistic simulations and calculations,” Carnegie Mellon University, 2013.

[183] J. M. Ziman, “Electrons and phonons: the theory of transport phenomena in solids,” *Endeavour*. 1960.